AD-A193 563 BODY AND SURFACE WAVE MODELING OF OBSERVED SEISMIC EVENTS PART 1(U) CALIFORNIA INST OF TECH PASADENA SEISMOLOGICAL LAB R W CLAYTON ET AL. 11 MAY 87 1/2

UNCLASSIFIED AFGL-TR-87-0157 F19628-85-K-0017 F/G 8/11 NL

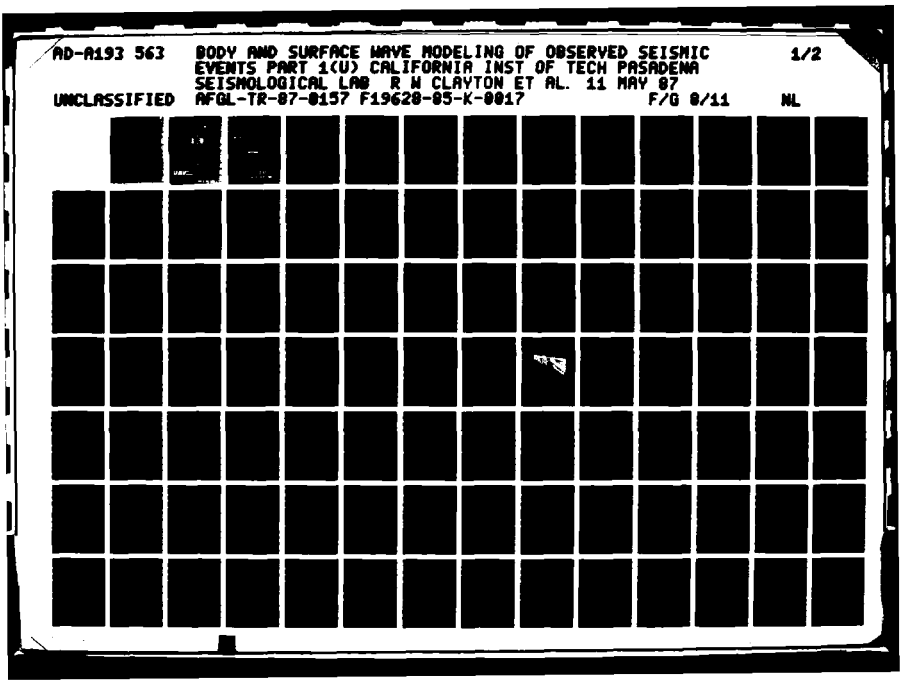

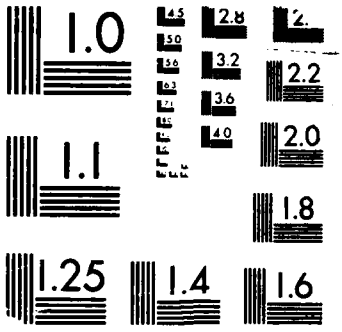

AFGL-TR-87-0157

Body and Surface Wave Modeling of Observed Seismic Events (Part I)

Robert W. Clayton
David G. Harkrider
Donald V. Helmberger

California Institute of Technology
Seismological Laboratory
Pasadena, CA 91125

11 May, 1987

Semiannual Technical Report No. 2

AIR FORCE GEOPHYSICS LABORATORY
AIR FORCE SYSTEMS COMMAND
UNITED STATES AIR FORCE
HANSCOM AIR FORCE BASE, MASSACHUSETTS 01731

"This technical report has been reviewed and is approved for publication"

JAMES F. LEWKOWICZ
Contract Manager

HENRY A. OSSING
Branch Chief

FOR THE COMMANDER

DONALD H. ECKHARDT
Division Director

This report has been reviewed by the ESD Public Affairs Office (PA) and is releasable to the National Technical Information Service (NTIS).

Qualified requestors may obtain additional copies from the Defense Technical Information Center. All others should apply to the National Technical Information Service.

If your address has changed, or if you wish to be removed from the mailing list, or if the addressee is no longer employed by your organization, please notify AFGL/DAA, Hanscom AFB, MA 01731. This will assist us in maintaining a current mailing list.

Do not return copies of this report unless contractual obligations or notices on a specific document require that it be returned.

REPORT DOCUMENTATION PAGE

1a. REPORT SECURITY CLASSIFICATION: UNCLASSIFIED	1b. RESTRICTIVE MARKINGS
2a. SECURITY CLASSIFICATION AUTHORITY	3. DISTRIBUTION/AVAILABILITY OF REPORT: Approved for public release; distribution unlimited.
2b. DECLASSIFICATION/DOWNGRADING SCHEDULE	
4. PERFORMING ORGANIZATION REPORT NUMBER(S)	5. MONITORING ORGANIZATION REPORT NUMBER(S): AFGL-TR-87-0157
6a. NAME OF PERFORMING ORGANIZATION: California Institute of Tech. Seismological Laboratory; 6b. OFFICE SYMBOL (If applicable)	7a. NAME OF MONITORING ORGANIZATION: Air Force Geophysical Laboratory
6c. ADDRESS (City, State and ZIP Code): Pasadena, California 91125	7b. ADDRESS (City, State and ZIP Code): Hanscom Air Force Base, Massachusetts 01731
8a. NAME OF FUNDING/SPONSORING ORGANIZATION: Advanced Research Projects Agency (DOD); 8b. OFFICE SYMBOL (If applicable)	9. PROCUREMENT INSTRUMENT IDENTIFICATION NUMBER: F19628-85-K-0017
8c. ADDRESS (City, State and ZIP Code): 1400 Wilson Boulevard, Arlington, Virginia 22209	10. SOURCE OF FUNDING NOS.

PROGRAM ELEMENT NO.	PROJECT NO.	TASK NO.	WORK UNIT NO.
61102F	5A10	DA	AA

11. TITLE (Include Security Classification): Body and Surface Wave Modeling of Observed Seismic Events (PART 1)

12. PERSONAL AUTHOR(S): Robert W. Clayton, David G. Harkrider and Donald V. Helmberger

13a. TYPE OF REPORT	13b. TIME COVERED	14. DATE OF REPORT (Yr., Mo., Day)	15. PAGE COUNT
Semi-annual Technical No. 2	FROM 7/14/85 TO 1/13/86	May 11, 1987	162

16. SUPPLEMENTARY NOTATION

17. COSATI CODES		
FIELD	GROUP	SUB. GR.

18. SUBJECT TERMS (Continue on reverse if necessary and identify by block number): Strong motion; 2-D modeling of sedimentary basins; 1971 San Fernando earthquake; Lg wave propagation; coupling; finite-element - propagator matrix codes

19. ABSTRACT (Continue on reverse if necessary and identify by block number)

The research performed under the contract, during the period 14 July 1985 through 13 January 1986, can be divided into two main topics; the effects of lateral structure, in particular, complicated sedimentary basins on the propagation and amplication of seismic strong motion, and the effects of ocean continent transition zones on L_g waves.

In section II, 2-D finite diffference techniques are used to model the seismic strong motions observed for the 1971 San Fernando earthquake. The finite difference seismograms show strong effects due to lateral variation in sediment thickness in the San Fernando valley and the Los Angeles basin. Using basin structure derived mostly from well

20. DISTRIBUTION/AVAILABILITY OF ABSTRACT	21. ABSTRACT SECURITY CLASSIFICATION
UNCLASSIFIED/UNLIMITED ☐ SAME AS RPT. ☐ DTIC USERS ☐	UNCLASSIFIED

22a. NAME OF RESPONSIBLE INDIVIDUAL	22b. TELEPHONE NUMBER (Include Area Code)	22c. OFFICE SYMBOL
James Lewkowicz	(617)377-3028	AFGL/LWH

logs and teleseismically determined source parameters, two dimensional SH and P-SV finite difference calculations reproduce the amplitude and duration of the strong motion velocities recorded across the Los Angeles and San Fernando basins for the period range 2 to 10 seconds. The edges of basins nearest the seismic source show ground motion amplification up to a factor of three over the case without the basin, and tend to convert direct shear waves into Love and Rayleigh waves that travel within the basin.

In section III, the methods for Representation Theorem (RT) coupling of finite element (FE) or finite difference calculations and propagator matrix method calculations to produce a hybrid method for propagation of SH mode sum seismograms across paths that contain regions of non plane-layered structure are explained and developed. The coupling methods explained in detail use a 2-D Cartesian FE formulation. Extensive tests illustrating the validity and accuracy of the implementation of these coupling methods are discussed. These hybrid techniques are developed to study the propagation of surface waves across regional transition zones or other heterogeneities that exist in part of a longer, mostly plane-layered, path. The effects of a thinning or thickening of the crustal layer on the propagation of L_g mode sum seismograms will be examined in later reports.

SEMI-ANNUAL TECHNICAL REPORT
14 July 1985 - 13 January 1986

ARPA Order No.:	5299
Name of Contractor:	California Institute of Technology
Effective Date of Contract:	14 January 1985
Contract Expiration Date:	13 January 1987
Contract Number:	F19628-85-K-0017
Principal Investigators:	Robert W. Clayton (818) 356-6909
	David G Harkrider (818) 356-6910
	Donald V. Helmberger (818) 356-6998
Program Manager:	James F. Lewkowicz (617) 861-3028
Short Title of Work:	Body and Surface Wave Modeling of Observed Seismic Events

Sponsored by
Defense Advanced Research Projects Agency (DOD)
Defense Sciences Office, Geophysical Sciences Division
DARPA/DSO Physical Characterization of Seismic Sources
ARPA Order No. 5299.
Issued by the Air Force Geophysics Laboratory under
Contract# F19628-85-K-0017

Seismological Laboratory
Division of Geological and Planetary Sciences
California Institute of Technology
Pasadena, California 91125

TABLE OF CONTENTS

I. Summary

The research performed under the contract, during the period 14 July 1985 through 13 January 1986, can be divided into two main topics; the effects of lateral structure, in particular, complicated sedimentary basins on the propagation and amplication of seismic strong motion; and the effects of ocean continent transition zones on L_g waves.

In section II, 2-D finite diffference techniques are used to model the seismic strong motions observed for the 1971 San Fernando earthquake. The finite difference seismograms show strong effects due to lateral variation in sediment thickness in the San Fernando valley and the Los Angeles basin. Using basin structure derived mostly from well logs and teleseismically determined source parameters, two dimensional SH and P-SV finite difference calculations reproduce the amplitude and duration of the strong motion velocities recorded across the Los Angeles and San Fernando basins for the period range 2 to 10 seconds. The edges of basins nearest the seismic source show ground motion amplification up to a factor of three over the case without the basin, and tend to convert direct shear waves into Love and Rayleigh waves that travel within the basin.

In section III, the methods for Representation Theorem (RT) coupling of finite element (FE) or finite difference calculations and propagator matrix method calculations to produce a hybrid method for propagation of SH mode sum seismograms across paths that contain regions of non plane-layered structure are explained and developed. The coupling methods explained in detail use a 2-D Cartesian FE formulation. Extensive tests illustrating the validity and accuracy of the implementation of these coupling methods are discussed. These hybrid techniques are developed to study the propagation of surface waves across regional transition zones or other heterogeneities that exist in part of a longer, mostly plane-layered, path. The effects of a thinning or thickening of the crustal layer on the propagation of L_g mode sum seismograms will be examined in later reports.

Elastic Finite-Difference Modeling of the 1971 San Fernando, Ca. Earthquake

John E. Vidale

Donald V. Helmberger

March 17, 1987

ABSTRACT

Finite-difference seismograms calculated for the 1971 San Fernando earthquake show strong effects due to lateral variation in sediment thickness in the San Fernando valley and the Los Angeles basin. Using basin structure derived mostly from well logs and teleseismically-determined source parameters, two-dimensional SH and P-SV finite difference calculations reproduce the amplitude and duration of the strong motion velocities recorded across the Los Angeles and San Fernando basins for the period range 2 to 10 seconds. The edges of basins nearest the seismic source show ground motion amplification up to a factor of three over the case without the basin, and tend to convert direct shear waves into Love and Rayleigh waves that travel within the basins.

INTRODUCTION

The San Fernando earthquake of February 9, 1971 produced one of the most complete sets of strong-ground records from a large thrust earthquake to date, and consequently has generated a large body of seismological literature. Hanks (1975) notes that seismic moment, source dimension, radiation pattern, rupture propagation, the development and dispersion of local surface waves, and azimuthal variations in the gross geological structure all appear to have first-order significance in fashioning the amplitude and frequency content of the strong-motion waveforms. Heaton (1982), among others, has modeled some of these features, but adds that many features of the observed motions remain unexplained, and considerable uncertainty still exists regarding the faulting history of the San Fernando earthquake.

One drawback of existing studies is the inability to properly simulate the propagational effects associated with the complicated sedimentary basins in and around Los Angeles. Finite element schemes have been used to explain some of the effect of basins on surface waves body waves, and the static deformation (Drake and Mal, 1972, McCowan et al., 1977). However, these efforts did not address the demanding task of modeling seismic profiles along paths crossing the various basin and ridge structures, as discussed qualitatively by Liu and Heaton (1984). The modeling of one such three-component profile is the subject of this study.

STRONG MOTION RECORDS

The filled triangles in Figure 1 locate three component accelerometers that recorded the strong motions of the San Fernando earthquake along a north-south profile. Figure 2 shows the vertical, radial, and transverse velocities recorded at these stations. The accelerations were integrated to velocities by EERL (1974).

We model velocities two reasons; first, it is currently economical to model only greater than 1 sec period seismic energy to ranges of 50-60 km with our finite-difference scheme, and velocity but not acceleration records have these periods, and second, we have less confidence in our knowledge of the geologic structures with wavelengths shorter than a few kilometers, which primarily influence shorter-period seismic waves. These records comprise profile I in Liu and Heaton (1984). The absolute timing of these records is not known so they are lined up relative to an early, high-frequency arrival on the vertical component that is probably a direct compressional wave.

Before discussing these motions in detail, it is useful to review the geological structure along this profile. A schematic cross-section is given on the bottom of Figure 1. Figure 3 shows the geologic layering in this cross-section in more detail, with an inferred shear wave velocity structure below. The stratigraphy is taken from Duke et al. (1971), who reviewed the well logs and the geological cross-sections in the literature for this area. Many well logs have been recorded around the Los Angeles basins because of oil exploration and these logs yield estimates of density and velocity. Duke et al. (1971) also conducted numerous small-scale refraction surveys to find the near-surface compressional-wave velocity profile. With knowledge of the composition of the rocks at depth, the shear-wave velocity can also be reliably estimated. Near surface values of the attenuation operator Q have also been provided by a variety of schemes. Duke et al. (1971) reports the details of this cross-section at great length.

Although the structure within the San Fernando and Los Angeles basins along this profile can be reliably estimated from the above study, the structure below the basins is less well-known since, unfortunately, the well logs stop as soon as they encounter the basement rock. Below the basins, we use the structure given in Kanamori and Hadley (1975) for compressional waves, and assume

that V_p / V_s is $\sqrt{2}$ Table 1 gives the compressional wave velocity and density associated with each shear wave velocity shown in Figure 3.

The motions shown in Figure 2 correspond with the geologic setting in which they were recorded. Within the San Fernando basin, a train of surface waves develops with an apparent velocity of 1 km/sec. The wavetrain lengthens as it propagates across the basin. On the Santa Monica mountains, the surface waves disappear and the amplitude falls by a factor of two. In the Los Angeles basin, the surface wave is again present with a slow apparent velocity, and the amplitudes increase by roughly a factor of two relative to the ridge. Near the ocean, in the Palos Verdes hills, the surface wave is still present, but the amplitude has dropped more rapidly than geometric spreading would predict. Geometric spreading would be $1/\sqrt{r}$ for surface waves and $1/r$ for body waves in a wholespace. Spreading for a layered halfspace can fall off by higher powers of r for body waves, but the data suggest surface waves are present and show a decrease by a factor of 3 from H118 and S267 to N191, where the range increases from 50 to 70 km, which would require a large exponent on r. It is these patterns, some of which are discussed by Liu and Heaton (1984), that we will attempt to understand by forward modeling through the FD technique with laterally varying structures.

Before forward modeling with a technique that assumes two-dimensional symmetry, we will verify that the seismic energy in the records is not significantly laterally reflected. Vidale (1986) uses complex polarization analysis that is an extension of the method of Montalbetti and Kanasewich (1970) to examine the three-component records for this profile of records from the San Fernando earthquake. Because the method works in the complex domain, elliptically as well as linearly polarized data may be interpreted. This analysis finds the direction of propagation for the Love and Rayleigh waves. The direction may be obtained

because the Love wave is linearly polarized transverse to the direction of propagation, and the Rayleigh wave is elliptically polarized in the plane that contains the vertical and the propagation directions.

The analysis in Vidale (1986) shows that the energy in this particular profile is traveling within 15° of radially outward from the source. This suggests that despite the three-dimensional nature of the basins, the geometry may be approximated by a two-dimensional model with useful results. We should note, however, that although the energy in this profile travels radially out from the source to the receiver, amplitude attenuation due to geometrical spreading depends on the curvature of the wavefront, so the amplitude may vary somewhat due to three-dimensional effects even if the energy path is not laterally deflected.

To match the frequency limitations of the FD algorithm, we low-pass filter the data. The FD method can only propagate energy with six or more grid points per wavelength, so to properly treat high frequencies, more grid points and therefore more calculation is required. Figure 2b shows the filtered vertical, radial, and transverse velocities that will be addressed in this modeling study.

REVIEW OF SOURCE PARAMETERS

The San Fernando earthquake has also been the subject of studies that concentrated on other data sets, namely the teleseismic body waves, the long-period surface waves, the location of preshocks and aftershocks, and the static displacements. These studies will help us estimate the source parameters. First, we will briefly review these studies to help clarify some of the uncertainties.

The seismicity studies (Allen et al., 1973, Whitcomb et al., 1973) reveal a relatively diffuse zone of aftershocks with a combination of thrust and left-lateral strike-slip mechanisms. By locating the mainshock relative to well-located aftershocks recorded on a temporarily deployed array, Whitcomb et al. (1973) place

the hypocenter at a depth of 8 km at 34° 24.7′ N and 118° 24.0′ W, with the mechanism listed in Table 2. The errors in hypocentral depth are conservatively estimated at ± 8 km vertically and ± 4 km horizontally. The aftershocks suggest that the plane of faulting dipped 35° to the north down to 8 km depth, below which the fault plane dipped 50°. The mechanism derived from first motions by Whitcomb et al. (1973), listed in Table 2, is similar to the teleseismic results.

Examination of the static displacements due to the earthquake (Alewine, 1974) reveals distributed slip from near the surface to a depth of about 14 km along the north dipping fault plane. The portion of the fault from the surface down to 5 km depth underwent about 5 m of slip, and the segment from 10 to 14 km depth shows 2-5 m slip, and there may be an area of less slip from 5 to 10 km depth. The greater the depth, however, the worse the resolution of static analysis. The static moment is estimated to be between 1.0 and 2.2 X 10^{26} dyne-cm.

The 16-60 sec fundamental Rayleigh waves generated by the San Fernando earthquake are analyzed by Alewine (1974), and given the strike and dip suggested by Whitcomb et al. (1973), the moment is found to be 1.7 X 10^{26} dyne-cm. Half the moment release is found to be at depths of about 3-8 km and the other half of the moment release is below about 10 km.

The teleseismic body wave studies (Langston, 1978, and Heaton, 1982) use records from long-period WWSSN stations to find the mechanism and 5-30 second period faulting history in time and space.

Both Langston (1978) and Heaton (1982) find a double source. In the various models, there is a source at 10-15 km depth with a moment of 0.5 X 10^{26} dyne-cm and there is a shallower source with a shallower dip angle that also has a moment of 0.5 X 10^{26}. The two sources are found to have a slightly different

strikes and the shallower source dips less, as shown in Table 2. When Heaton (1982) attempts to model the near-in records and static data as well as the teleseismic data, his estimate of the total moment rises to 1.7 X 10^{26} dyne-cm. Figure 4 summarizes the results from the teleseismic modeling of Langston (1978) and Heaton (1982).

The short-period WWSSN records are also examined in the search for higher frequency (0.5-3.0 second period) details of the faulting history (Hanks, 1975, and Langston, 1978). The work of both Langston (1978) and Hanks (1975) suggest that the first pulse of short-period energy originated about 12 km below the surface. If the pulse of energy came from the hypocenter, which was on the fault plane as defined by the aftershocks, the location from Whitcomb et al. (1973) would have to be in error by 4 km vertically and 4 km horizontally. Some of the short-period WWSSN records, however, indicate a small precursor about 2 seconds before the initial large pulse, so perhaps the hypocenter and the location of the short-period energy release are not coincident.

In this study, we find that a point source at 10 km depth with the mechanism of Heaton's deep source (which is nearly identical to Langston's deep source) can explain most of the data. The sensitivity of our modeling to changes in source depth and mechanism are discussed below.

NUMERICAL MODELS OF THE STRONG MOTIONS

Our methods are described in the article in this issue by Helmberger and Vidale (1987). More details of these two-dimensional finite-difference (FD) SH and P-SV algorithms that are used to calculate the Green's functions are described in Vidale et al. (1985), Vidale and Helmberger (1987), Clayton and Vidale (1987), and Vidale and Clayton (1986). The finite-difference method is of fourth-order accuracy as defined by Alford et al. (1974). The seismic energy from

the source is introduced into the grid by the method of Alterman and Karal (1968). This method, as we use it, requires the source to be placed in a region of the grid of constant density and velocities.

Expressions describing line-source excitation functions used in the line-to-point-source mapping may be found in Helmberger and Vidale (1987). The exact dislocation solution is expressed in an asymptotic series in which the displacement decouples into the SH and P-SV systems where the vertical and azimuthal radiation patterns separate explicitly. Therefore we can make separate FD calculations to model the SH and P-SV radiation. The expressions containing the vertical radiation patterns are loaded into the grid source box. The azimuthal radiation patterns are factored in later according to the fault orientation. This FD procedure does not handle the near-field terms properly at small horizontal distances, but numerical checks indicate accurate results beyond about 10 km for a source at a depth of 10 km.

The Green's functions for the transverse component of velocity for the four source locations shown in Figure 3 are displayed in Figures 5 and 6 where $j=4$ corresponds to the strike-slip and $j=5$ to the dip-slip components. The Green's functions correspond to the $\tilde{V}_j$ in Equations 1 and 14 of Vidale et al. (1985), and are equivalent to Equation 24 in Helmberger and Vidale (1987, this issue) for the case where the source is impulsive and only one of A_4 and A_5 is nonzero. A Q of 25 is included in the calculation.

The ranges indicated on the left are appropriate for the deepest source. For shallower sources, we chose to leave the receivers at the same point in the structure with the same range, rather than shift them by the difference in hypocentral position, so the ranges are approximate for the shallower sources. Note that the shallower sources are located further to the south. The change in polarity for the first station for the source S indicates that the source is just to the south of the

first receiver. However, we are only interested in the records written at the larger distances where the near-field terms can be neglected. A seismic attenuation Q of 25 is assumed; this value falls within the wide range of Q's reported by Duke et al. (1971).

Incorporation of spatially varying attenuation into finite-difference calculations is possible with Pade approximants (Day and Minster, 1984, Witte and Richards, 1986) but requires much computation. We use a simpler scheme in this paper to include the effect of a constant Q. Our scheme is derived from one that has been used in generalized ray calculations for some years (Carpenter, 1967). The quantity $t^* = \int 1/vQ \; ds$ or $t^* = \int 1/Q \; dt$ may be computed for a given ray, and a convolutional attenuation operator can be computed for any t^* (see Futterman, 1962, for example). If Q is constant, $t^* = t/Q$, thus t^* is only a function of time. In the computation of teleseismic arrivals, t^* remains approximately constant during the time window in which a P-wave or even several branches of a P-wave triplication arrive.

The profile in this paper is more complicated, however, in that the time window is not short compared to the travel time from the source. Since Q is included with a convolution-like operator, however, we need not use the same operator for each point in time. Q is then incorporated by convolving at each point in time of the seismograms the Futterman Q operator for a $t^* = t/Q$. Of course, the convolution-like operation may not be done in the frequency domain since every time point requires a different Q operator. In practice, we only calculate a new Q operator for each 50 time points since the Q operator changes gradually with time, and computing an operator requires an FFT.

A moment of 10^{26} dyne-cm is used for the 10 km source depth. To compare amplitudes between different depths, we hold AD_o rather than the moment μAD_o constant to avoid the strong tendency to generate larger seismic motions

in softer material.

The Love waves dominate the motions for the dip-slip case at all depths whereas the direct S arrivals are more noticeable in the strike-slip case, especially at the greater depths. These features may be understood in terms of vertical radiation patterns. The strike-slip source radiates most of the energy horizontally, which appears as direct body waves, while the dip-slip pattern tends to radiate energy vertically, where it can be trapped to form surface waves.

The strike-slip Green's function is the most important for the transverse component of motion for the San Fernando earthquake, despite the fact that the mechanism is dominantly thrust. This is because a 45° dip-slip event produces the same radiation pattern of SH energy as a strike-slip event, but rotated 45° in strike. The A_4 coefficient (strike-slip case) is about 10 times larger than the A_5 coefficient (dip-slip case) in both Langston's (1978) and Heaton's (1982) solution for the deep source. Heaton's shallow source is also dominated by the strike-slip solution but Langston's shallow source is about one-third composed of the dip-slip solution. For these reasons, we have conducted most of our sensitivity studies with the strike-slip case. Synthetic transverse ground motions can be generated from the Green's functions shown in Figures 5 and 6 by performing the operations indicated in equation 1 of Vidale et al. (1985). Transverse velocity records convolved with the 3 second time function shown in Figure 8c are shown in Figure 7b. Seismograms for a flat-layered approximation to the deep basin structure are included in Figure 7a for comparison.

These synthetic seismograms for a flat structure are sensitive to the source depth in both amplitude and waveform. The shallowest source excites large, slow Love waves, and would make even larger, higher-frequency waves were it not for the strong damping due to the Q of 25. Even considering the inefficiency of the mechanism of the shallow source in exciting radiation along this profile, 0.1 X

10^{26} dyne-cm of moment in the shallow source would suffice to generate waves as large as those observed.

The shallow source creates such large waves for two reasons. First, the softer material near the surface allows larger velocities to develop for a given moment than the stiffer material at greater depth. Second, the shallower source is closer to the edge of the slow San Fernando basin than the deeper sources, and it can trap a larger portion of its energy as surface waves. The direct body-wave has a negligible amplitude compared to the surface wave for all but the two closest stations. Source I generates smaller seismic waves, and excites surface waves with a range of velocities. The direct arrival is distinct for all ranges, and source D produces predominantly a direct diving wave. Surface waves do not contribute much energy to the records for the intermediate and deep sources. It is clear that for this flat-layered geometry, the shallow source generates much more surface motion per unit moment than the intermediate and deep sources.

The moments of 1-2 X 10^{26} dyne-cm found by the studies in Table 2, placed at the intermediate or deep depth are consistant with the peak velocities observed. The synthetic waveform fit with the data, however, is improved considerably by the empirical source time function described below.

The waveforms from the more realistic structure, Figure 7b, are more complicated than in the flat-layered case. Sources at all depths can excite noticeable surface waves in both basins. This result arises because direct energy incident on the edges of the basin can be trapped by the basins much more efficiently than the direct waves can tunnel into the flat layers (Vidale et al., 1985, for example). The source S still excites larger motions on the surface, again largely because a source in the slower medium generates larger amplitude waves, and also because the shallow source is closer to the basin edge, allowing a larger percentage of its energy to be trapped. A source at location B produces seismograms very similar

to those of a source at location D, except for a smaller amplitude, which is due to the faster velocity at the deeper depth.

The surface waves that are traveling within the San Fernando basin can, to some extent, tunnel across the Santa Monica mountains to enter the Los Angeles basin. Significant energy also must be reradiated as body wave energy when the surface waves reach the far side of the basins since the surface waves do not either continue into the next basin or reflect back from the edge. Little energy reverses direction and travels back to the north in the basins. The peak amplitudes of the velocity traces are greater for the realistic structure than for the flat-layered structure in the San Fernando basin, but the reverse is true in the Santa Monica mountains. In the Los Angeles basin, the peak amplitudes are less than in the flat-layered case because the receivers are in the shadow of the mountains, for the case of sources S and I. The source D, however, excites the Los Angeles basin with a direct S wave, which is more efficiently converted to surface waves in the realistic than the flat-layered geometry.

Note that the seismograms for the source D in Figure 6 show many of the characteristics of the data displayed in Figure 2, that is, reduced amplitude with simple direct pulses at the Santa Monica mountains and significant surface wave arrivals in each basin. Source I, at 6 km depth, matches the data nearly as well, but has too much energy in surface waves compared to direct waves. For the rest of the paper we will consider only a point dislocation source at 10 km depth. Most probably, the source was actually finite, but most of the effect of source finiteness may be included in the source time function for the purpose of understanding the motions in the basins. What we do not include seems less significant than the effect of the structure, which is the focus of this paper. This conclusion is justified by noting that a point source with an empirical source time function, an independent velocity structure, and a teleseismically determined

mechanism explains most of the velocity records observed in the basin. This approach introduces a slight contradiction; we put both pulses at 10 km depth with the same mechanism, while Langston (1978) and Heaton (1982) separate the two pulses and give them distinct mechanisms. Either the separation and differing mechanisms are less than were estimated or our simpler approach produces a similar result, for in the end we can match the data within the limitations of our knowledge of the structure and our 2-D approach.

The FD seismograms in Figure 7b suggest that the body wave appears at the ridge with a time function very similar to the source time function. The waveform of the transverse component at the ridge station D068 is shown in velocity and displacement in Figure 8. The displacement trace shows two strong pulses of energy. Heaton's (1982) source model predicts a strong second arrival with a 4 second time delay, while Langston (1978) finds a value of 4.9 seconds. Both models appear to fit the observations at the ridge quite well. The relative amplitude ratio of the two pulses appear to favor the Langston source model, which is given in Table 2.

One possible strategy at this point would be to add the secondary source and make adjustments in the source time description. Another approach that might be called an "empirical source model" is to assume that the displacement record D068 is a good source description in this particular direction and use it to predict the other seismograms. This empirical approach is adopted and the FD seismograms with the empirical source model are presented in Figure 9. The moment, which is difficult to control because the long-period information is absent from the data, is set so that the amplitude of the observed transverse record at station D068 matches the synthetic at that range. When a cluster of stations are at nearly the same range, only one representative trace is plotted.

In Figure 9, the agreement between the data and the FD seismograms is excellent at all but the closest range, C041 at Pacoima dam, where the near-field assumptions break down and finiteness and directivity may become important. The frequency content of the records in the San Fernando valley is higher in the data than in the synthetics, which is probably due to inaccuracies in the velocity profile which produce too low a resonant frequency in the FD modeling.

The P-SV motions can be simulated by constructing Green's functions as for the SH case except that two rather than three fundamental fault orientations are required. These responses for the assumed two-dimensional structure and 10 km deep source are given in Figure 10. As discussed earlier, the vertical radiation patterns strongly influence the relative body-wave to surface-wave ratios. The A_1, A_2, and A_3 factors are all significant for the deep source mechanism. The A_3 or 45^o dip-slip component dominates, as might be expected for a mostly thrust event, because A_3 is slightly larger than A_1 and A_2 and the amplitudes of the Green's functions for A_3 are larger than those of A_1 and A_2.

The FD seismograms are compared with the data for the vertical and radial components in Figures 11 and 12. Again, when a cluster of stations are at nearly the same range, only one representative trace is plotted. The amplitude of the synthetic seismograms is determined from the SH scaling described above. The match in timing is somewhat arbitrary since there is no absolute timing for the data.

The match in amplitude between the P-SV synthetic velocities and the data is good. In addition, the duration of shaking in the San Fernando basin and the waveforms at the start of the record in the Los Angeles basin are also well-modeled using the empirical time function. As in the SH case, the Santa Monica mountains produce a strong decrease in the amplitude of the velocity traces, and both basins apparently convert the direct waves into surface waves, Rayleigh

waves in this case, at the edge nearest the source.

Two troublesome problems appear in the forward modeling of the San Fernando records. First, the small amount of shallow moment release allowed by our model is in conflict with observations of 1 meter of thrust motion measured at the surface by Alewine (1974), as well as the suggestions of Heaton (1982), Langston (1978) and Alewine (1974) of significant shallow moment release. In our model, sources at between 6 and 14 km depths excite basins in a similar way, so it is only in the top 5 km that we would exclude significant moment release. The half-space model of Heaton (1982) and the layered model of Langston (1978) overestimate the velocity near the surface, so a smaller moment would serve to excite the same energy in the seismic waves given the correct lower velocities. Also, it is possible that the energy radiated from the shallow portion of the fault is absorbed by some mechanism such as decoupling of the two sides of the fault plane or very low Q in the region, but these explanations are not compelling. The main point of this paper is that the relative amplitudes and duration of shaking across basins can be explained with FD modeling, and the details of faulting in our model are secondary. To the extent that shallow sources tend to excite larger motions in the San Fernando basin relative to those in the Los Angeles basin than were observed, this study suggests less moment release shallower than about 6 km depth than the studies of Heaton (1982) and Langston (1978).

The second problem may be seen in Figures 11 and 12, where the Rayleigh wave created in the San Fernando basin tunnels across the Santa Monica mountains and has a much larger amplitude in the Los Angeles basin than is seen in the data. We have tried rather extreme structures such as more separation between the basins and different kinds of edges on the basins, but the Rayleigh waves simply are better at tunneling across the mountains than the Love waves,

and it is difficult to match the data. Three-dimensional effects may be responsible for this problem. Since this profile skirts the west edge of the Los Angeles basin, the Rayleigh waves jumping the mountains will be refracted into the slower material in the center of the basin and the amplitude of these Rayleigh waves at stations H118 and S267 may be small.

An alternative explanation may be that the velocity model for the San Fernando basin has too thick a column of slow sediments. In the data, it appears that the surface waves are shorter period in the San Fernando basin than the Los Angeles basin. In the model, the same 3-5 second period surface waves are excited in both the San Fernando and Los Angeles basins, suggesting that the San Fernando basin model is inaccurate in that it should have a thinner layer of slow sediments than the Los Angeles basin. If the two basins had distinctly different resonant periods, the surface waves from the San Fernando basin would not excite the Los Angeles basin as much.

The peak amplitude comparison between the data and the FD synthetics is summarized in Figure 13. The match is very good. We did not deviate from the velocity model derived from Duke et al. (1971) to keep this as much of a forward-modeling exercise as possible. We feel as a forward-modeling exercise, this simulation has been successful.

For insight into the creation and destruction of the surface waves at the edges of the basins, the envelope of the transverse velocity records is shown in Figure 14. For this plot, 250 rather than eight receivers are used. In this figure, a sketch of the basins and mountains is included at the bottom for location. We use the same source location and empirical time function as we did for the previous synthetics seismograms. The first arrival in the seismograms displayed in Figures 9 and 14 is the direct SH wave. The direct wave advances slightly at the Santa Monica mountains because of the faster material at the surface. In both

the San Fernando basin and the Los Angeles basin, the direct SH wave incident upon the edge of the basin nearest the epicenter produces a surface wave train (Love waves) that crosses the basin then converts back to body waves.

Some energy from the Love wave in the San Fernando basin converts to a body wave with a rapid apparent velocity across the Santa Monica mountains, then partially converts back to a surface wave in the Los Angeles basin. This arrival may be thought of as surface wave energy that has tunneled across the mountains. The surface wave generated by the direct SH pulse, however, is stronger than the tunneling surface wave for this source location and mechanism.

CONCLUSIONS

The strong motions recorded within the San Fernando and Los Angeles basins during the San Fernando earthquake of 1971 can be largely understood by forward modeling with teleseismically determined source parameters through known structure with only two dimensional variations in velocity and density. This modeling will accept less moment release shallower than 5 km depth than has been suggested in some previous studies, but this inconsistancy might be reconciled if the fully three dimensional structure appropriate for closed basins is used in the FD calculation. The dramatic differences between using the laterally varying structure of Duke et al. (1971) and a flat-layered structure render it impossible to fit this data from the San Fernando earthquake with a flat-layered model.

The geometry of the basin structure is important in determining the attenuation of peak velocity along a profile, as has been previously suggested by theoretical studies (Boore, 1970, Lysmer and Drake, 1972, Bard and Gariel, 1986). The mountains shadow the basins behind them against shallow surface waves, but the edges of the basin nearest the earthquake tends to convert body waves

again to shallow surface waves. The source depth of the earthquake is less important than for the flat-layered case in determining the duration of shaking and attenuation of peak amplitude with distance. Basins with sharp edges tend to generate some back-scattered surface waves; basins with gradual edges have negligible back-scattered energy.

It is encouraging that the 2-10 second period seismic waves observed in the San Fernando and Los Angeles basins can be largely explained by known structure. We feel that this line of deterministic modeling can help us understand and reduce the uncertainties in amplitude attenuation with distance of strong motions.

ACKNOWLEDGEMENTS

This work has been supported by the U.S.G.S., No. 14-08-0001-21912, by the Air Force Geophysics Laboratory, No. F19628-83-K-0010, and by the Defense Advanced Research Project Agency, No. F19628-85-K-0017. J.E.V. was supported by an NSF fellowship. Robert W. Clayton and Art Frankel aided in the development of the finite difference program. The authors appreciate the care taken by an anonymous reviewer, Heidi Beth Houston, and David Boore to make the manuscript lucid. California Institute of Technology contribution number 4360.

REFERENCES

Alewine, R.W., III (1974). Application of linear inversion theory toward the estimation of seismic source parameters, *Ph.D. Thesis*, California Institute of Technology, Pasadena, California, 303 pp.

Alford, R.M., K.R. Kelley and D.M. Boore (1974). Accuracy of finite-difference modeling of the acoustic wave equation, *Geophysics* 39, 834-842.

Allen, C.R., T.C. Hanks, and J.H. Whitcomb (1973). San Fernando earthquake: Seismological studies and their implications, in *San Fernando, California, Earthquake of February 9, 1971, Volume I, Geological and Geophysical studies*, U.S. Government Printing Office, Washington, D.C..

Alterman, Z. and F.C. Karal (1968). Propagations of elastic waves in layered media by finite-difference methods, *Bull. Seism. Soc. Am.*, 58, 367-398.

Bard, P. and J. Gariel (1986). The seismic response of two-dimensional sedimentary deposits with large vertical velocity gradients, *Bull. Seis. Soc. Am.*, 76, 343-366.

Boore, D.M. (1970). Love waves in a non-uniform waveguide: finite difference

calculation, *J. Geophys. Res.*, 75, 1512-1527.

Carpenter, E.W. (1967). Teleseismic signals calculated for underground, underwater, and atmospheric explosions, *Geophys.*, 32, 17-32.

Clayton, R.W., and J.E. Vidale (1987). Finite-difference wave simulation, manuscript in preparation.

Day, S.M., and J.B. Minster (1984). Numerical simulation of attenuated wavefields using a Pade approximant method, *Geophys. J. R. astr. Soc.*, 78, 105-118.

Drake, L.A., and A.K. Mal (1972). Love and Rayleigh waves in the San Fernando Valley, *Bull. Seism. Soc. Am.*, 62, 1673-1690.

Duke, C.M., J.A. Johnson, Y. Kharraz, K.W. Campbell, and N.A. Malpiede (1971). *Subsurface site conditions and geology in the San Fernando earthquake area*, UCLA-ENG-7206, School of Engineering, UCLA.

EERL, Caltech (1974). Strong Motion Earthquake Accelerograms, vol. II, Report from Earthquake Engineering Research Laboratory, California Institute of Technology, Pasadena, California.

Futterman, W.I. (1962). Dispersive body waves, *J. Geophys. Res.*, 67, 5279-5291.

Hanks, T.C. (1975). Strong ground motion of the San Fernando, California, Earthquake: ground displacements, *Bull. Seism. Soc. Am.*, 65, 193-225.

Heaton, T.H. (1982). The 1971 San Fernando earthquake: a double event? *Bull. Seism. Soc. Am.*, 72, 2037-2062.

Helmberger, D.H. and J.E. Vidale (1987). Modeling strong motions produced by earthquakes with 2-D numerical codes, *Bull. Seism. Soc. Am.*, (this issue).

Kanamori, H., and D. Hadley (1975). Crustal structure and temporal velocity change in southern California, *Pageoph.*, 113, 257-280.

Langston, C.A. (1978). The February 9, 1971 San Fernando earthquake: a study of source finiteness in teleseismic body waves, *Bull. Seism. Soc. Am.*, 68, 1-29.

Liu, H.L., and T.H. Heaton (1984). Array analysis of the ground velocities and accelerations from the 1971 San Fernando California earthquake, *Bull. Seism. Soc. Am.*, 74, 1951-1968.

Lysmer, J. and L.A. Drake (1972). A finite element method for seismology (in volume 11 of *Methods of Computational Physics*, Bruce Bolt, ed., entitled *Seismology: surface waves and earth oscillations*)

McCowan, D.W., P. Glover, S.S. Alexander (1977). A static and dynamic finite element analysis of the 1971 San Fernando, California, earthquake, *Geophys. J. R. astr. Soc.*, 48, 163-185.

Montalbetti, J.F., and E.R. Kanasewich (1970). Enhancement of teleseismic body phases with a polarization filter, *Geophys. J. R. astr. Soc.*, 21, 119-129.

Vidale, J.E. (1986). Complex polarization analysis of particle motion, *Bull. Seis. Soc. Am.*, in press.

Vidale, J.E., and D.H. Helmberger (1987). Path effects in strong motion seismology, (in 1987 volume of *Methods of Computational Physics*, Bruce Bolt, ed., entitled *Seismic strong motion synthetics*)

Vidale, J.E., D.H. Helmberger, and R.W. Clayton (1985). Finite-difference seismograms for SH waves, *Bull. Seism. Soc. Am.*, 75, 1765-1782.

Vidale, J.E. and R.W. Clayton, (1986). A stable free-surface boundary condition for 2-D elastic finite-difference wave simulation, to appear in December, *Geophysics.*

Whitcomb, J.H., C.R. Allen, J.D. Garmany, and J.A. Hileman (1973). San Fernando earthquake series, 1971: Focal mechanisms and tectonics,

Rev. Geophys. Space Phys., 11, 693-730.

Witte, D., P.G. Richards, (1986). Anelastic wave propagation by the pseudo-spectral method, *Trans. AGU*, 67, 303.

Table 1 : Velocity and density structure for the cross-section in the middle of the San Fernando basin

P-wave velocity	S-wave velocity	Density
1.2	0.6	1.7
2.0	1.1	1.8
2.5	1.4	1.9
3.1	1.8	2.1
4.3	2.5	2.3
5.5	3.2	2.5
6.1	3.5	2.7
6.9	4.0	2.9
7.3	4.2	2.9

Table 2 : Source parameters of the San Fernando earthquake

Study Method		Strike	Dip	Rake	Depth km	Moment X 10^{26} dyne-cm
Whitcomb(1973)		-67°	52°	72°	8	-
First motions						
Alewine(1974)		-67°	53°	72°	0–14	1.0-2.2
Static displacements						
Alewine(1974)		-67°	53°	66–82°	0–15	1.7
Surface waves						
Langston(1978)	first source	-79°	44°	80°	15	0.53
Teleseismic records	second source	-80°	18°	96°	10	0.32
Langston(1978)	first source	-70°	53°	76°	8–15	0.41
Teleseismic records	second source	-80°	29°	90°	0–10	0.45
Heaton(1982)	first source	-70°	54°	76°	3–16	0.7
combined study	second source	-75°	45°	90°	0–10	1.0

FIGURE CAPTIONS

Figure 1. Map and cross-section of the San Fernando region from Duke et al. (1971). The epicenter is marked by a cross. The surface breakage is indicated by the cross-hatched line. The filled triangles are the locations of the strong-motion instruments used in this section. Cross-hatched areas show surface exposure of bedrock. The bottom of the basin for the profile A-A' is shown below, where dashed portions show where the boundary is not known. The cross-section has vertical exageration of 2:1. SFB indicates the San Fernando basin, SMM the Santa Monica mountains, LAB the Los Angeles basin, PVH the Palos Verdes hills, and PO the Pacific ocean.

Figure 2a. Velocity records of the 1971 San Fernando earthquake, taken from EERL (1974). The traces are aligned relative to a high-frequency, early arrival on the vertical component that is interpreted to be a direct compressional wave. Amplitude is given in cm/sec. The station names are listed at the far left. The stations are shown in order of increasing epicentral distance, but the actual station spacing is irregular. Figure 2b. Smoothed velocity records. The records shown in Figure 2a are convolved by a gaussian pulse about one second wide to filter out frequencies that cannot be properly handled by the finite-difference grid.

Figure 3. Stratigraphic and structural cross-section of the profile from the San Gabriel mountains on the left, across the San Fernando basin, the Santa Monica mountains, and the Los Angeles basin, to the Palos Verdes hills on the right. The stratigraphy, the velocities, and the densities are taken from Duke et al. (1971), except that the velocities below the basins are taken from Kanamori and Hadley (1975). The heavy vertical lines in the stratigraphy diagram indicate the location of well logs used by Duke et al. (1971) to construct the model. Only the shear wave velocity is shown, the compressional wave velocity and the density corresponding to each shear wave velocity are given in Table 1. The letters B, D, I, and S correspond to the locations of the bottommost, deep, intermediate, and shallow sources discussed in the text. The triangles along the surface mark the location of the receivers for the finite difference seismograms. The vertical exaggeration is 2:1.

Figure 4. Schematic north-south cross-section of results from teleseismic body wave studies. Langston (1978) interprets the faulting of the San Fernando earthquake as two point sources in Figure 4a and as two finite segments in Figure 4b. The moment is assumed to be uniformly distributed with depth for each source in Figure 4b. Heaton (1982) combines the teleseismic data, near-field data on hard rock sites, and static data to find the two non-intersecting finite fault segments shown in Figure 4c. The moment is assumed to be non-uniformly distributed with depth for each

source in Figure 4c. Details of these models may be found in Table 2.

Figure 5. Green's functions for the transverse component of velocity with S and I source locations. The strike-slip case corresponds to $A_4 = 1$ and $A_5 = 0$, and the dip-slip case corresponds to $A_4 = 0$ and $A_5 = 1$. Moment scaling is discussed in the text. The source time function is impulsive, and the frequency content is limited by the seismic Q of 25.

Figure 6. Green's functions for the transverse component of velocity with the D and B source locations. The strike-slip case corresponds to $A_4 = 1$ and $A_5 = 0$, and the dip-slip case corresponds to $A_4 = 0$ and $A_5 = 1$. Moment scaling is discussed in the text. The source time function is impulsive, and the frequency content is limited by the seismic Q of 25.

Figure 7a. Finite-difference seismograms for the transverse component of velocity for the model with flat layers of the thickness and velocities appropriate for the middle of the San Fernando basin in Figure 3, listed in Table 1. The source has a gaussian time function 3.0 seconds in width that is shown in Figure 8c. The mechanism is strike-slip and the moment scaling is discussed in the text. Velocities are in cm/sec. Figure 7b. Finite difference velocity seismograms for the model shown in Figure 3. The source has the same time function 3.0 seconds in width as Figure 7a. The mechanism is strike-slip. The location of the shallow, intermediate, and deep depth sources are indicated in Figure 3.

Figure 8. The calculation of an empirical source time function for the deep source. Figure 8a shows the observed transverse velocity waveform at the Santa Monica mountains station D068. Figure 8b shows the displacement waveform at station D068. Predictions of secondary arrivals by Heaton (1982) and Langston (1978) are indicated by the H and L above the trace. Figure 8c shows the gaussian time function assumed in the construction of the synthetics shown in Figure 7.

Figure 9. Comparison of filtered transverse component of data with FD seismograms computed with the empirical time function shown in Figure 8. The heavy traces show the data, with the station name to the left and the amplitude in cm/sec to the right. The light traces show the FD seismograms, with the range in km to the left and the amplitude to the right. The FD seismograms assume point source D in the structure shown in Figure 3, and a Q of 25. The source time function is chosen and the source amplitude is scaled so that the waveform and amplitude of the synthetic seismogram at the ridge station (30 km) matches that of station D068.

Figure 10. Vertical and radial Green's functions for source D. The strike-slip case corresponds to $A_1 = 1$, $A_2 = 0$, and $A_3 = 0$. The dip-slip case corresponds to $A_1 = 0$, $A_2 = 1$, and $A_3 = 0$. The 45° dip-slip case

corresponds to $A_1 = 0$, $A_2 = 0$, and $A_3 = 1$. The moment for each Green's function is 10^{20} dyne-cm. The frequency content is limited mostly by the seismic Q of 25.

Figure 11. Comparison of filtered vertical component of data with FD seismograms computed with the empirical time function shown in Figure 8. The heavy traces show the data, with the station name to the left and the amplitude in cm/sec to the right. The light traces show the FD seismograms, with the range in km to the left and the amplitude to the right. The data is lined up on a high-frequency arrival on the vertical component that is presumably a direct compressional wave. The FD seismograms assume a point source at the location D (10 km depth) in Figure 3; they are computed with the structure shown in Figure 3, and a Q of 25 is assumed. The amplitudes of the finite difference seismograms are consistent with those for the transverse component in Figure 9.

Figure 12. Comparison of filtered radial component of the data with FD seismograms computed with the empirical time function shown in Figure 8. The heavy traces show the data, with the station name to the left and the amplitude in cm/sec to the right. The light traces show the FD seismograms, with the range in km to the left and the amplitude to the right. The data is lined up on a high-frequency arrival on the vertical component that is presumably a direct compressional wave. The FD seismograms assume a point source at the location D (10 km depth) in Figure 3; they are computed with the structure shown in Figure 3, and a Q of 25 is assumed. The amplitudes of the finite difference seismograms are consistent with those for the transverse component in Figure 9.

Figure 13. Peak velocity attenuation with distance. The crosses show the peak velocity of the smoothed data versus offset. The line shows the attenuation for the FD simulation of the motions.

Figure 14. A seismic section of the envelope of the transverse component of velocity across the San Fernando and Los Angeles basins. Dark portions of the images have energy in the velocity traces; light portions have little or no energy at that time. 250 receivers are used, rather than the eight shown up to this point. The same source is used as in Figure 8. The major geologic structures are sketched below the section, where SFB indicates the San Fernando basin, SMM the Santa Monica mountains, and LAB the Los Angeles basin.

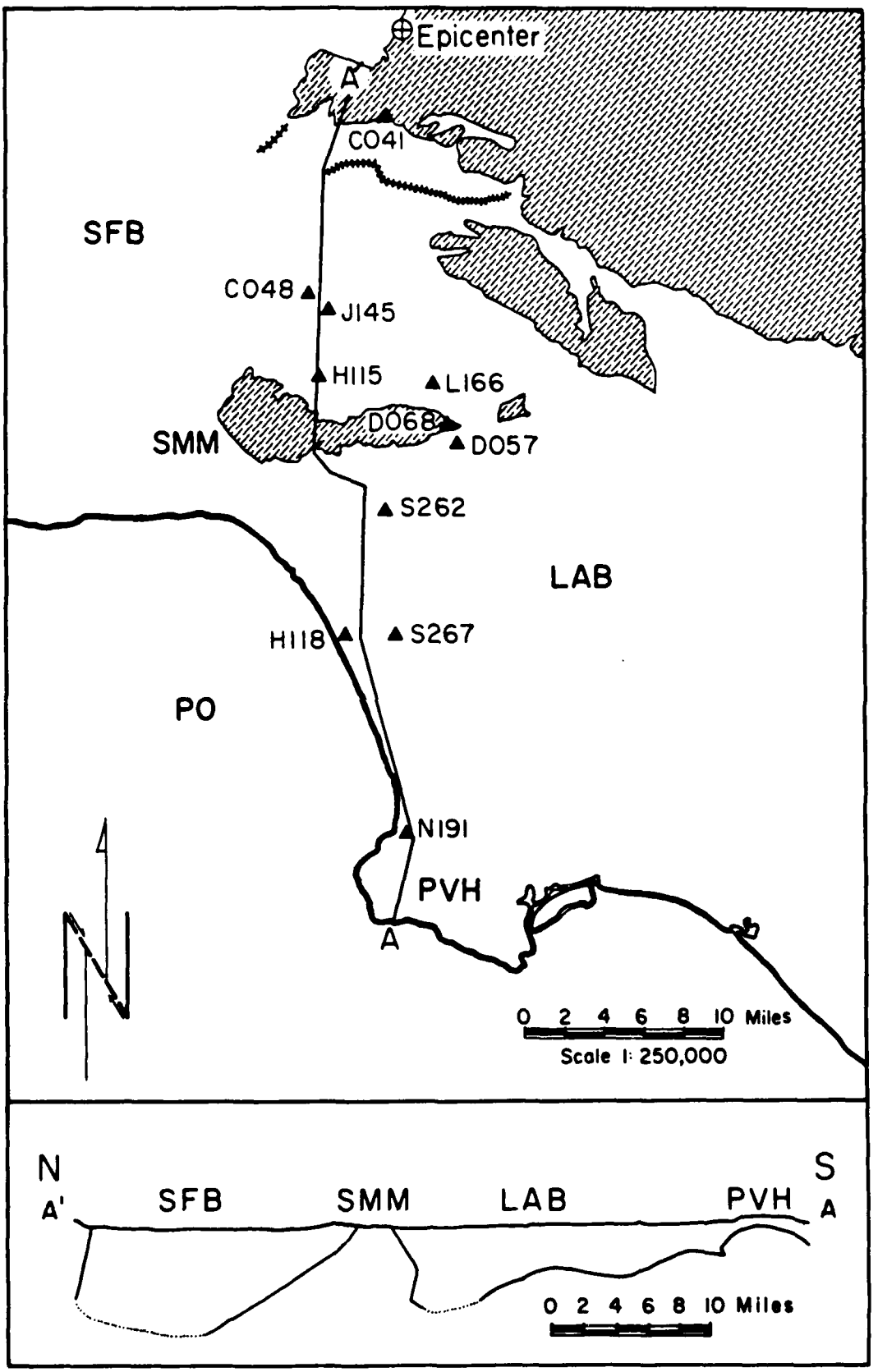
Epicenter
A
C041
SFB
C048
J145
H115
L166
D068
D057
SMM
S262
LAB
H118
S267
PO
N191
PVH
A
0 2 4 6 8 10 Miles
Scale 1: 250,000
N
A'
SFB
SMM
LAB
PVH
S
A
0 2 4 6 8 10 Miles

Figure 1

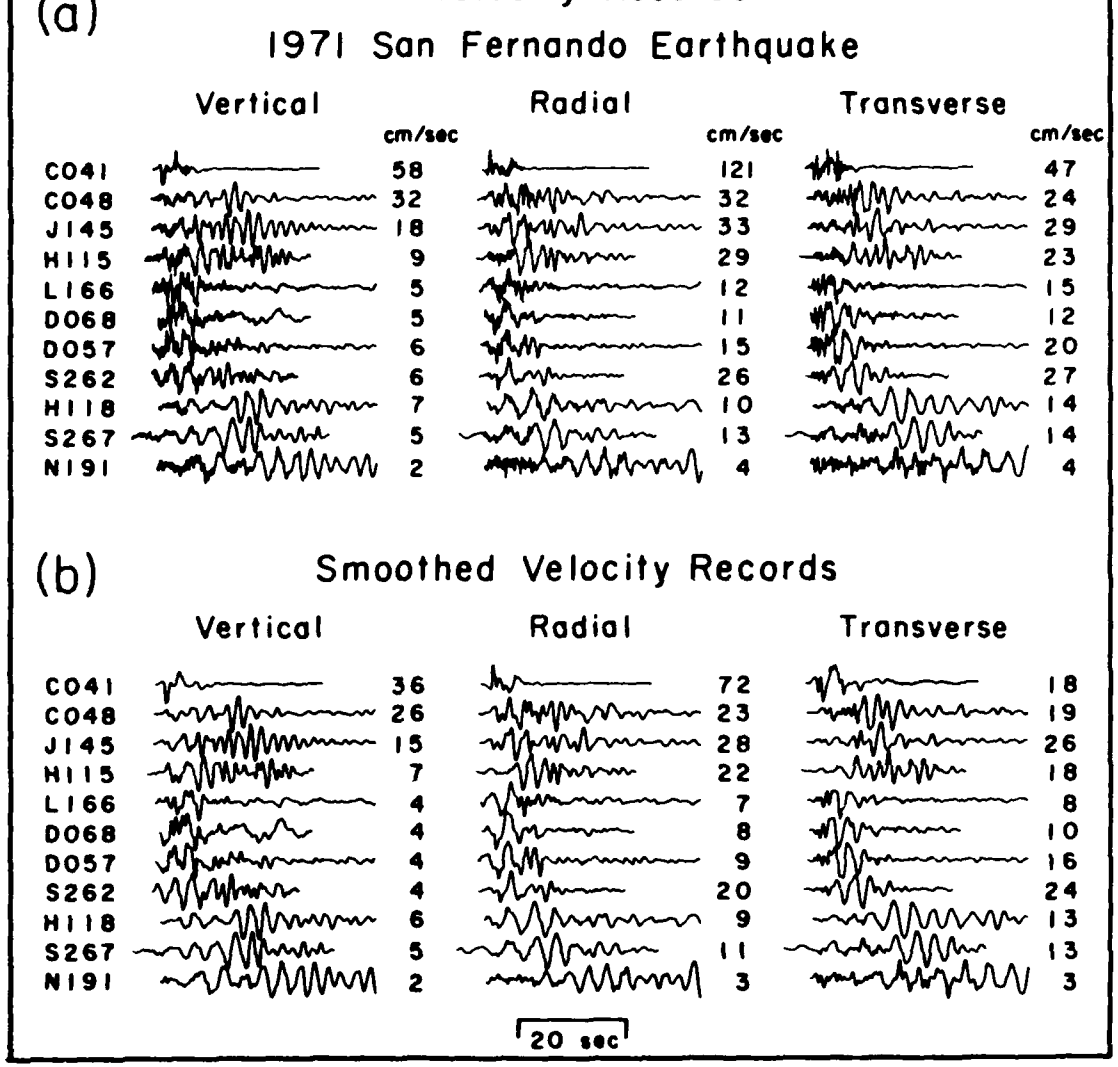
(a)
Velocity Records
1971 San Fernando Earthquake
Vertical
Radial
Transverse
cm/sec
cm/sec
cm/sec
C041 58 121 47
C048 32 32 24
J145 18 33 29
H115 9 29 23
L166 5 12 15
D068 5 11 12
D057 6 15 20
S262 6 26 27
H118 7 10 14
S267 5 13 14
N191 2 4 4
(b)
Smoothed Velocity Records
Vertical
Radial
Transverse
C041 36 72 18
C048 26 23 19
J145 15 28 26
H115 7 22 18
L166 4 7 8
D068 4 8 10
D057 4 9 16
S262 4 20 24
H118 6 9 13
S267 5 11 13
N191 2 3 3
20 sec

Figure 2

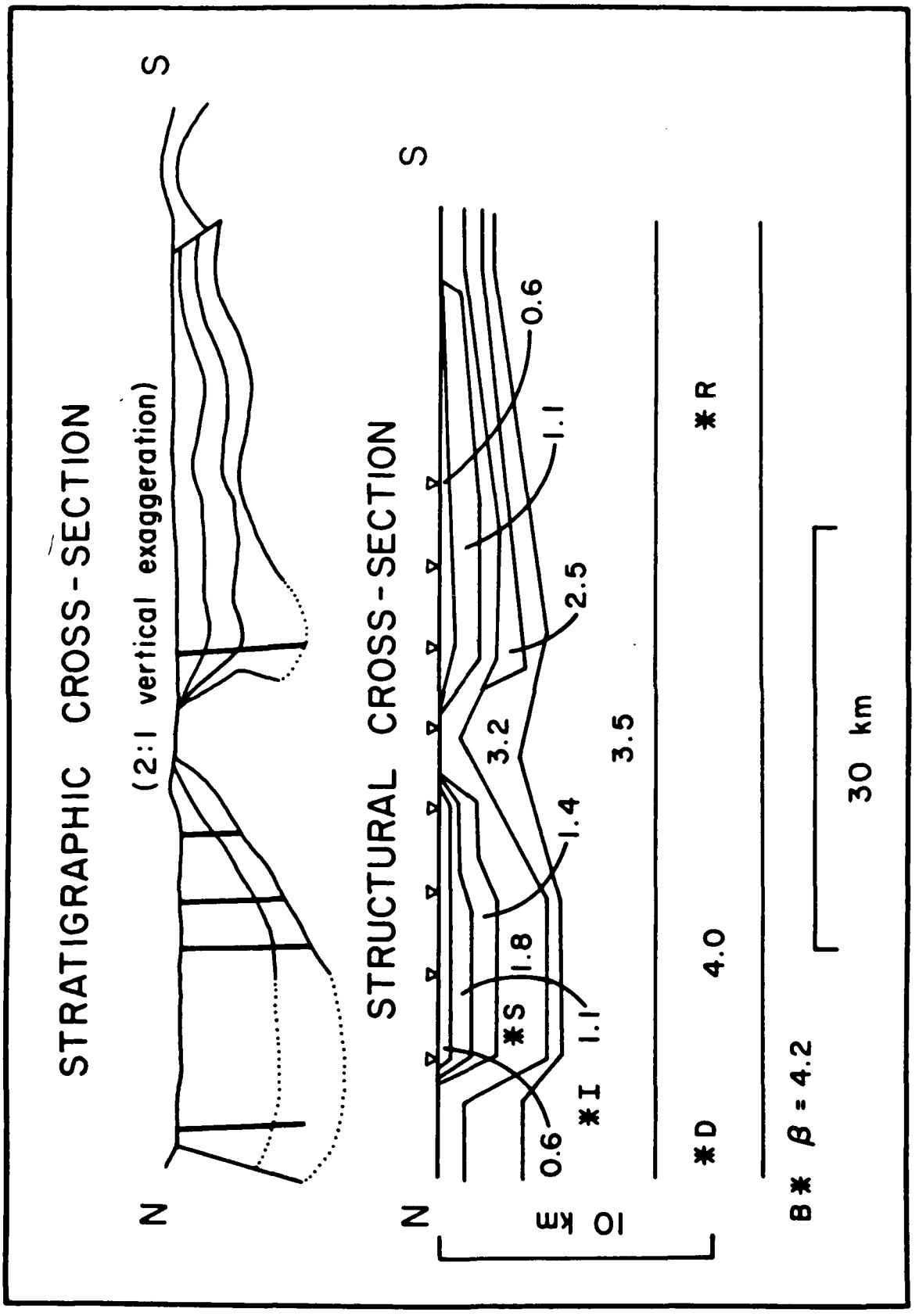
STRATIGRAPHIC CROSS-SECTION
(2:1 vertical exaggeration)
S
N
STRUCTURAL CROSS-SECTION
S
N
10 km
30 km
0.6
1.1
2.5
3.2
1.4
3.5
1.8
*S
1.1
*I
0.6
*D
4.0
*R
B* β = 4.2

Figure 3

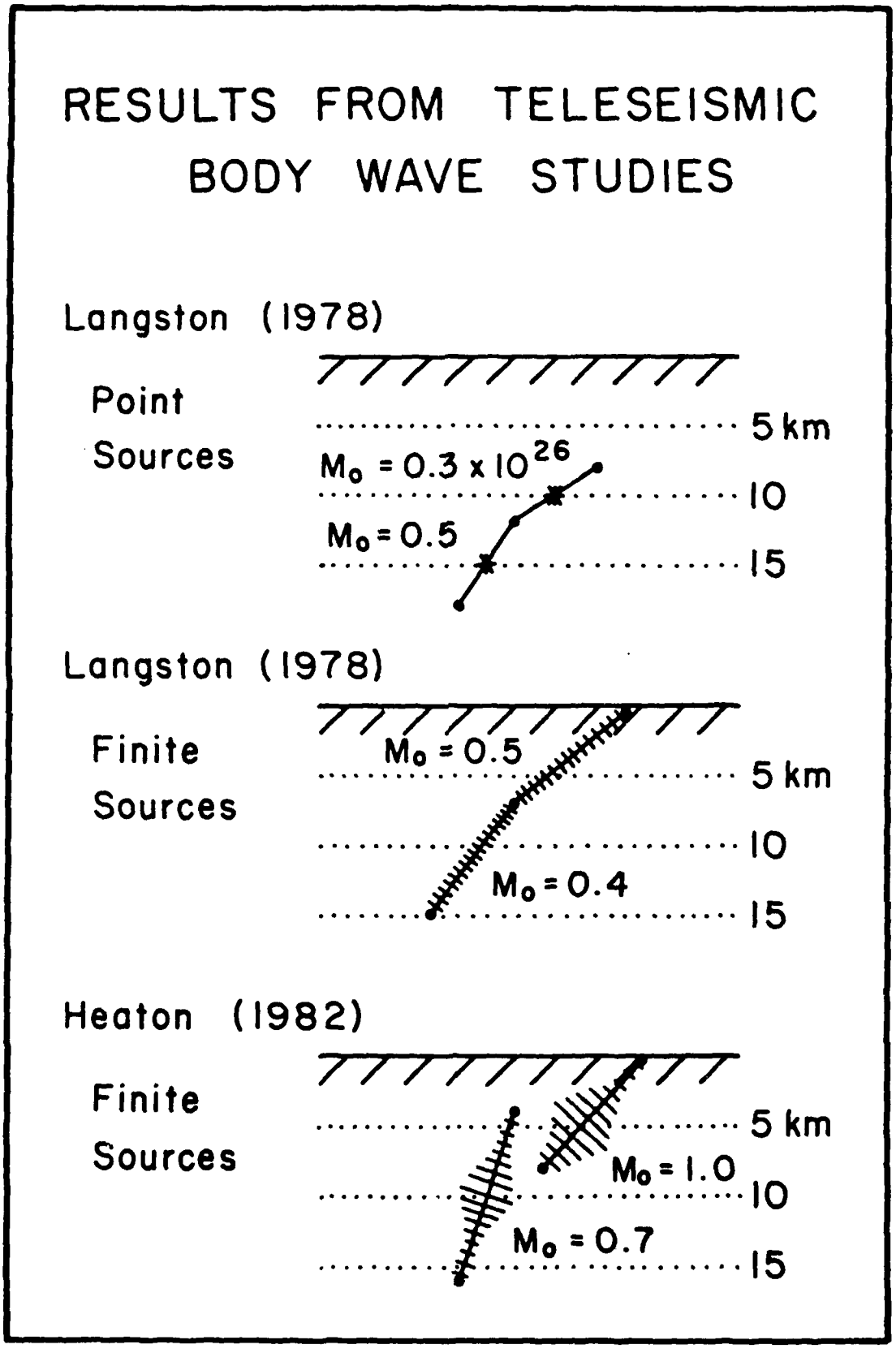
RESULTS FROM TELESEISMIC BODY WAVE STUDIES
Langston (1978)
Point Sources
$M_o = 0.3 \times 10^{26}$
$M_o = 0.5$
5 km
10
15
Langston (1978)
Finite Sources
$M_o = 0.5$
$M_o = 0.4$
5 km
10
15
Heaton (1982)
Finite Sources
$M_o = 1.0$
$M_o = 0.7$
5 km
10
15

Figure 4

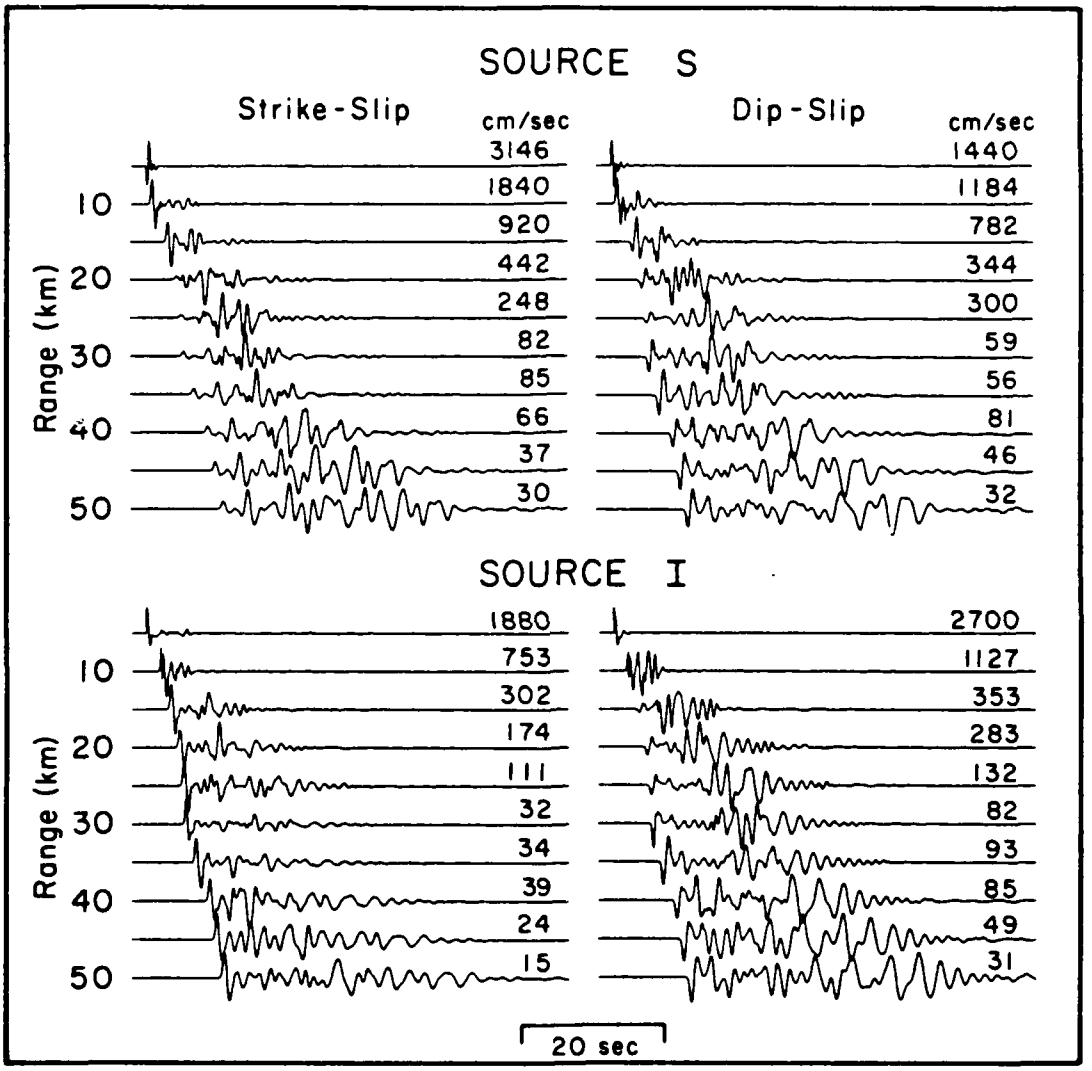
SOURCE S
Strike-Slip
cm/sec
3146
1840
920
442
248
82
85
66
37
30
Dip-Slip
cm/sec
1440
1184
782
344
300
59
56
81
46
32
Range (km)
10
20
30
40
50
SOURCE I
1880
753
302
174
111
32
34
39
24
15
2700
1127
353
283
132
82
93
85
49
31
20 sec

Figure 5

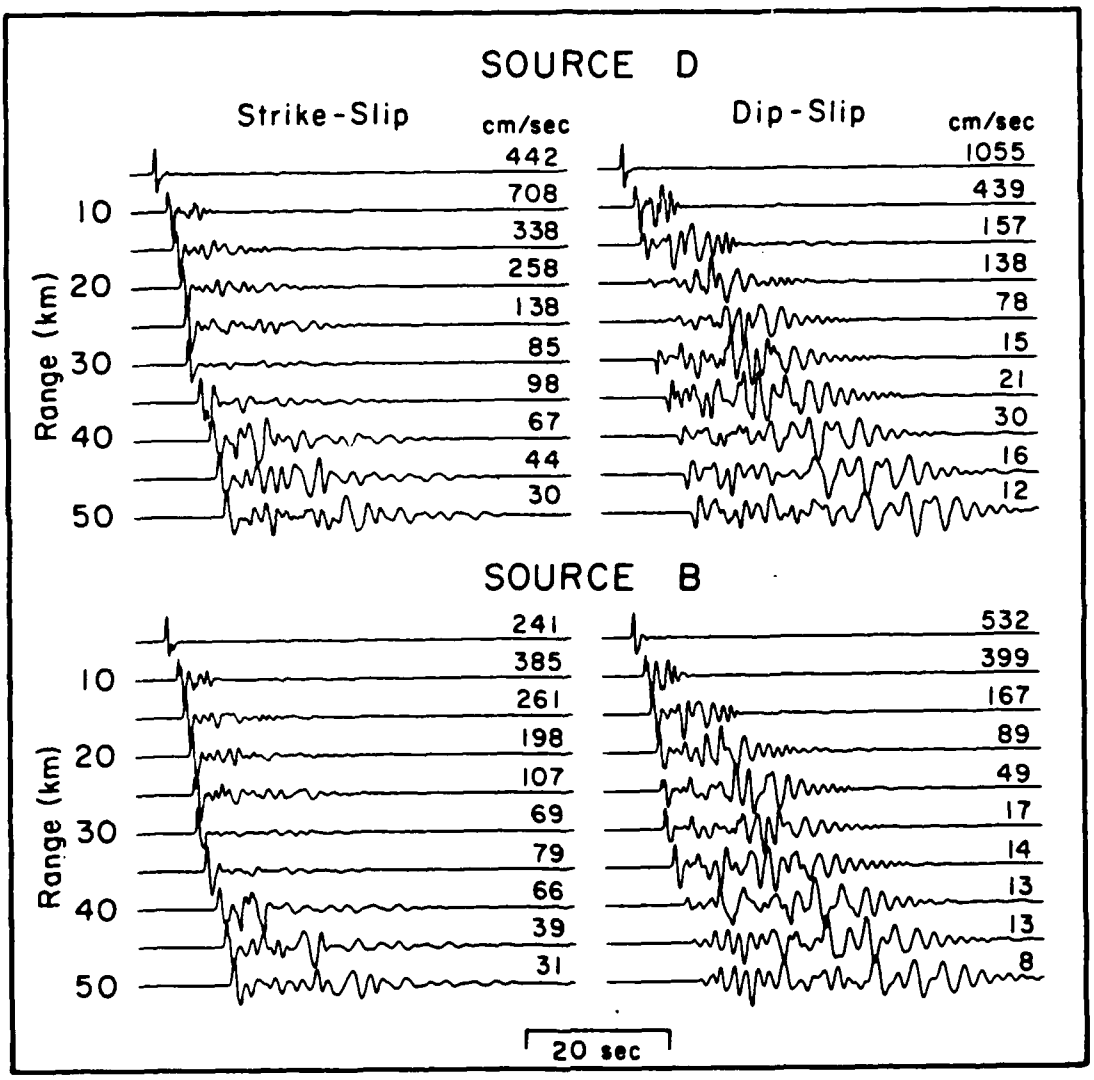
SOURCE D
Strike-Slip
cm/sec
442
708
338
258
138
85
98
67
44
30
Dip-Slip
cm/sec
1055
439
157
138
78
15
21
30
16
12
Range (km)
10
20
30
40
50
SOURCE B
241
385
261
198
107
69
79
66
39
31
532
399
167
89
49
17
14
13
13
8
20 sec

Figure 6

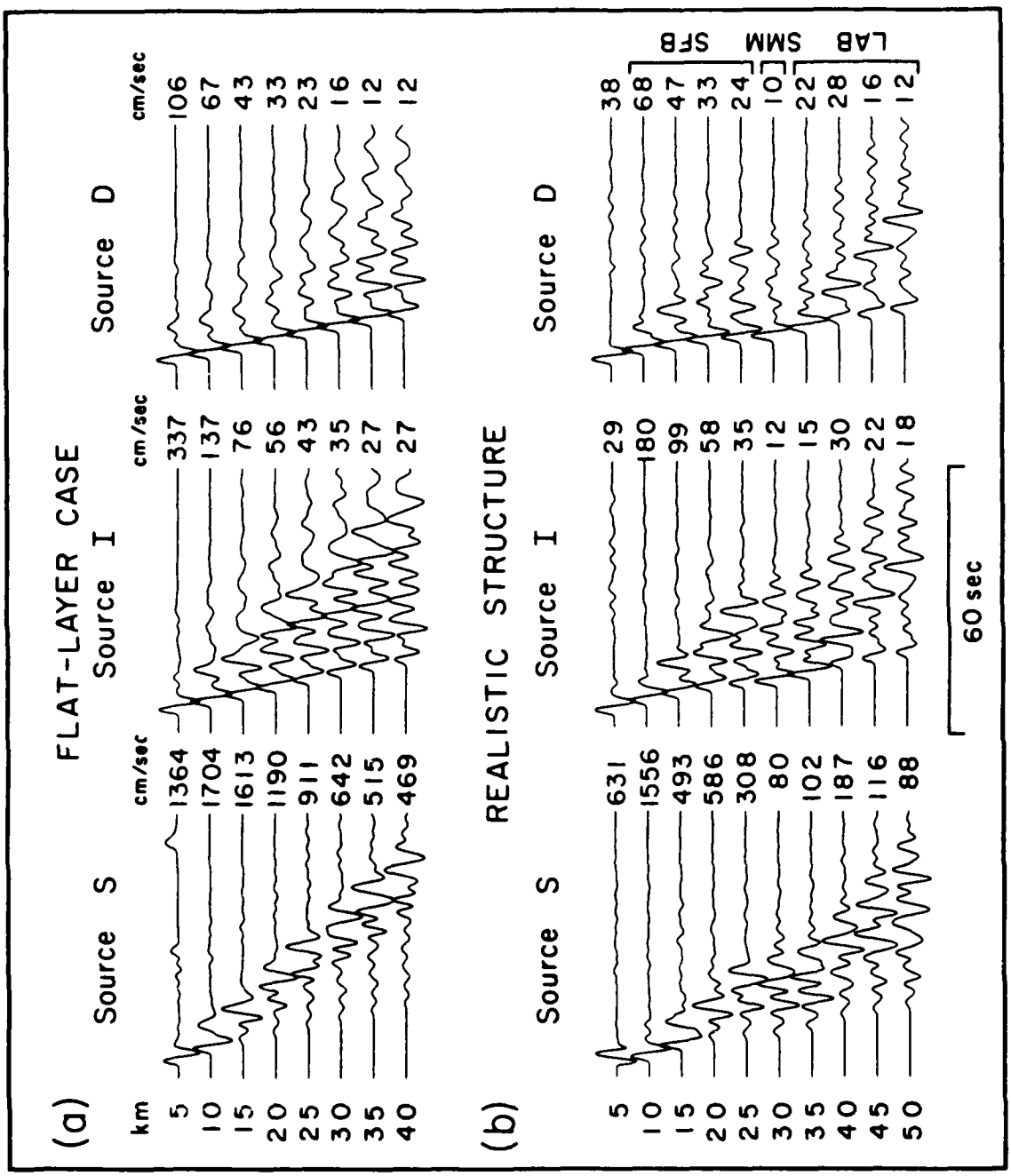
(a)
FLAT-LAYER CASE
Source S
Source I
Source D
km
cm/sec
cm/sec
cm/sec
5 1364 337 106
10 1704 137 67
15 1613 76 43
20 1190 56 33
25 911 43 23
30 642 35 16
35 515 27 12
40 469 27 12
(b)
REALISTIC STRUCTURE
Source S
Source I
Source D
LAB SMM SFB
5 631 29 38
10 1556 180 68
15 493 99 47
20 586 58 33
25 308 35 24
30 80 12 10
35 102 15 22
40 187 30 28
45 116 22 16
50 88 18 12
60 sec

Figure 7

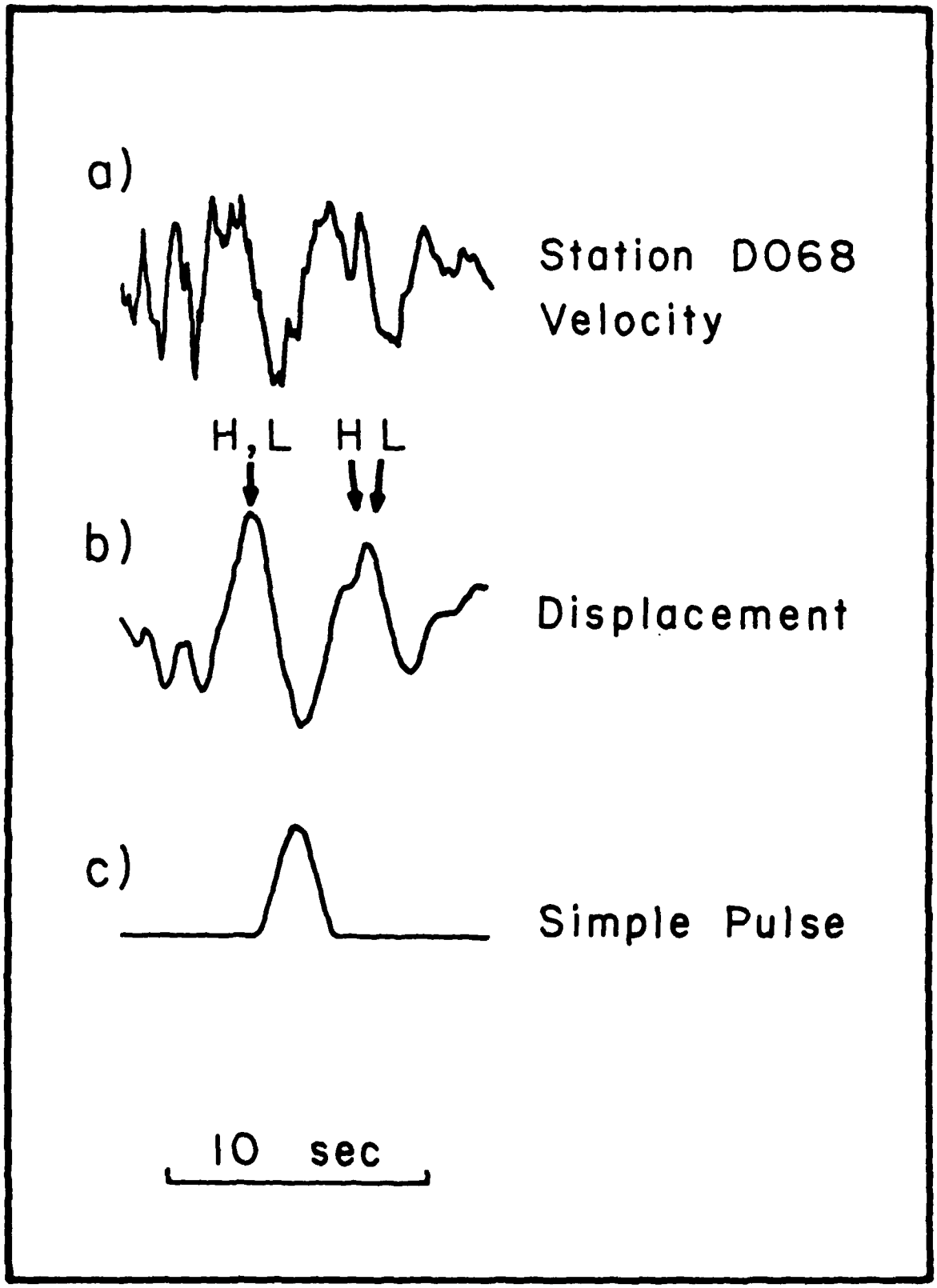
a)
Station D068
Velocity
H, L H L
b)
Displacement
c)
Simple Pulse
10 sec

Figure 8

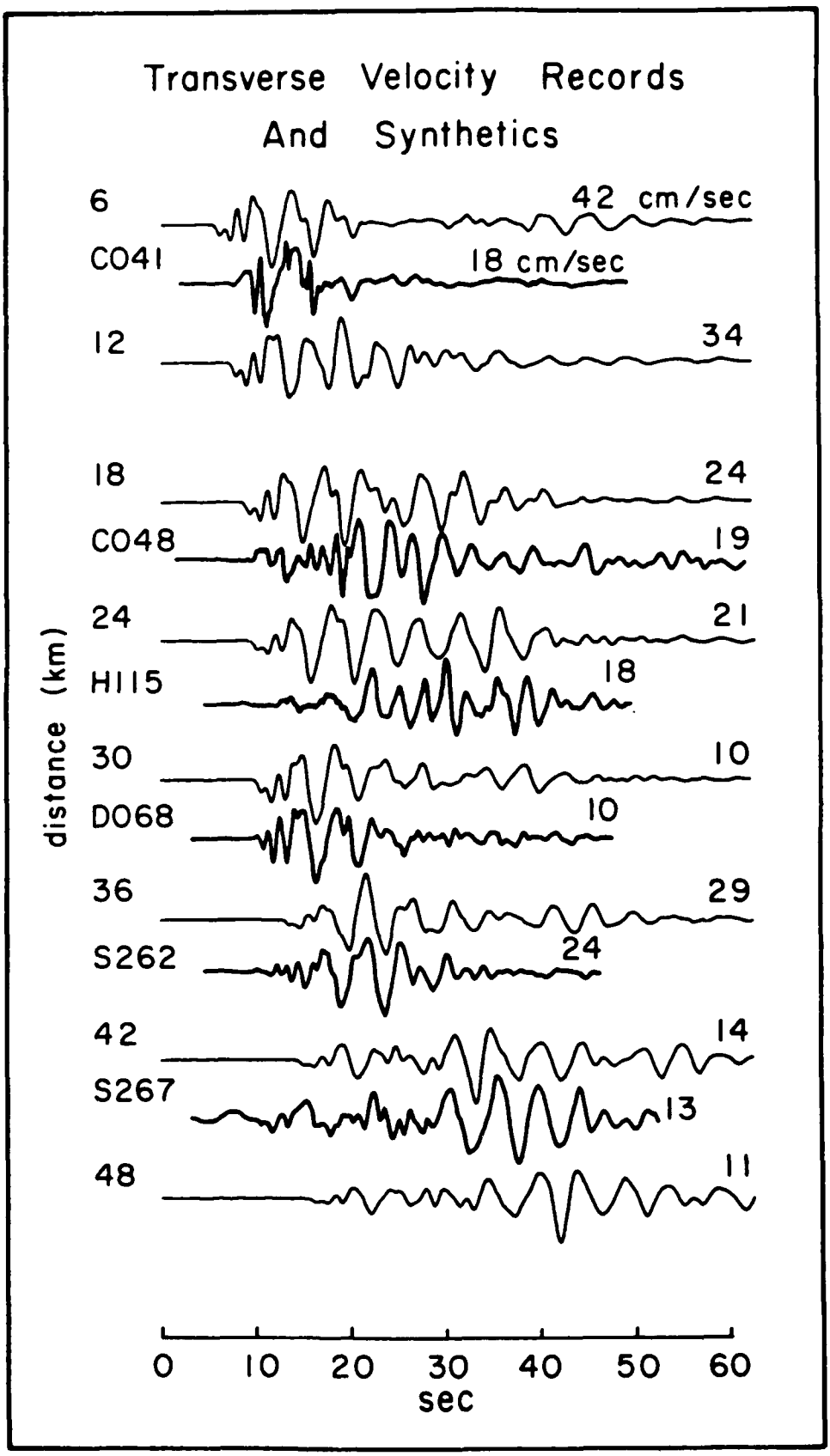
Transverse Velocity Records
And Synthetics
6
42 cm/sec
C041
18 cm/sec
12
34
18
24
C048
19
24
21
H115
18
30
10
D068
10
36
29
S262
24
42
14
S267
13
48
11
distance (km)
0
10
20
30
40
50
60
sec

Figure 9

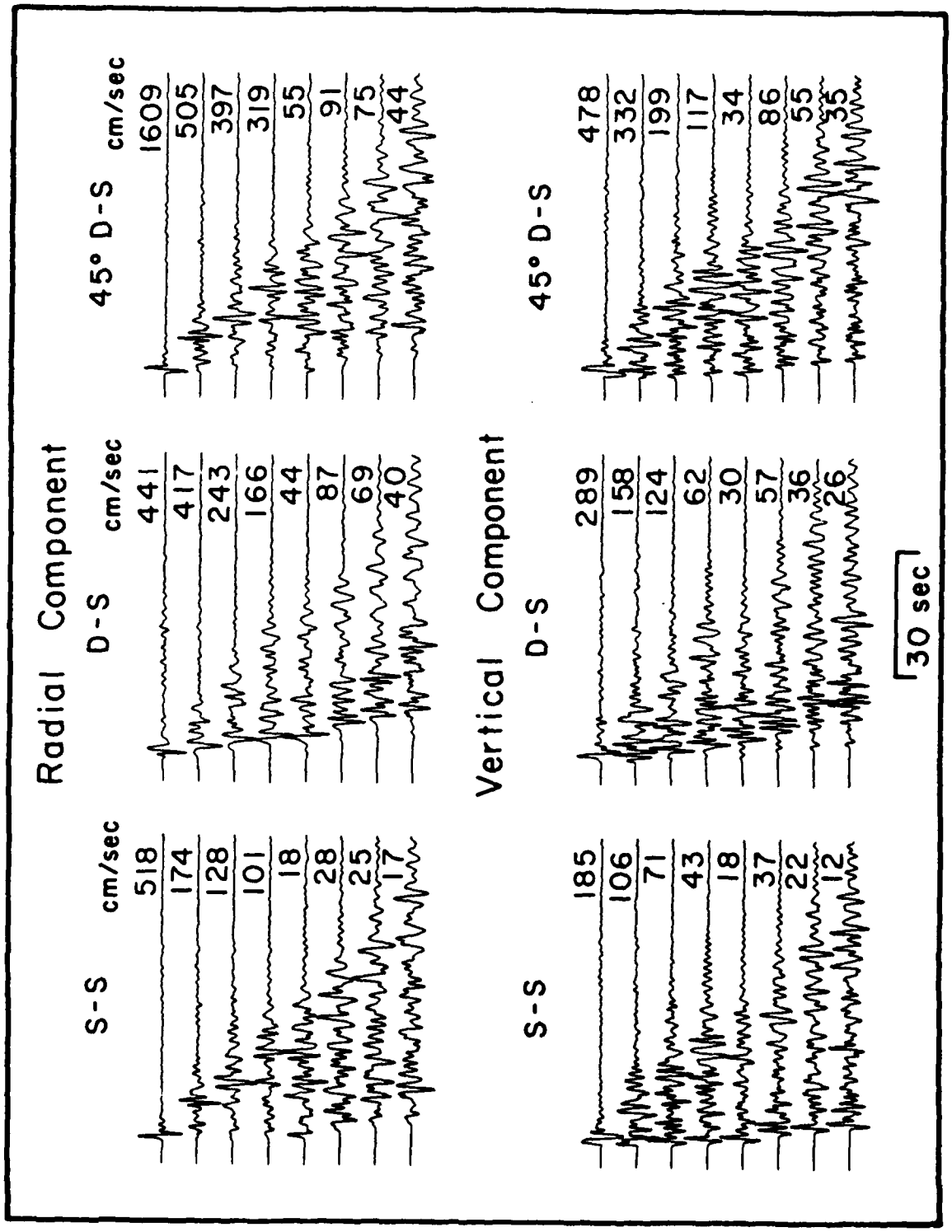
Radial Component
S-S cm/sec
518
174
128
101
18
28
25
17
D-S cm/sec
441
417
243
166
44
87
69
40
45° D-S cm/sec
1609
505
397
319
55
91
75
44
Vertical Component
S-S
185
106
71
43
18
37
22
12
D-S
289
158
124
62
30
57
36
26
45° D-S
478
332
199
117
34
86
55
35
30 sec

Figure 10

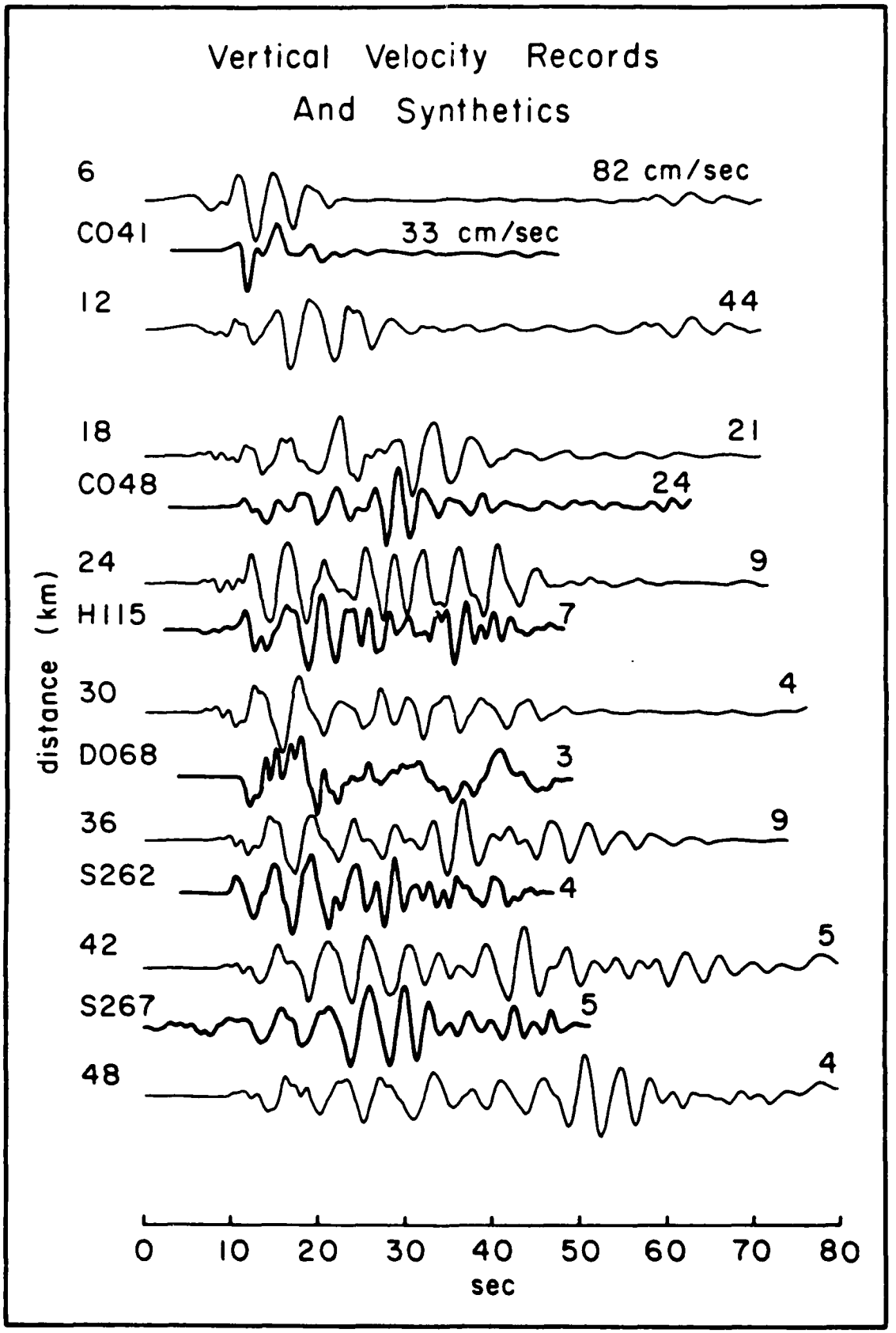
Vertical Velocity Records
And Synthetics
6
82 cm/sec
C041
33 cm/sec
12
44
18
21
C048
24
24
9
H115
7
30
4
D068
3
36
9
S262
4
42
5
S267
5
48
4
distance (km)
0
10
20
30
40
50
60
70
80
sec

Figure 11

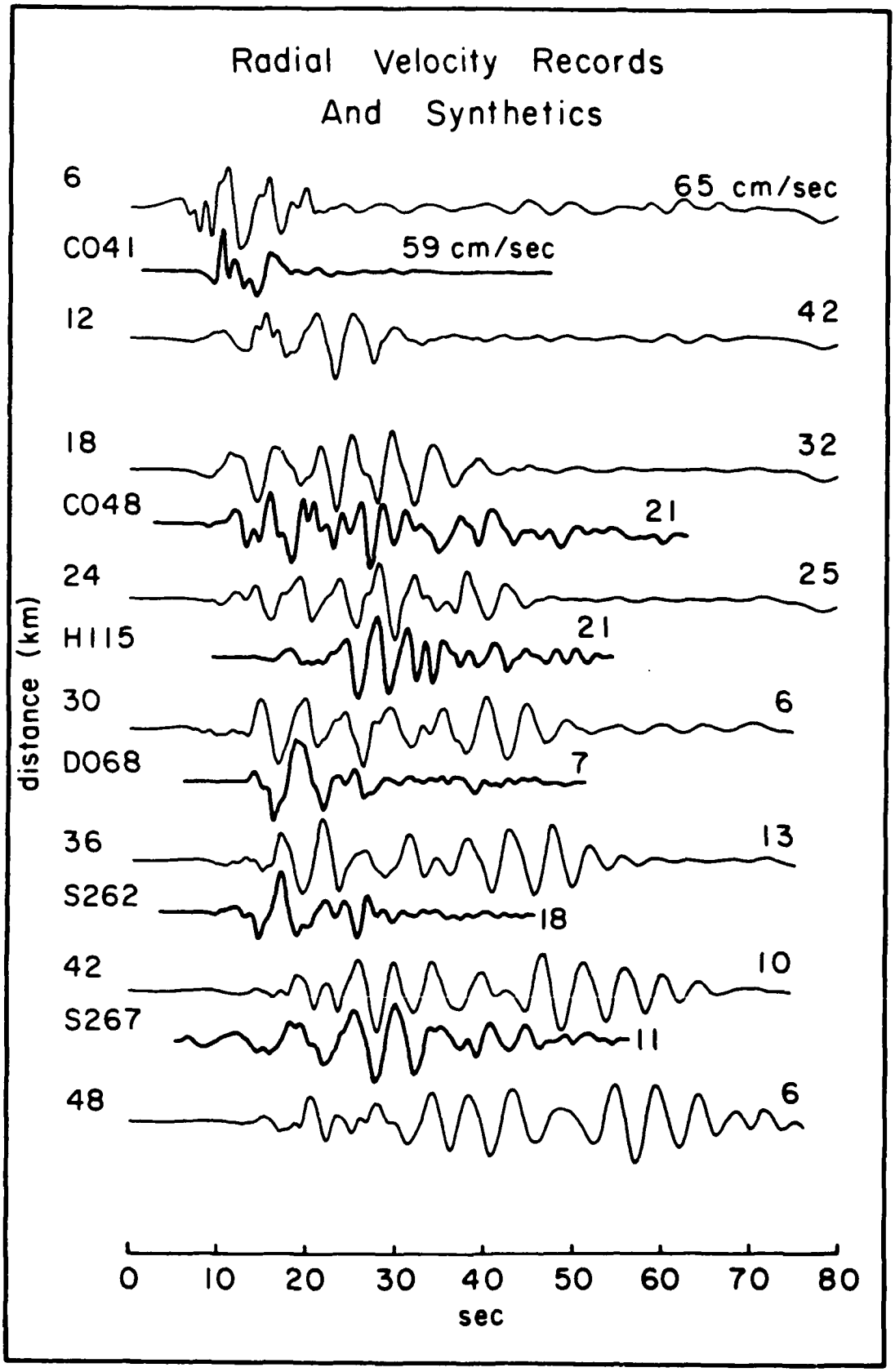
Radial Velocity Records
And Synthetics
6
65 cm/sec
C041
59 cm/sec
12
42
18
32
C048
21
24
25
H115
21
30
6
D068
7
36
13
S262
18
42
10
S267
11
48
6
distance (km)
0
10
20
30
40
50
60
70
80
sec

Figure 12

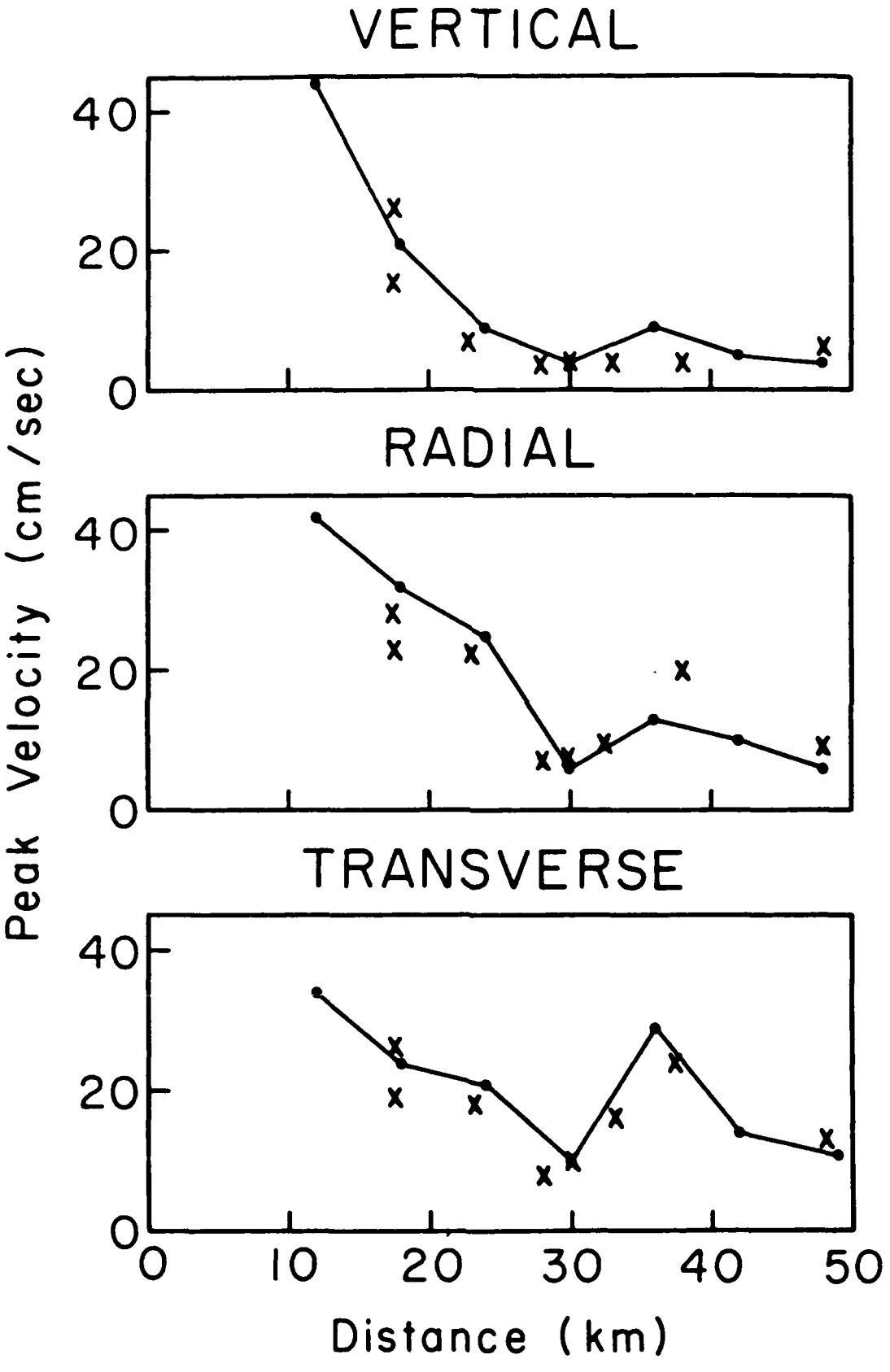
VERTICAL
RADIAL
TRANSVERSE
Peak Velocity (cm/sec)
0
20
40
0
10
20
30
40
50
Distance (km)

Figure 13

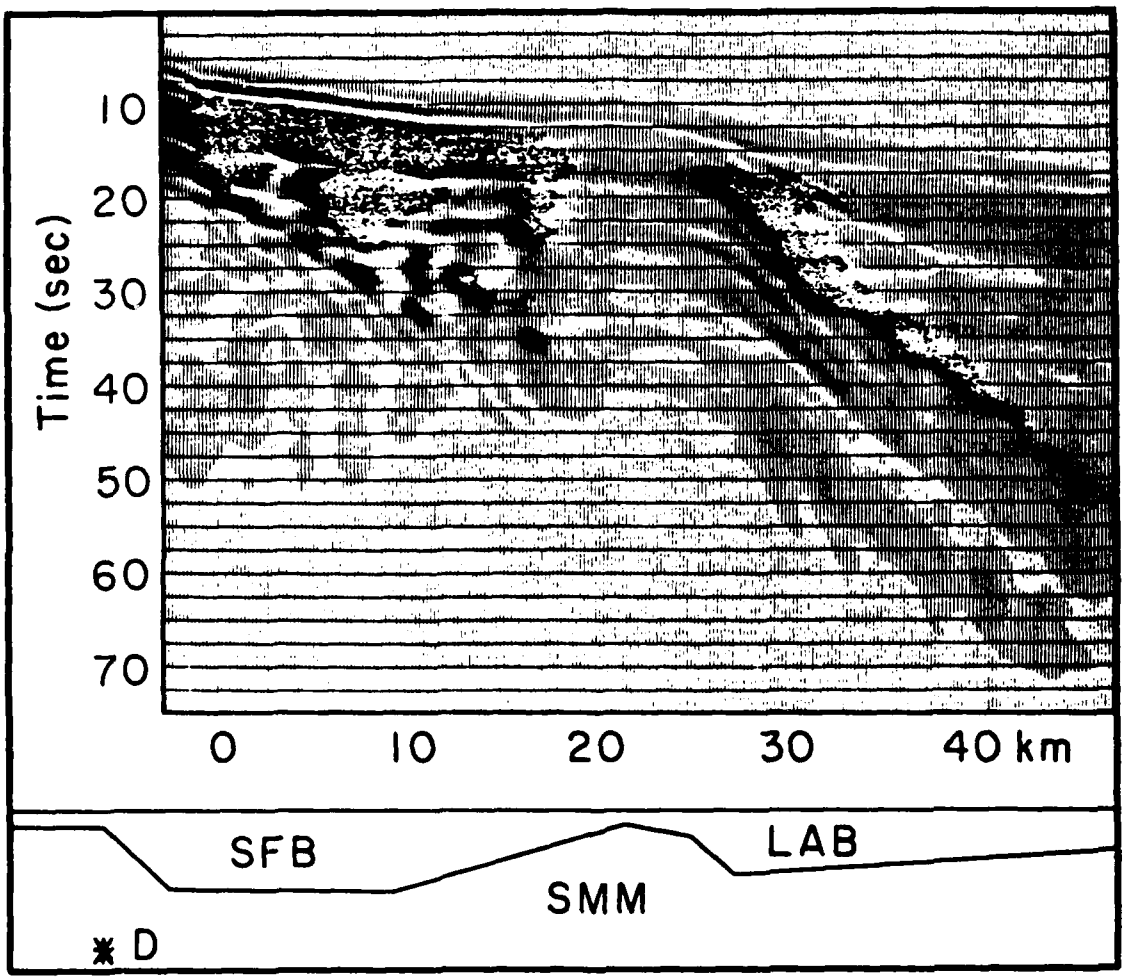

Figure 14

Numerical Studies of Propagation of L_g Waves across Ocean Continent Boundaries Using the Representation Theorem

Thesis by

Janice Regan

Table of Contents

Acknowledgements

Many thanks to my thesis advisor, David G. Harkrider, for guidance, support, and encouragement. Thanks, also to the students, faculty, and staff of the Seismo. Lab. for their friendship and encouragement.

This research has been sponsored by the Defense Advanced Research Projects Agency (DOD) with technical management by the Air Force Geophysics Laboratory under Contract # F19628-85-K-0017.

Abstract

The methods for Representation Theorem (RT) coupling of finite element (FE) or finite difference calculations and Harkrider's (Harkrider 1964, 1970) propagator matrix method calculations to produce a hybrid method for propagation of SH mode sum seismograms across paths that contain regions of non plane-layered structure are explained and developed. The coupling methods explained in detail use a 2-D Cartesian FE formulation. Analogous methods for the 3-D method follow directly. Extensive tests illustrating the validity and accuracy of the implementation of these coupling methods are discussed. These hybrid techniques are developed to study the propagation of surface waves across regional transition zones or other heterogeneities that exist in part of a longer, mostly plane-layered, path. The effects of a thinning or thickening of the crustal layer on *the* propagation of L_g mode sum seismograms have been examined in this study. The thinning or thickening of the crustal layer is used as a simple model of ocean continent transitions. The L_g phase is of particular interest since it is used in several important applications such as mapping the extent of continental crust, magnitude determination, and discrimination between explosive and earthquake sources. The understanding of the observations that L_g wave is attenuated completely when the propagation path includes an oceanic portion of length greater than one hundred to two hundred kilometers or a region of complex crustal structure is not complete, and a clear explanation of these phenomena could have important consequences for all these types of studies. The transition model calculations done in this study show that passage through a region of thinning crustal thickness, the model for a continent to ocean transition, increases the amplitude and coda length of the L_g wave at the surface, and allows much of the modal energy

trapped in the crust, which forms the L_g phase, to escape into the subcrustal layers as body waves or other downgoing phases. The magnitude of both these effects increases as the length of the transition increases or the slope of the layer boundaries decrease. The passage of the wavefront exiting the continent to ocean transition region through the oceanic structure allows further energy to escape from the crustal layer, and produces a decrease in L_g amplitude at the surface as the length of the oceanic path increases. The amplitude decrease is maximum near the transition region and decreases with distance from it. Passage through a region of thickening crust, the model of a ocean to continent transition, causes a rapid decrease in the L_g amplitude at the surface of the crust. The energy previously trapped in the oceanic crustal layer spreads throughout the thickening crustal layer, and any amplitude which has been traveling through the subcrustal layer but has not reached depths below the base of the continental crust is transmitted back into the continental crust. The attenuation of L_g at the crustal surface along a partially oceanic path occurs in the oceanic structure and in the ocean to continent transition region. The attenuation at the surface depends in part on the escape of energy at depth through the continent to ocean transition region into the underlaying half-space. The total attenuation of Lg due to propagation through a forward transition followed by a reverse transition is at most a factor of four to six. This is inadequate to explain the observed attenuation of Lg. Thus, additional effects, other than geometry must be considered to provide a complete explanation of the attenuation of Lg.

Introduction

This thesis presents a study of the propagation of L_g waves across ocean continent transition regions. The transition regions are represented by a simplified model consisting of a crustal layer with thickness that increases or decreases smoothly between oceanic and continental values. The distance over which this smooth variation occurs is referred to as the length of the transition region. The changes to a L_g wavefield, when it travels through one of these simple transition regions, are modeled using a hybrid method which is explained and developed in sections four, five, and six of chapter one. The hybrid method combines the Finite Element method and the Propagator Matrix technique through application of the Seismic Representation Theorem. These two methods are explained and the notation associated with them is defined in section two and three of chapter one. In the regions of complex structure, those regions containing the transition regions, the Finite Element method is used to transmit the L_g waves. In the regions of plane layered structure either the Propagator Matrix technique is used to directly determine the seismograms for a source in the layers being considered, or it is used to determine the Green's functions for propagation from the interface between the complex region and the layered region to the receiver. In the first case, displacement time histories are determined at a set of points equally spaced in depth along a vertical plane. These time histories are used as boundary conditions for the Finite Element method. Extensive tests of the accuracy of producing a Finite Element wavefield by specifying the displacements as a function of time along the vertical plane defining the Finite Element grid edge are presented in sections seven and eight of chapter one. The results of these tests are useful in understanding the sources of uncertainty due to truncation of the vertical plane at some depth less than infinity. In the case where the propagator method is used to determine Green's functions the Green's functions are combined with the stress and displacement time histories recorded at the boundary between the plane layered region

and the complex region according to the Representation Theorem. Tests of the validity and accuracy of this method of coupling are discussed in section two of chapter three. The results of the study on the effects of transition length on the propagation of L_g waves are reported, discussed and interpreted in chapter two. The results of the study of the effects of the length of the intermediate oceanic path on the propagation of L_g are mentioned in chapter two and again in the first and last sections of chapter three. In order to understand why the models used were chosen for this study, and why this study is important, it is useful to discuss and review the the different types of studies that use L_g data. In the remainder of this section the background of the problem will be discussed.

In order to choose a reasonable form for a simple model of a ocean continent or continent ocean transition region it is useful to examine existing observations of such regions. Structures of transition regions have been studied using many techniques, both geological and geophysical. These techniques include reflection and refraction seismic surveys, gravity studies, and geologic mapping and interpretation. Many such studies have been completed so only a few examples will be cited here to support the choice of the model structure used. A review of studies of the continental margins of the eastern and western coasts of Canada by Keen and Hyndman (1979) shows sample sections of the transition regions along the passive margins of the eastern coast. The transition lengths observed vary between about fifty and two hundred kilometers with the average being about one hundred kilometers. Sheridan et al. (1979) and Grow et al. (1979) discuss refaction studies off the northeastern United States coast which show similar transition geometries and transition lengths of one to three hundred kilometers. Uchupi and Austin (1979) examine reflection profiles off the eastern coast of North America which indicate that the length of the upper surface of the transition region is about one hundred kilometers. Hinz et al. (1979) present the same types of

results off Labrador and Greenland showing transition lengths of about one hundred kilometers. Studies off northern Alaska by Eittreim and Grantz (1979) and Grantz et al. (1979) show transition lengths of the upper transition surface of between fifty and one hundred kilometers. Barton et al. (1984) derive a structure beneath the North Sea which shows similar transition regions. Le Douaran et al. (1984) examine the crustal structure in the northwestern Mediterranean Basin, and Makris et al. (1983) and Makris and Stobbe (1984) derive structures in the Eastern Mediterranean. In the Mediterranean region the transition regions are fifty to one hundred fifty kilometers in length. Most of the transition region structures mentioned above show similarities. In all cases the crustal layer thins from the continent toward the ocean. In most cases this thinning is fairly constant. The thicknesses of the continental and oceanic crustal layers vary somewhat. The resolution and detail in the models vary considerably. The details would need to be accounted for if cases of detailed waveform modeling were to be undertaken, but, they are not *critical for this study*. The lengths of transition regions suggested by the observations are between fifty and three hundred kilometers. These studies all indicate that the simplified models used in this investigation are reasonable. These models use a thirty two kilometer crustal layer over a half-space as a model of the continental structure and a five kilometer ocean over a five kilometer crust over a half-space as a model of the oceanic structure. The thickness of the crustal layer varies smoothly between the oceanic and continental values as one passes through a transition region. Model transition regions are constrained by computational limits to lengths of one hundred kilometers or less.

The wavefields transmitted through these models are synthesized to model the L_g arrivals in a seismogram. The L_g arrival was first defined by Press and Ewing (1952). Based on studies of seismograms recorded in North America, they defined L_g to have periods of 0.5 to 6 seconds, phase velocities between 2.0 and 3.5 km/s, reverse

dispersion at distances greater than 20°, and a sharp high amplitude onset. They noted that L_g arrivals are visible for purely continental paths and are gradually eliminated as the oceanic portion of the path increases in length beyond one hundred kilometers. The arrivals are visible on all three components but are larger on the horizontals. They suggested two possible interpretations of L_g, then abandoned the one which explained L_g in terms of higher mode Love waves in favor of one which explained them as channel waves trapped in the crust above a low velocity layer. The idea that L_g was a crustal channel wave was expanded and discussed by Press and Gutenburg (1956) and Gutenburg (1955) but even they stated that such an explanation was at best tentative. The interpretation of L_g in terms of higher mode Love waves was abandoned by Press and Ewing (1952) because of the motions on the vertical and longitudinal components and the long coda. Oliver and Ewing (1957, 1958a, 1958b) and Oliver et al. (1959) studied higher mode Love waves and Rayleigh waves and concluded that the vertical and longitudinal components of L_g are composed of higher mode Rayleigh waves and that higher mode Love waves could account for the transverse component. They considered only the first two higher modes and thus did not explain the long coda, but only its initial portion. Kovach and Anderson (1964) showed in detail that L_g could be interpreted using higher mode Rayleigh and Love waves. Panza et al. (1972) related the higher mode Rayleigh wave interpretation to the channel wave explanation. Panza and Calcagnile (1974, 1975) compare models with and without a low velocity channel below the crustal waveguide and conclude that such a channel is not necessary for the existence of L_g waves. Thus, the L_g arrival is clearly explained as a superposition of the higher mode Love waves and Rayleigh waves.

All the studies of higher mode Rayleigh waves and Love waves discussed above are based on analysis of group velocities, and phase velocities, with the L_g arrivals

corresponding to the group velocities of the extrema of the group velocity curves. Knopoff et al. (1975) used the higher mode interpretation of L_g to calculate synthetic seismograms for L_g. These seismograms further establish the validity of the previous interpretations based on group velocities of higher mode Love and Rayleigh waves by matching not only arrival times but also relative amplitudes. These seismograms also establish that the observed properties of L_g waves can be produced without including a low velocity channel. Knopoff et al. (1975) continued their studies using synthetic L_g waves to define properties of L_g that can be used to discriminate differences in crustal structure. Bouchon (1981,1982) used an alternate method for determining L_g synthetics at short distances (150 - 350 km) to model data from an earthquake in France. He concluded that the L_g arrivals were composed of multiply reflected post-critical SH and SV rays and that synthetics modeled the data well for group velocities between 3.5 and 2.8 km/s. Several other workers have used the fact that Love waves can be expressed as the superposition of post-critical multiply reflected SH rays in the crust to investigate the L_g arrivals. Herrin and Richmond (1960) along with corrections in Herrin (1961) used ray theory to show L_g could be modeled using multiply reflected and refracted ray in a thin crustal layer. This type of approach was also used by Pec (1967) and Kennett (1986) to address some properties of L_g. Cara and Minster (1981) developed a method to analyze Rayleigh type L_g seismograms recorded along a linear array. Cara et al. (1981) applied this method to data recorded in the northwestern Sierra Nevada and in southern California. They conclude that representation of L_g as a single multimode wavetrain is an oversimplified approach which can explain observations in the initial portions of the wavetrain (group velocity $>$ 3.2 km/s), while the later portions of the waveform are strongly affected by reflections and diffractions from any discontinuities in structure. Other phases previously defined in terms of the channel model have also been modeled using the higher mode surface wave model. Schwab

et al. (1974), Mantovani et al. (1977), Nakanishi et al. (1977), and Mantovani (1978) considered S_n, Stephens and Isacks (1977) considered the transverse component of S_n, and Cansi and Bethoux (1985) investigate the T phase which converted to L_g at the continental margin. In light of all the evidence the higher mode interpretation of L_g best explains the observed properties of L_g, even though variations in the crustal structure may cause a longer coda than that calculated using a simple layered structure. The SH L_g seismograms used to produce the wavefields used to drive the FE calculations in this study are determined as mode sums over the fundamental and first five higher modes.

One of the important uses of L_g has been to distinguish regions with oceanic crustal structures from those with continental crustal structures and to map regions where sudden changes in crustal structure occur. While the theoretical interpretation of L_g were being debated many observational studies of L_g waves were being conducted. These studies were conducted to map regions of oceanic crustal structure and regions of complex crustal structure on continents which caused the L_g arrival to be heavily attenuated or vanish. The studies considered a strong L_g to indicate continental structure and a missing or highly attenuated L_g to indicate passage through oceanic crust. Intermediate cases were included in one group or the other depending on the workers, but none used a quantitative scale.

Bath (1954,1958) collected a large sample of L_g data along Euroasiatic paths and fashioned explanations of his data based on the guided wave interpretation of L_g. He also defined two arrivals he called L_{g_1} and L_{g_2} with distinctly different phase velocities of 3.54 km/s and 3.37 km/s. His observations supported the conclusion of Press and Ewing (1952) that partially oceanic paths resulted in attenuation of the L_g phase. However, he interpreted some portions of the Arctic Ocean where L_g was not attenuated as being continental in structure. This approach, of defining paths which

pass under oceans but do not attenuate L_g as continental paths has also been used in most of the more recent studies of this type since that time. These studies used L_g recorded in many regions of the world. Press et al. (1956) considered paths in Africa, Press (1956) used paths in California, Savarensky and Valdner (1960) studied the Black Sea region, Bolt (1957) studied data from Australia, Utsu (..) considered Japan and the region surrounding it, and Lehmann (1952, 1957) studied significant events in North America and Europe. Oliver et al. (1955) considered L_g propagation in the Arctic region, Herrin and Minton (1960) in the Southwestern United States and Mexico, and Wetmiller (1974) investigated the crustal structure in the Baffin Bay area. Gregersen (1984) studied the crustal structure near Denmark and in the North Sea. Additional data for this area were presented by Kennett and Mykkeltveit (1984) who used the supplemented data set and the method of Kennett (1984a) to produce synthetics and an interpretation of the data in terms of a multimode wavetrain traveling through a crustal 'pinch'.

As originally noted by Bath, some purely continental paths show attenuated L_g and the later studies mapped these regions. Gumper and Pomeroy (1970) made a more extensive study of L_g and other phases in Africa. They found L_g velocities between 3.48 and 3.60 km/s and a discontinuity in the crust near the rift zone. Ruzaikin et al. (1977) mapped regions of L_g propagation in Asia and saw attenuation in Tibet and regions of China. Kadinsky-Cade et al. (1981) conducted a detailed study of L_g, S_n, P_g, and P_n propagation in India, the Himalayan Arc and the Tibetan Plateau producing a more detailed map than Ruzaikin et al., and agreeing with their observations and the sparse observations of Bath that showed the absence of L_g on paths crossing or originating in Tibet. Finally, Ni and Barazangi (1983) report the results of a detailed study in India, Tibet, and the Himalayan Arc which agrees with other results. Chinn et al. (1980) studied L_g and S_n in western South America and

observed that L_g propagation was efficient only parallel to the strike of the Andes. They also observed conversion of Oceanic S_n to L_g in areas of crustal thickening. Isacks and Stephens (1975) also observed conversion of S_n to L_g both in earthquakes from the West Indies observed in Eastern North America and in earthquakes near southernmost Mexico observed on the northern coast of the Gulf of Mexico. Some of their claims of observed conversions are disputed by Shurbet (1962, 1974, 1976). Gregersen (1978) discusses conversion between different modes of Love waves and between Love and Rayleigh waves at an ocean continent boundary. These studies illustrate the importance of a clear understanding of the mechanisms of attenuation of L_g along mixed paths. Simply stating that a path which passes under an ocean but is not attenuated implies that the floor of that ocean has a continental structure could be misleading. A clearer understanding of the effects of structural transitions on the attenuation of L_g is important.

Another major use of L_g waves is the determination of magnitudes of explosions and earthquakes and of regional attenuation properties. These magnitudes, usually referred to as m_{bL_g}, and other types of magnitudes are compared to discriminate between the two types of sources (Blandford, 1982, and Pomeroy et al. 1982). The ratio of body wave magnitude, m_b, to surface wave magnitude, M_S, is one such discriminant whose physical basis is explained by Stephens and Day (1985). In order to examine whether this type of discriminant can be generalized to periods shorter than than those considered when using the twenty second surface wave magnitude, new empirical relations for short period phases such as L_g (Baker, 1970) and R_g (Basham, 1971) were derived to measure short period surface wave magnitudes. Nuttli (1973) used observed attenuation of short period Rayleigh waves (L_g, and R_g) to present a theoretical explanation and generalization of the empirical relations and defined their limitations. He explained how to use data of L_g amplitude versus

distance to determine the value of γ, the coefficient of anelastic attenuation. Nuttli (1978) extended the definitions from one second waves to frequencies as high as ten Hertz. These studies provided a more quantitative method for mapping the attenuation of L_g than simply recording whether L_g was observed, not observed, or attenuated. Thus, a series of studies mapping the attenuation of L_g using the determination of γ were initiated. An extensive study of the United States at 0.5 to 2 Hz. had previously been completed by Sutton et al. (1967) using other methods. Nuttli (1973) developed an L_g magnitude scale for the central United States. Herrmann and Nuttli (1982) studied the relation of this scale, m_{bL_g}, to the local magnitude scale, M_L. The attenuation observed was used to model ground motions at regional distances due to earthquakes and assess the possible destructiveness of the L_g part of the wavetrain (Herrmann and Nuttli, 1975a, 1975b). An additional study of this type of problem using added data was done by Street (1984). Street et al. (1975) studied L_g spectra of United States earthquakes. The results were the basis of a study of L_g moments, magnitudes, and intensities (Street and Turcotte, 1977) and the development of an L_g magnitude scale analogous to that of Nuttli (1973) for the northeastern United States and southeastern Canada (Street, 1976). Jones et al. (1977) studied attenuation of L_g in the southeastern United States. Nuttli (1980) considered a region including Iran. Bollinger (1979) again studied the northeastern United States obtaining results consistent with Street (1976). Nuttli (1981) examined attenuation of L_g in western and central Asia for both earthquakes and explosions. Barker et al. (1981) studied the crustal structure at the Nevada Test Site using L_g and P_g. Chung and Bernreuter (1981) reviewed the studies of regional relations between various magnitude scales including m_{bL_g}. Nicolas et al. (1982) studied attenuation of regional phases in western Europe. Gupta et al. (1980) considered both earthquakes and explosions in western Russia, and Gupta et al. (1982) studied variations in horizontal to vertical L_g

amplitude ratios. Ebel (1982) criticizes the m_{bL_g} scale as being inappropriate at five to ten Hertz for earthquakes in the northeastern United States. Dwyer et al. (1983) presented a frequency dependent study of L_g in the central United States which addresses this criticism of the m_{bL_g} scale. Singh and Herrmann (1983) present a regionalized map of L_g attenuation in the continental United States for periods between 0.5 and 3.5 Hz. Herrmann and Kijko (1983a, 1983b) also investigate necessary changes to the L_g magnitude scale to allow use of data for instruments with predominant periods other than the one second period of the WWSSN instrument. Campillo et al. (1984) studied the excitation of spectra and geometrical attenuation of regional phases including L_g. Der et al. (1984) studied the coherence of the L_g wave crossing a given region. All these studies are based on the interpretation of L_g as a superposition of higher mode Love and Rayleigh waves. They all assume that the L_g waves are traveling through a relatively constant thickness crustal layer, and most do not account for reflection of diffraction of L_g energy from changes in thickness of the crust. Clearly, it is important to understand if such changes will produce significant effects not accounted for in the interpretations given.

Many attempts to understand the propagation of seismic disturbances across regions of varying structure such as transition zones have been made. First, simple models were used and analytic solutions were derived for soluble special cases, then increasingly complicated models were considered as available computational power increased. The types of models that have been used to approximate transition regions can be separated into several types which are illustrated in Figure 1.

The simplest type of model (Figure 1a) consists of two homogeneous layered regions, 1 1', and 3 3', with layer over half-space structures separated by a vertical boundary or a region 2 2' in which density, ρ, rigidity μ, and SH wave velocity , β, vary smoothly between their values in the regions 1 1' and 3 3'. Sato (1961a) discusses

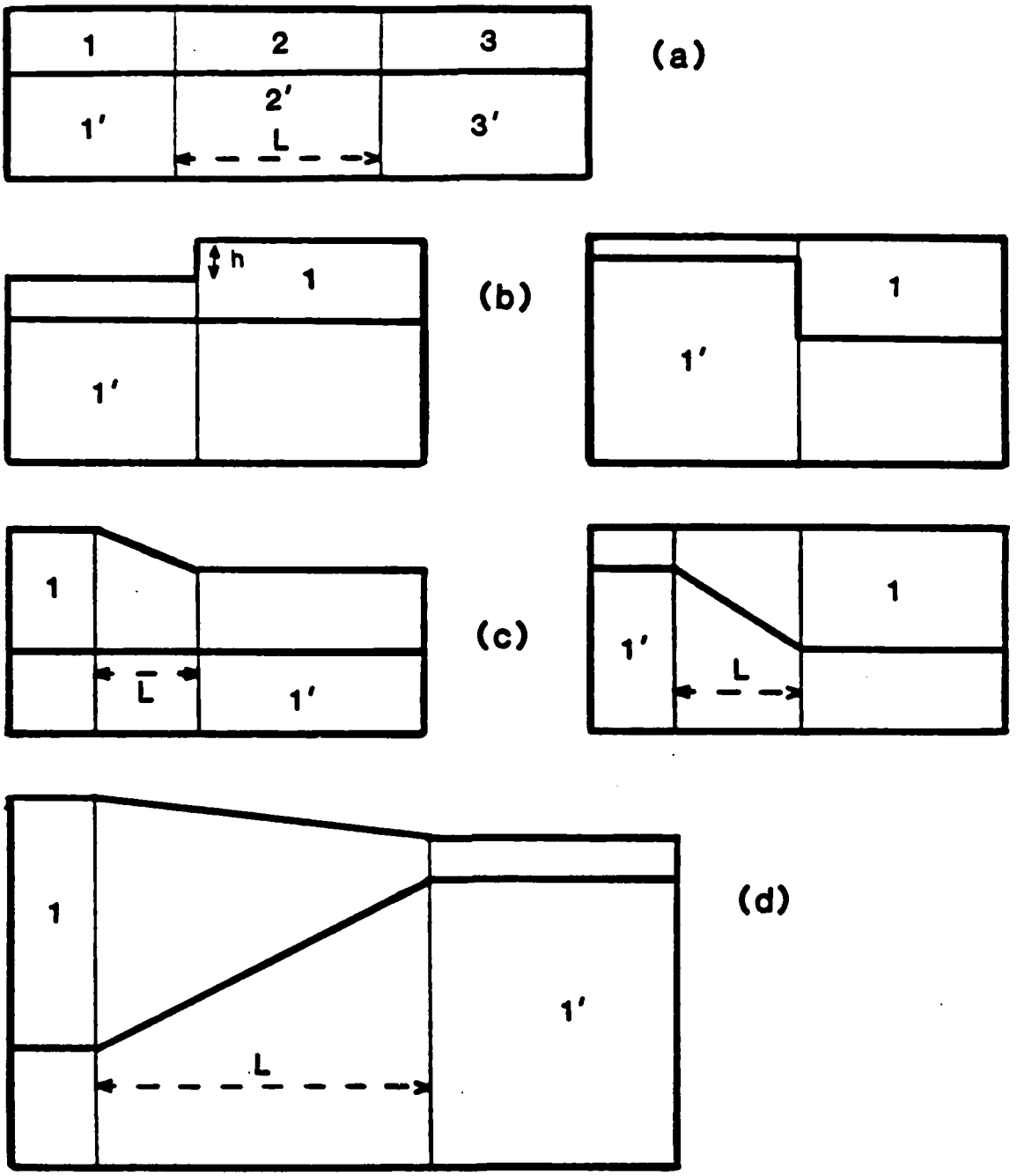

Figure 1: Types of models used in studies of propagation of Love waves across continent ocean boundaries. Part a) shows the simplest model, two regions labeled 1 and 3 separated by a vertical boundary or a intermediate region, 2, of varying properties. Part b) shows another type of simple model, a layer of a half-space with a sudden step change in the thickness of the layer. Part c) shows a more general type of simplified model with a more gradual change in thickness rather than a step. Part d) shows the type of model used in this study, which includes smooth thickness variation both at the surface and the base of the crustal layer.

both these cases applying the conditions

$$\frac{\mu_3}{\mu_1} = \frac{\mu_{3'}}{\mu_{1'}} \qquad \beta_1^{-2} - \beta_{1'}^{-2} = \beta_2^{-2} - \beta_{2'}^{-2}$$

to assure the transmission of fundamental mode Love waves across the boundary without modal conversion. He derives analytic expressions for the transmitted and reflected waves, the phase and group velocities, and the reflection and transmission coefficients in each case. The case for which no transition regions is present has since been used by Alsop (1966), Boore (1970), and Gregersen and Alsop (1974, 1976) as a test case for more generalizable numerical methods. More recently, Kennett (1973) has developed a numerical technique to consider the problem of seismic waves interacting with a layer or layers in which properties change across a surface perpendicular to or at a specified angle from the layering.

The next level of complexity that can be introduced into the model is the inclusion of a change in the thickness of the surface layer at the discontinuity between the two structures. This type of model is illustrated in Figure 1b. In most cases the material properties do not change when the layer thickness changes. Sato (1961b) used the Wiener-Hopft technique to obtain analytic expressions for the transmitted and reflected waves for a model with a surface step with height h much less than the wavelength of the incident wavefield λ. Using these solutions he obtained approximate expressions for energy reflection and transmission coefficients for a surface step model using a Green's function method. Hudson and Knopoff (1964) calculated expression for the motion and the reflection and transmission coefficients for the surface step model. They did not need or use the $h << \lambda$ approximation. Alsop (1966) developed an approximate method for determining Love wave transmission and reflection coefficients in a model of type 1b. This method assumes that all energy remains in Love waves, introducing errors, particularly at intermediate periods, if any

energy is converted between modes or into forms other than modal energy. The latter two methods had the advantage that higher modes could be used and that no specific interrelation of elastic properties between the different layers or regions was necessary. Gregersen and Alsop (1974, 1976) extended the method of Alsop (1966,1968) to the determination of transmission coefficients for the case of non-normally incident Love waves. At normal incidence results correspond well to those found in previous studies, for oblique incidence at angles less than forty degrees normal incidence is a good approximation. Bose (1975) solves the surface step problem using an integral equation formulation which yields asymptotic solutions for large distances from the step. His results show increases in amplitude for a step down and decrease in amplitude for a step up, consistent with results derived for the step models in this study. Kazi (1978a, 1978b) uses the variational method of Schwinger-Levine to derive solutions to the surface step problem that account for the Love waves converted to body waves at the surface step. He determines the reflection and transmission coefficients by way of a scattering matrix and evaluates them for the same cases as Alsop (1966) and Knopoff and Hudson (1964) showing that the transmission coefficients increased after the cutoff frequency rather than decreasing as was observed in earler studies that neglected the body waves. Lapwood, Hudson, and Kembhavi (1973, 1975) and Lapwood and Hudson (1975) used a similar variational technique to study normally and obliquely incident plane waves incident on a layer between two uniform half-spaces. Hudson (1977) extended their method to the surface step problem but concluded that the numerical implementation of the method would not be more efficient than existing techniques. Martel (1980) used a finite element technique to evaluate propagation of Love waves across a Moho step. Spatial filtering of the transmitted and reflected modes to determine transmission and reflection coefficients allowed the isolation of the diffracted body wave component.

Studies using the surface step model and the Moho step model have been generalized in several ways. First, and most relevant to this study, the step can be replaced by a transition region as discussed in the next paragraph. Other types of generalization allow the study of the effect of topography, of a short section if thinner crust referred to as a crustal 'pinch', or of continuous but small variations in crustal thickness on the incident wavefield. Gilbert and Knopoff (1960) used a method similar to a Born approximation to study seismic scattering from topography and to produce approximations valid for pulses with duration short with respect to the horizontal travel time across the irregularity. Hudson (1967) extended the method of Gilbert and Knopoff (1960) to variations in elastic properties at the surface such as sediment filled depressions, as well as surface distortions. The method can be used to obtain a rough estimate of the dimension of the scatterer. Boore et al. (1971) and Boore (1972) study the effect of topography on SH waves using the Finite Difference method to propagate a simple pulse through the structure. This approach, unlike the previously discussed methods, allows the consideration of steep topography or topography with wavelength similar to or smaller than that of the incident waves. Herrera (1964a, 1964b) developed a perturbation method to study the effects on a propagating seismic disturbance of a crustal layer with slowly varying thickness. Mal and Herrera (1965) studied the effect of a short section of thinner crust, where the difference in crustal thickness between the thin and the thick crust is small compared with the wavelength of the incident energy.

The next increase in the complexity of the transition model is the introduction of a transition region in which the crustal thickness varies smoothly between the crustal thicknesses at its ends. The simplest models of this type are shown in figure 1c. In these models either the surface or the Moho have a smooth slope in the transition region. Knopoff and Mal (1967), and Knopoff et al. (1970) explained an analytic

solution for this type of model when the slope of the surface (or Moho) of the transition region is small. They also assumed that the local phase velocity was the same as that in a layered structure with the local layer thickness. They found forward scattering to be much less important than back scattering. Pec (1967) calculated the dispersion of Love waves propagating in a wedge shaped layer such as the transition region in models of type 1c. He considered Love waves in terms of the constructive interference of multiply reflected SH rays and found that the inclination of the Moho caused the largest changes in phase velocity and amplitudes at short periods. Boore(1970) studied the propagation of a simple low frequency Love wave across the type of structure shown in figure 1c. He specified the displacements at t=0 and t=dt throughout the grid such that the displacement at t=0 at the surface of the layer over a half-space portion of the model was a Ricker wavelet. The Finite Difference method was then used to calculate phase velocities and transmission coefficients at various points along the grid surface for a one hundred twenty kilometer long transition region. Periods of twenty to one hundred thirty seconds were used. Phase velocities were lower for propagation from continent to ocean than from ocean to continent. He noted that in the region of the transition that mode conversions and conversion to other types of waves seemed to be important. Lysmer and Drake (1971, 1972) and Drake(1972), who discusses mainly Rayleigh wave results but states that they also apply to Love waves, use a Finite Element method based on Zienkiewicz and Cheung (1967) which includes a rigid grid bottom and thus allows no energy to escape the grid. The formulation also requires that the incident modal energy is exactly equal to the sum of the reflected and transmitted modal energy, thus disallowing conversion to other types of waves. Lysmer and Drake (1971) use this method to study the effect of a transition of type 1c, with length one hundred twenty kilometers, or 1d, with a length of one hundred kilometers, on the incident fundamental mode Love wave

energy. With their constraint no difference in continent to ocean and ocean to continent phase velocities is seen, so they attribute the differences to body wave interference. They estimate that about one percent of the energy at 25s period is transmitted without mode conversion and about 35% is transmitted in other modes. Drake(1971) discusses mainly Rayleigh wave results but states that they also apply to Love waves. Drake and Bolt (1980) used the method of Lysmer and Drake (1972) to study a more complicated model with the upper and lower transition surfaces having different lengths to model phase velocity data of events normally incident on the California continental margin. They considered periods between 4.4 and 60 seconds and modeled only incident fundamental mode waves. They discuss the period ranges over which fundamental mode transmission is small and conversion to particular higher modes is large. They conclude that the ocean continent boundary strongly increases the attenuation of fundamental mode Love waves. Schlue (1979) shows some simple examples of a three dimensional Finite Element solution for Love wave propagation.

All the studies discussed in the previous paragraph used periods much longer than those that will be considered in the following discussions. The shorter periods used in this study allow the examination of the effects of transition regions with length many times the wavelength of the incident energy. Most previous studies considered transition regions with lengths comparable the wavelength of the incident energy. The method of Lysmer and Drake (1972) purposely excluded the possibility of conversion from modal energy to body waves, and thus excludes the possible escape of energy from the system as these body waves travel out the bottom of the grid. This escaping energy is shown in this study to be an important component of the explanation of the attenuation of the L_g phase traveling on partially oceanic paths. The studies using the method of Lysmer and Drake (1972) used periods shorter than other studies but longer than those used here. They also considered only fundamental mode Love wave input

and calculated each mode separately, while the driving functions used in this study are a sum over a range of frequencies on the fundamental and first five higher branches. In fact most of the earlier studies with Finite Element or Finite Difference considered the fundamental mode at one frequency rather than over a range of frequencies. None of these studies has generated realistic seismograms, but instead they all concentrated on measuring phase velocities and transmission and reflection coefficients. In light of these facts it is clear that the results discussed in this thesis can give a significant addition to the understanding of the propagation of L_g waves across transition regions.

Finally, the content of each chapter will be summarized. The first four sections of chapter one present the basics of and the notation associated with the Propagator Matrix and FE techniques. Sections five and six discuss the theory of the two coupling methods. The remainder of the chapter is a series of tests of the accuracy of the coupling technique discussed in section five and used in chapter two. Sections one to three of chapter two discuss the design of the numerical experiments presented in the remainder of that chapter, and in section two of chapter three. The remainder of chapter two discussed the effects of transition of L_g wavetrains and the dependence of those effects on transition length. Chapter three first presents FE results investigating the effect of the length of the oceanic path on the L_g wavefield. Then examples of the accuracy and efficiency of the coupling method discussed in section six of chapter one are presented. Finally, this method is used to determine seismograms after propagation through a transition and then oceanic paths of different lengths. Reasons for the attenuation of L_g for oceanic path lengths longer than 100-200 kilometers are discussed.

Chapter 1

Representation Theorem Coupling of the Finite Element and Modal Propagator Matrix Methods

Intoduction

In this chapter the methods for Representation Theorem (RT) coupling of finite element (FE) or finite difference calculations and Harkrider's (Harkrider 1964, 1970) propagator matrix method calculations to produce a hybrid method for propagation of SH mode sum seismograms across paths that contain regions of non plane-layered structures are explained and developed. The FE method used in this study is an extensively modified version of the Stress Waves in Solids code (Frazier, Alexander and Petersen, 1973). The coupling methods explained in detail in this chapter use a 2-D Cartesian FE formulation. Analogous methods for the 3-D method follow directly. The hybrid method linking propagator matrix results to FE calculations assumes that the wavefield arrives at the edge of the FE grid after propagating many wavelengths in the layered structure. Extensive tests illustrating the validity and accuracy of the implementation of this method are presented in this chapter. These tests use a structure consisting of a layer over a half-space. This simple structure allows the calculation of synthetic seismograms using only the propagator matrix technique. These synthetic seismograms can be directly compared to the hybrid results to ascertain the accuracy and the limitations of the coupling technique. After propagation through a path of length much less than the source to FE grid distance in the FE grid the wavefields can be coupled back into a layered medium. The layering in the second layered medium need not be identical to that in the first layered medium. The tests of coupling from FE to propagator matrix are discussed in chapter 3. This sequence of

procedures can be repeated any number of times, thus including several regions of complexity in the source to receiver path.

These hybrid techniques are developed to study the propagation of surface waves across regional transition zones or other heterogeneities that exist in part of a longer, mostly plane-layered, path. Examples of structures of interest through which surface waves can be propagated using these techniques include, regions of crustal thickening or thinning such as continent ocean transitions or basins, anomalous bodies of any shape located in the path, topography, and sudden transitions from one structure to another. In fact, any arbitrary structure of interest can be placed in the FE portion of the path.

To clearly explain the methods used to couple finite element (FE) and propagator matrix methods, enabling transmission of a disturbance along part of its path from the source to the receiver by each method, it is useful to first discuss some of the foundations on which each method is based, and some of the details of the implementation of each method. The propagator matrix technique is used to transmit mode sum synthetics through sections of their paths that consist of simple plane layered structures. The theory used to derive this technique is explained in detail by Harkrider (Harkrider 1964). His numerical implementation of these ideas forms the basis for the slightly modified codes used in this study. The fundamentals of this method which are central to the understanding of the Representation Theorem coupling techniques and the generation of the mode sum synthetics and the Green's Function synthetics used in these techniques will be discussed below. The modifications to the numerical implementation of Harkrider will also be discussed. The FE calculations discussed here are done using an extensively modified version of the Stress Waves in Solids (SWIS) code developed by Frazier, Alexander, and Petersen (Frazier et al. 1973, Frazier and Petersen 1974). The basic structure of SWIS code is retained, but many options in the code

are removed, and the detailed implementation is changed in order to produce a large increase in the speed of execution. Further options not available in the version of the SWIS code used were added to enable grid points to be constrained to move with a given time history, to allow the production of time slices, and to implement hourglass corrections for the SH case. Details of these changes and their impact will be discussed later, as will the basic formulation of the SWIS FE method.

The Propagator Matrix Technique

The basic idea behind the propagator matrix method as implemented by Harkrider is to transmit the disturbance produced by a source within a layered half-space structure through that structure by combining terms that describe the source, the medium response, and the propagation effects. The terms that apply the effects for the propagation path in the z direction are in the form of propagator matrices. For source and receiver both at depth, they are separated into two parts, the propagation in z from the source to the surface, and the propagation in z from the surface to the receiver. An additional propagation term adds the effect of the propagation in the r coordinate. In most cases the general form of a modal displacement at a receiver at depth is

$$v(r,\phi,z) = S\, A_L \left[\frac{v_S(h)}{v_0}\right]_H \left[\frac{v_R(z)}{v_0}\right]_H P \qquad (1)$$

where S is a function of the source strength and geometry, A_L represents the medium response for a surface source and a surface receiver, P expresses the propagation effects in direction r, $\left[\frac{v_S(h)}{v_0}\right]_H$ is the term for transmitting the disturbance from the source depth to the surface which because of reciprocity can be expressed as a modal propagator from the surface to the source depth, and $\left[\frac{v_R(z)}{v_0}\right]_H$ is the propagator from the surface to the receiver depth. The subscript H on the terms which transmit the modal

disturbances in z denotes homogeneous, that is independent of and not containing a source. The expressions within the square brackets of these terms represent matrix quantities, not simple ratios. If the source is a stress source rather than a displacement source then $\left[\frac{v_S(h)}{v_0}\right]_H$ is replaced by $\frac{k_L}{\mu_S}\left[\frac{\tau^*(h)}{\dot{v}_0 / c_L}\right]_H$, where μ_S is the rigidity at the depth of the source. If stress rather than displacement is to be recorded at the receiver, then $\left[\frac{v_R(z)}{v_0}\right]_H$ is replaced by $\frac{k_L}{\mu_R}\left[\frac{\tau^*(z)}{\dot{v}_0 / c_L}\right]_H$. In this expression μ_R is the rigidity at the depth of the receiver. As an example of a specific case of this type of representation, the displacement expressions for a double couple source of arbitrary orientation will be stated in terms of the propagator formulation. This expression will then be used to obtain the expressions for displacements from a dip slip and a strike slip source. These expressions will be used extensively in subsequent discussions. Following this discussion the modifications made to the propagator matrix codes will be explained.

The displacement for an arbitrary double couple source follows directly from the expression for the SH displacement at the free surface produced by a double couple source of arbitrary orientation at depth h (Harkrider 1964, 1970).

$$\left\{\overline{v}_0\right\} = 2i\pi K_{\#} k_\beta^2 \mu \Delta_L \left\{ \left[\cos\lambda \sin\delta \cos2\phi - \sin\lambda \frac{\sin2\delta}{2} \sin2\phi\right] \left[\frac{v_S(h)}{v_0}\right]_H \frac{\partial H_2^{(2)}(k_L r)}{\partial r} \right.$$

$$\left. - \left[\sin\lambda \cos2\delta \cos\phi + \cos\lambda \cos\delta \sin\phi\right] \left(\frac{1}{\mu_S}\left[\frac{\tau^*(h)}{\dot{v}_0 / c_L}\right]_H\right) \frac{\partial H_1^{(2)}(k_L r)}{\partial r} \right. \qquad (2)$$

where

$$K_{\#} = \frac{-\overline{M}(w)}{4\pi\rho\omega^2} = \frac{iM_0}{4\pi\rho\omega^3} \qquad \dot{v}_0 = i\omega v_0 \qquad (3)$$

$$k_\beta^2 = \frac{\omega^2}{\beta^2} = \frac{\rho_s \omega^2}{\mu_s} \qquad k_L = \frac{\omega}{c_L} \qquad \tau = i\tau^* \qquad (4)$$

In equations (2), (3), and (4), λ is the strike of the double couple source, δ is the dip, ϕ is the azimuth to the station, β is the SH wave velocity, ρ_s is the density at the depth of the source, h is the source depth, ω is the frequency, r is the distance from the source to the receiver, c_L is the Love wave velocity, μ_S and μ_R are respectively the rigidity at the source depth and at the receiver depth, A_L is the medium response for a surface source and receiver, $\left[\frac{v_S(h)}{v_0}\right]_H$ and $\left[\frac{\tau^*(h)}{\dot{v}_0 / c_L}\right]_H$ are the terms that transmit the source disruption in z from the source to the surface receiver, and the term containing the Hankel function is the propagation term in r. The source term is defined to contain all the angular dependence on δ, λ, and ϕ, as well as the term $2i\pi k_\beta^2 K_\psi$, and the factors of μ. The second equality in the first expression of equation (3) assumes a step moment, that is $\overline{M}(\omega) = \frac{M_0}{i\omega}$.

It is well known that a double couple of arbitrary orientation can be expressed in terms of a linear combination of double couple sources of three types, vertical strike slip, vertical dip slip and 45° dip slip. Thus, results for these three fault types can be added to produce results for an arbitrary orientation, removing the necessity to repeat the entire procedure for each orientation to be studied. Substituting (3) and (4) into (2) and evaluating the expression for each of the three basic fault types yields, (5), the expressions used to determine displacement at the surface. For a vertical strike slip fault $\delta = 90°$, and $\lambda = 0°$. In the following development part a of each set of equations will be the expression for the strike slip fault. For a vertical dip slip fault $\delta = 90°$, and $\lambda = 90°$. Part b of each set of equations below will be the appropriate expression for the vertical dip slip fault. For a 45° dip slip fault $\delta = 45°$, and $\lambda = 90°$. Part c of the next group of equations is for a 45° dip slip fault.

$$\left\{\bar{v}_0\right\} = -\frac{M_0}{2\omega}\,\Delta_L \cos 2\phi \left[\frac{v_S(h)}{v_0}\right]_H \frac{\partial H_2^{(2)}(k_L r)}{\partial r} \tag{5a}$$

$$\left\{\bar{v}_0\right\} = -\frac{M_0}{2\omega}\,\Delta_L \sin\phi \frac{1}{\mu_S}\left[\frac{\tau^*(h)}{\dot{v}_0 / c_L}\right]_H \frac{\partial H_1^{(2)}(k_L r)}{\partial r} \tag{5b}$$

$$\left\{\bar{v}_0\right\} = -\frac{M_0}{2\omega}\,\Delta_L \frac{(-\sin 2\phi)}{2}\left[\frac{v_S(h)}{v_0}\right]_H \frac{\partial H_2^{(2)}(k_L r)}{\partial r} \tag{5c}$$

Examining equations (5) shows that, for SH waves, any fault geometry can be modeled using a linear combination of only the vertical dip slip and the vertical strike slip faults. This follows from the observation that the vertical dip slip and the 45° dip slip expressions differ only by a function of the azimuth ϕ. For the remainder of this development only vertical dip slip and vertical strike slip fault types will be considered. This is equivalent to setting $\sin\phi = \cos 2\phi = 1$, and $\sin 2\phi = 0$, that is $\phi = 90°$. For a given value of ϕ any fault geometry can be reconstructed by reintroducing the appropriate values of $\sin\phi$, $\cos 2\phi$, and $\sin 2\phi$ into the coefficients of the linear combination of the remaining two factors. The displacements determined by equation (5) are those produced at the surface by a double couple source at depth h. To determine the displacements at depth, a term propagating the energy from the surface to the depth of the receiver must be included. For a receiver at depth z the modal displacement expressions become

$$\left\{\bar{v}(z)\right\} = -\frac{M_0}{2\omega}\,\Delta_L \frac{\partial H_2^{(2)}(k_L r)}{\partial r}\left[\frac{v_S(h)}{v_0}\right]_H \left[\frac{v_R(z)}{v_0}\right]_H \tag{6a}$$

$$\left\{\bar{v}(z)\right\} = -\frac{M_0}{2\omega}\,\Delta_L \frac{1}{\mu_S}\frac{\partial H_1^{(2)}(k_L r)}{\partial r}\left[\frac{\tau^*(h)}{\dot{v}_0 / c_L}\right]_H \left[\frac{v_R(z)}{v_0}\right]_H \tag{6b}$$

Most of the changes made to the propagator matrix codes of Harkrider were minor. The only major changes were the addition of an option to evaluate the

analytic expressions for the stresses and the implementation of an alternate code which uses the line source rather than the point force, double couple, or explosive sources already available. The implementation of the stress calculation will be discussed later. The construction of the line source code required changes to the source terms and the modal propagation terms that propagate in r. The basic form of the z dependent modal propagator terms is identical regardless of the source used, so no changes were necessary in the calculation of $\left[\frac{v_S(h)}{v_0}\right]_H$, $\left[\frac{v_R(z)}{v_0}\right]_H$, $\left[\frac{\tau^*(h)}{v_0 / c_L}\right]_H$, or $\left[\frac{\tau^*(z)}{v_0 / c_L}\right]_H$. The line source code is set up to calculate displacement, stress, and displacement and stress Green's functions. The minor changes made to the codes include the restructuring of the order of operations to allow the efficient calculation of particular types of sets of seismograms. To efficiently calculate sets of displacement and stress seismograms in which successive seismograms are at the same horizontal distance r, and at a series of receiver depths at intervals of Δz, the operations were reordered to avoid unnecessary recalculation of intermediate results. The propagation terms in r need to be calculated only once, as does the source to surface term. To efficiently calculate sets of displacement and stress line source Green's functions the calculations were reordered in a different manner so that the surface to receiver propagator term and the propagation term in r needed to be evaluated only once. The codes still retain the ability to calculate seismograms for sets of receivers or Green's functions for sets of sources which do not form depth sections. However, for these sets the order of operations is not necessarily optimal and extra time may be taken in calculation of displacements or stresses.

The Modified SWIS Finite Element Code

The SWIS FE program is a flexible code capable of calculating the propagation of stress waves through solids of arbitrary complexity. Properties such as density, and elastic wave velocity are defined at a grid of nodes whose locations can be defined in

curvilinear coordinates. These properties are then used to determine the location, stress, and motion of the nodes in the grid as a function of time. Next, it is useful to give a simple step by step outline of the procedures used in the SWIS FE code.

First, several quantities are defined at each node or at each element in the grid to provide the initial conditions. In particular, the properties that are initialized at each node before the first time step are, the nodal position $\underline{X}(t)$, nodal displacement $\underline{U}(t)$, and nodal velocity $\dot{U}\left(t - \frac{\Delta t}{2}\right)$. The properties defined for each element are the force as a function of time, $\underline{F}(t)$, resulting from body forces $\underline{f}(t)$ within the element and from tractions $\underline{\pi}(t)$ applied to the surface of the element, and the elastic constants as determined by specification of density and elastic wave velocities. The values, within a element, of the variables initialized on each node are defined by interpolation between the nodal values at the nodes surrounding that element. In order to define the form of the interpolation functions the coordinate systems which define the location of a point within an element and the location of an element within the body must be defined and related. The 'natural' or local coordinate system defines the location of any point in the element with respect to the nodes surrounding that element. Each node is defined to be a unit distance, in each coordinate, from the element center. Let z_i be the coordinates of a point in element e in this 'natural' coordinate system, and let Z_i^m be the coordinates of node m, one of the nodes bordering element e, in the 'natural' coordinate system. This means that Z_i^m is always ± 1. A Cartesian coordinate system is defined within the volume V containing the body composed of the elements. In this Cartesian coordinate system, the i^{th} component of the position of node m bordering element e will be denoted X_i^m, and the i^{th} coordinate of a point z within element e will be denoted x_i. The Cartesian coordinates x_i and X_i^m can be transformed to an arbitrary curvilinear coordinate system y_i and Y_i^m using the well known relations for the transformation of quantities between Cartesian and general curvilinear coordinates.

Since all calculations in this study are performed in Cartesian coordinates, the transformation to general curvilinear coordinates will be omitted in further discussion of the SWIS FE method. Now it is possible to define the interpolation function used to determine positions, dislocations, velocities, accelerations and stresses within an element. In 'natural' coordinates the interpolation function used to define the coordinates of a point z within element e has the form

$$P^m(z) = \frac{1}{2^D}\prod_{i=1}^{D}(1 + z_i Z_i^m) \tag{7}$$

where

$P^m(z)$ the interpolation function at point z for position of node m bordering element e

D number of space dimensions

Using the interpolation function it is possible to define the value of any of the quantities initially defined at each node at any point within an element, in terms of the Cartesian coordinates of the nodes surrounding the element. The location of the evaluation point within the element is expressed in the 'natural' coordinate system, For the position, displacement, applied force, or velocity at any point in an element surrounded by 2^D nodes the relation is or is analogous to equation (9).

$$x_i = \sum_{m=1}^{2^D} P^m(z) X_i^m \tag{8}$$

For the stresses the relation is

$$\sigma_{ij} = \sum_{m=1}^{2^D} \frac{\partial P^m(z)}{\partial z_j} X_i^m \tag{9}$$

The SWIS code is based upon a one point quadrature integration rule, so the point z used to evaluate these expressions is the centroid of the element. Given the initial values the SWIS code uses one of several series of calculations to advance the properties of the nodes of the grid one time step, Δt. Only the option used for the

calculations in this study is discussed below. To update the values of the initialized quantities by Δt, thus yielding the configuration of the grid at time $t+\Delta t$ the following time centered explicit FE integration procedure is used;

(1) Compute strain and thus stress at the centroid of each element m

$$\sigma_{ij}(\underline{x},t) = 2\mu\left\{\frac{1}{2}\frac{\partial P^m(z)}{\partial z_j}U_i(t) + \frac{1}{2}\frac{\partial P^m(z)}{\partial z_j}U_j(t)\right\} + \lambda\delta_{ij}\frac{\partial P^m(z)}{\partial z_k}U_k(t) \qquad (10)$$

(2) Compute the restoring forces for each element m

$$R_i^m(t) = \sigma_{ij}(\underline{x},t)\frac{\partial P^m(z)}{\partial z_i} \qquad (11)$$

Then use the values of restoring force R_i^m at each element m surrounding a given node to determine a net restoring force R_i at each node.

(3) Integrate the equation of motion to give the values of location, stress and motion at each node at time $t + \Delta t$.

$$U_i(t + \Delta t) = U_i(t) + \Delta t\left\{\dot{U}\left[t - \frac{\Delta t}{2}\right] + \Delta t\frac{\left(F_i(t) + R_i(t)\right)}{M}\right\} \qquad (12)$$

The basic series of calculations described above form the core of the SWIS code and were retained in principle in the modified and accelerated version of SWIS used in this study.

In the discussion of the basics of the FE method used no mention was made of the exact method by which a source can be introduced into the FE calculations. In the basic version of SWIS a point source or a source of finite spatial dimension can be defined by constraining a node or nodes in the grid to have a specified displacement at time zero. Alternately, given body forces, F_i, can be applied at the centroids of one or more elements at time zero to create a source. Clearly, a more general source would

be desirable, and in fact necessary for the RT coupling of Propagator Matrix or other results into a FE calculation. To couple energy from a source outside the FE grid into the FE calculation it is necessary to specify the displacement time history of a column of nodes. An additional option to allow the specification of displacement as a function of time for any node or nodes within the grid was added to the basic SWIS code. This option allows the specification of a time history constraint at up to two hundred nodes. However, if time history constraints are specified at more than one node, they must have a common duration at all nodes used. Constraints used to define boundary conditions are defined separately and persist for the entire calculation. The time history constraints can have any duration. If the duration of the constraint is less than the duration of the calculations then the constrained nodes are released when the time t within the calculation exceeds the duration of the constraint. If the duration of the constraint exceeds the duration used to define the length of the calculation then only the first portion of the constraining displacement time histories are used.

A second modification to the SWIS FE code was added to enable the production of time slices, or 'snapshots' of the motions at each node within the grid at a chosen time t. This option allows the code to write a file which contains the displacements at every node in the grid, or at every node in a decimated grid every n time steps. If a decimated grid is chosen it is specified by an integer decimation factor. If this factor has a value l then in a given row (l-1) nodes are skipped between each node for which a value is recorded, and (l-1) rows of nodes are skipped between each row where displacements are recorded. These displacements are then plotted to produce a series of figures showing the displacement as a function of location within the grid at a selection of times. The sequence of plots illustrates how the energy propagates through the grid as a function of time.

The final, and most important addition to the SWIS code was the SH hourglass correction terms. The finite element (FE) code uses a one-point quadrature integration rule so stresses are evaluated only at the center of mass of each element. Consequently any stress state that produces non-constant stress within an element is not treated completely in the calculation. Such a stress state can be decomposed into the sum of a constant stress state, which the one point integration represents exactly, and a non-constant stress state with zero stress at the centroid, known as the hourglass mode. To account for the hourglass modes in a code which uses one point integration an additional term is added to the restoring force. The form of this term for SH or antiplane motion is explained and derived below. For the in plane or P-SV problem corresponding hourglass modes occur as discussed by Kosloff and Frazier (1978). In all cases the hourglass term in the restoring force is calculated using similar procedures.

Figure 1a) shows a 2-D rectilinear element of the type used in the SH Finite Element calculations, and the form of the hourglass deformation present for SH motion of such an element. This deformation lifts one pair of diagonally opposite element corners and depresses the other pair of corners by the same amount, producing no stress or dispacement at the centroid of the element. Since the Finite Element code depends upon evaluation of stress only at the centroid of each element, it is singular with respect to such deformation. A correction to the restoring forces must be made to offset this hourglass motion. This correction must be singular with respect to constant stress states and rigid body translations. The constant-stress states produce motions as shown in Figure 1b) and 1c). It is clear that no sum of these motions and a translation in y will produce the deformation shown in 1a). Thus, the hourglass deformation is indeed singular with respect to translations and constant-stress states.

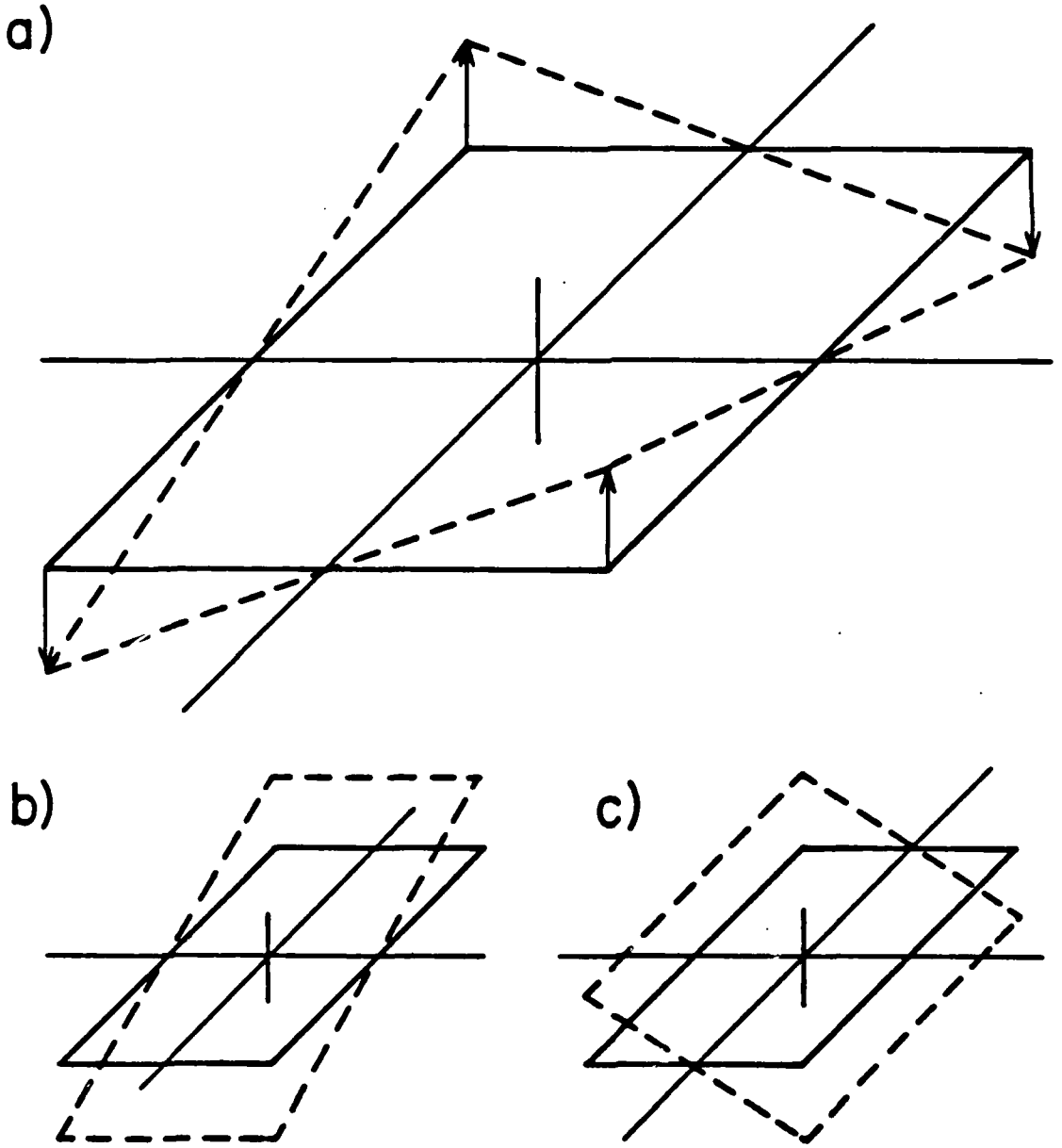

Figure 1: Types of SH motion of a 2-D rectilinear element. a) shows the hourglass mode for SH motion. Arrows at the element corners show the direction of displacement in y. The displacement and stress at the centroid (coordinate origin) of the element are zero. b) and c) show the motions accounted for in the uncorrected stiffness matrix, the constant stress modes.

For a body undergoing pure antiplane (SH) deformation, perpendicular to the x-z plane, the following conditions are satisfied:

$$\begin{aligned} &\text{a)} \quad u_x = u_z = 0. \\ &\text{b)} \quad \sigma_{ii} = 0. = \sigma_{xz} \\ &\text{c)} \quad \sigma_{xy} = \mu \frac{\partial u_y}{\partial x} \\ &\text{d)} \quad \sigma_{zy} = \mu \frac{\partial u_y}{\partial z} \end{aligned} \tag{13}$$

These relations are used as a basis to derive the form of this hourglass correction factor to the restoring forces for the case of SH motion. Using equations (7), (8) and (9) and the equation (14) below, from Zienkiewicz (1971), the hourglass correction to the restoring force at node m, R_i^m, can be calculated. The details of this calculation are given in the following paragraphs. Equation (14) expresses the hourglass restoring forces on each node in terms of the interpolation functions, the tractions on the surfaces of the surrounding elements and the body forces in those elements.

$$R_i^m = \sum_{e_m} \int_{V_e} h_i P^m(z) dV + \sum_{e_m} \int_{S_\sigma} P^m(z) T_i dS \tag{14}$$

where

h_i — body forces in volume V, i component i=1, ..., D

S_σ — the portion of the element surface S on which tractions T_i are specified

$\sum_{e_m}$ — sum over all elements bounding the node

To calculate the hourglass restoring forces the traction, T_i, on the element surfaces are needed. The quantities used as tractions for the purpose of calculating hourglass restoring forces are the stresses σ_{xy} and σ_{zy}. Consider the 2-D rectilinear element illustrated in Figure 2, with a linear varying traction σ_{zy} applied to its sides at $z=\pm b$ and σ_{xy} applied to its sides at $x=\pm a$. Let the form of the tractions σ_{xy} be

$$\sigma_{xy} = \mu \frac{\partial u_y}{\partial x} = \sigma_0 z \tag{15}$$

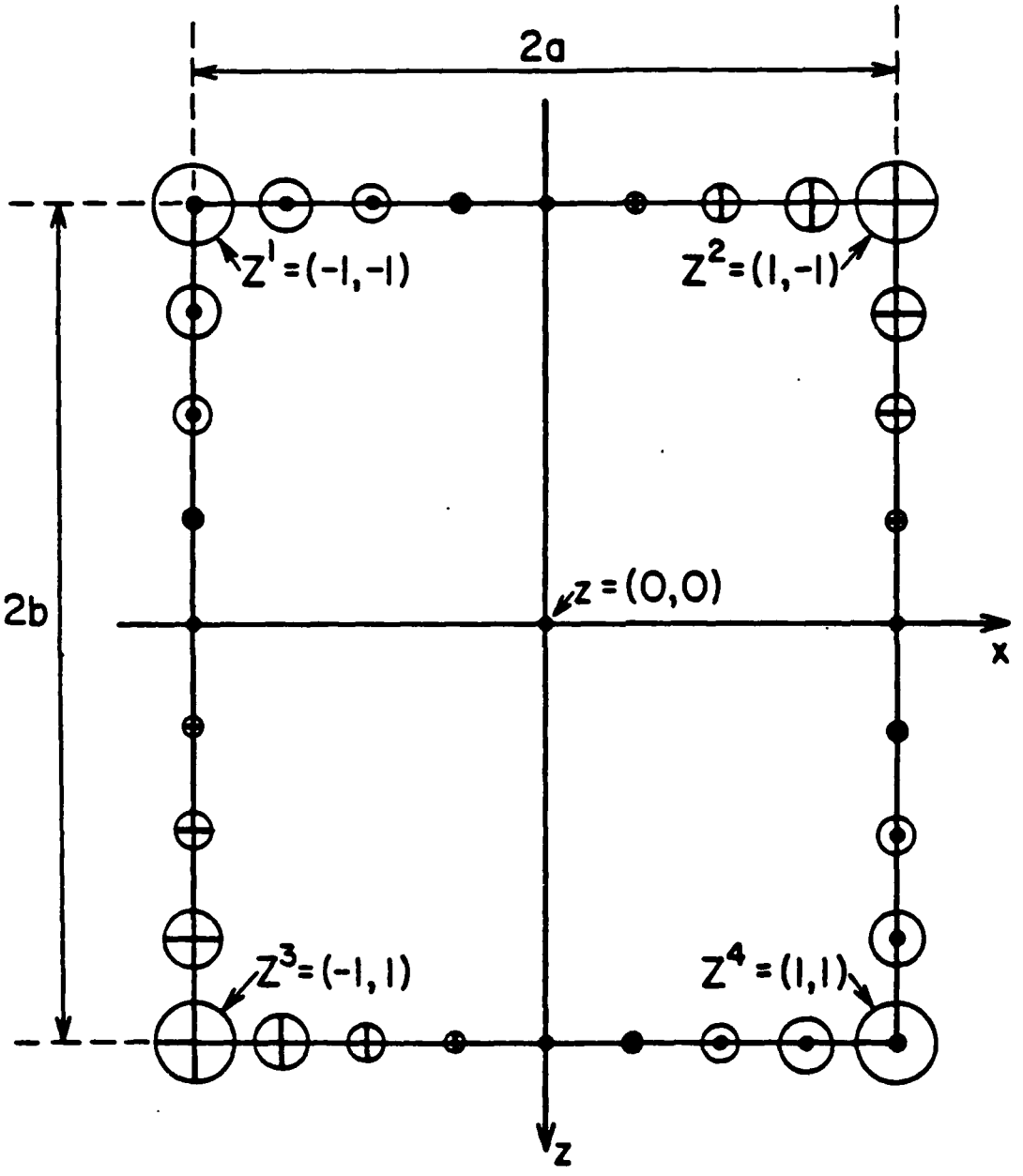

Figure 2: Configuration of an element used to calculate hourglass restoring forces for 2-D SH motion. The diameters of the circles on the element edges indicate the amplitudes of the applied tractions T_i ($T_i = \sigma_{xy}$, $x=\pm a$, $T_i = \sigma_{zy}$, $z=\pm b$) at selected points. Variation between illustrated points is linear. Circles with embedded crosses indicate motion into the page. Those with embedded dots indicate motion out of the page. Z_i are the natural coordinates of the nodes. The lengths a, b are the dimensions of the element in the Cartesian coordinate system.

From this relation u_y can be determined by integrating σ_{xy} with respect to x.

$$u_y = \int \sigma_0 z dx. = \sigma_0 zx + f(z) \tag{16}$$

However, at x=0, z=b, u_y=0 so f(z)=0. Now u_y at each of the j nodes surrounding element e may be determined. Expressing the u_y for node m, m=1,..,j, as the m^{th} element of a vector $\{U_y\}$, and defining the unit vector $\{1\}$ to carry the sign information as

$$\left\{1\right\}^T = \left\{-1, 1, 1, -1\right\} \tag{17}$$

enables the y displacements at the nodes to be written

$$\left\{U_y\right\} = \begin{Bmatrix} u_y(-1, 1) \\ u_y(1, 1) \\ u_y(-1,-1) \\ u_y(1,-1) \end{Bmatrix} = \frac{\sigma_0 ab}{\mu}\left\{1\right\} \tag{18}$$

Simple manipulation of (18) leads to the following expression for σ_0

$$\sigma_0 = \frac{\mu}{4ab}\left\{1\right\}^T\left\{U_y\right\} \tag{19}$$

It should also be noted that equations (16), (13a), and (13d) lead directly to an expression for σ_{zy}

$$\sigma_{zy} = \mu\frac{\partial u_y}{\partial z} = \sigma_0 x \tag{20}$$

Now we have the expression for the traction $T_i = \sigma_{zy}, \sigma_{xy}$ to be used in equation (9) to calculate the restoring forces. For a 2-D quadrilateral element subject to (13) the body forces h_i are zero so the first term in (9) vanishes and the interpolation functions become

$$P^m(z) = \frac{1}{4}\left(1 + z_1 Z_1^m\right)\left(1 + z_2 Z_2^m\right) \tag{21}$$

Substituting (21) into (14) gives the following expressions for R^m, the hourglass restoring forces.

$$R^1 = -\int_{-a}^{a} \frac{1}{2}(1-z_1)\,\sigma_0 x\,dx + \int_{-b}^{b} \frac{1}{2}(1+z_2)\,\sigma_0 z\,dz = \sigma_0 \frac{(a^2+b^2)}{3}$$

$$R^2 = \int_{-a}^{a} \frac{1}{2}(1+z_1)\,\sigma_0 x\,dx + \int_{-b}^{b} \frac{1}{2}(1+z_2)\,\sigma_0 z\,dz = -\sigma_0 \frac{(a^2+b^2)}{3}$$

$$R^3 = -\int_{-a}^{a} \frac{1}{2}(1-z_1)\,\sigma_0 x\,dx - \int_{-b}^{b} \frac{1}{2}(1-z_2)\,\sigma_0 z\,dz = -\sigma_0 \frac{(a^2+b^2)}{3} \tag{22}$$

$$R^4 = \int_{-a}^{a} \frac{1}{2}(1+z_1)\,\sigma_0 x\,dx - \int_{-b}^{b} \frac{1}{2}(1-z_2)\,\sigma_0 z\,dz = \sigma_0 \frac{(a^2+b^2)}{3}$$

Thus, in vector form the restoring forces are

$$\left\{R\right\} = -\sigma_0 \frac{(a^2+b^2)}{3}\left\{1\right\} \tag{23}$$

Substituting (15) in (19) gives the value of the restoring forces used in the SH FE code. Square elements were used, that is a=b, so the final form of the hourglass restoring force corrections are:

$$\left\{R\right\} = \frac{\mu}{6}\left\{1\right\}\left\{1\right\}^T\left\{U_y\right\} \tag{24}$$

This restoring force has been implemented in the version of SWIS used for all subsequent calculations

It remains to be shown that these corrections are necessary and adequate to allow the FE code to produce accurate results. To illustrate the effect of the corrections two test examples were completed, each of them with and without the hourglass restoring

force terms. The first example uses a point source located at one of the nodes within the grid. This source configuration is known to be a severe test of the stability of a FE or finite difference (FD) calculation. The second example uses a two step procedure, the validity of which will be demonstrated later, to couple energy propagated from a distant line source into the FE calculation through the edge of the FE grid. This procedure produces a more stable source and introduces hourglass instabilities only in the FE portion of the path. Consequently, smaller differences are introduced into the results when hourglass restoring forces are omitted.

Results of the first set of calculations, using the line source within the grid, are shown in Figure 3. The line source is located at a depth of 10 km from the free surface and a horizontal distance of fifty kilometers from the left hand grid edge. The grid has dimensions of 200x100 nodes, and node spacing of dx=dy=0.5 km. All calculations use a time step of 0.05s. The displacement time history of the source is a triangle eight time steps wide with a rise time of four time steps. Each group of three seismograms shown in Figure 3 is recorded at a given node. The nine nodes for which seismograms are illustrated surround four adjacent elements that share a common node. That common node is 12.5 km from the source, at the same depth as the source. The geometric arrangement of the groups of seismograms in Figure 3 is identical to that of the nodes at which they are recorded. The maximum amplitude of each trace is normalized to one. The uppermost seismograms in each group of three seismograms in Figure 3 is calculated by direct numerical evaluation of the analytic expression for the propagation of waves from a line source through a half-space. This expression is

$$u_y(x,z,t) = \int_{r_1/v}^{t} \frac{f(t-\tau)}{\left[\tau^2 - r_1^2/v^2\right]} d\tau + \int_{r_2/v}^{t} \frac{f(t-\tau)}{\left[\tau^2 - r_2^2/v^2\right]} d\tau \qquad (25)$$

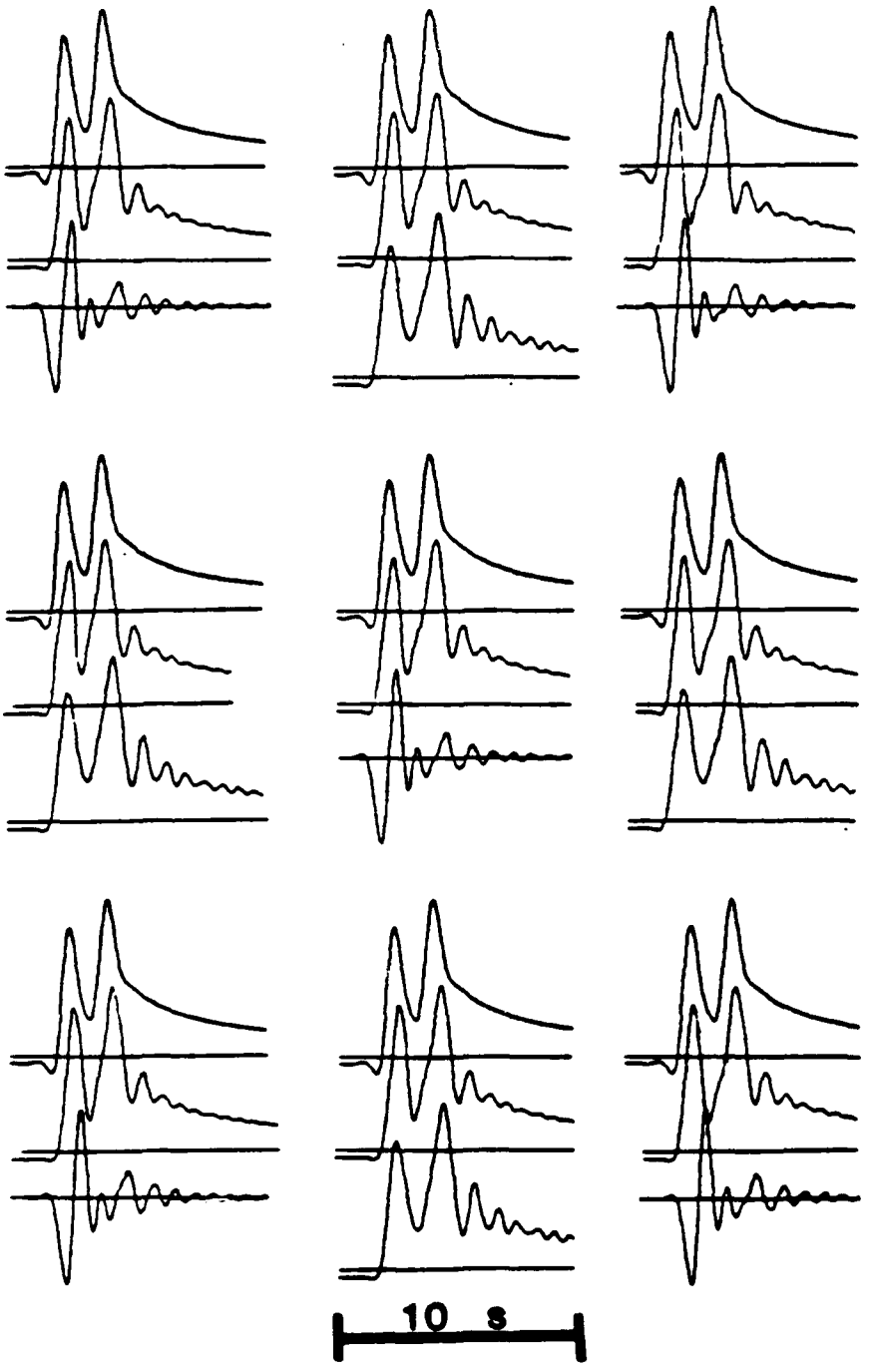

Figure 3: Waveforms for synthetic and FE seismograms calculated at nine adjacent nodes. Amplitude of each trace is normalized to one. Each group of three traces is recorded at one node. The groups of traces are displayed in the same geometrical arrangement as the nodes at which they are recorded. The central node is at a depth of 10 km, 12.5 km from a 10 km deep source. The spacing between the illustrated nodes is 0.5 km. In each group the top trace is synthetic, the second trace is a FE result including hourglass restoring forces, and the third trace is a FE result without hourglass restoring forces.

Where r_1 is the direct source to receiver distance, r_2 is the source to receiver distance for the reflection from the free surface, v is the SH wave velocity in the half-space, t is the time of observation with t=0 being the origin time, and x and z are the receiver coordinates. The first term on the right hand side of this equation gives the direct arrival, the second term the reflection from the free surface. The first peak in each synthetic is the direct arrival, the second peak is the free surface reflection. The central seismogram in each group is the FE result including the hourglass restoring forces. The last seismogram in each group is the FE solution omitting the hourglass terms. The waveforms and amplitudes for the first two traces in each group differ mainly in that some spurious oscillations are present in the FE solution. These oscillations are due to instabilities caused by the finiteness and high frequency of the source. The waveforms for the FE solution without hourglass corrections show marked discrepancies when compared to either the corrected FE solutions or the synthetics. For alternate nodes in any row or column these discrepancies have a different character. In one case the shape of the waveform shows only a small discrepancy and the peak amplitude is increased by more than 10%. In the other case the entire character of the waveform changes and the amplitude decreases by at least 20%. Clearly the hourglass corrections are necessary if accurate results are to be determined.

The second example used a 100x100 node FE grid whose first column is 1500 km from a ten kilometer deep line source in a layer over a half space. The layer has density 2.7 g/cm^3 and SH wave velocity 3.5 km/s and the half space has density 3.2 g/cm^3 and SH wave velocity 4.5 km/s. The time step size and the vertical and horizontal spacing of nodes in the FE grid were identical to those used in the previous example. Seismograms were calculated for a group of nodes along the surface and down depth sections at twenty five, forty and sixty five nodes from the grid edge using a two step procedure. First, synthetic seismograms were generated at a horizontal

distance of 1500 km from the source, at the surface and at half kilometer depth intervals to a depth of thirty kilometers. These seismograms were used to constrain the displacement time histories of the leftmost column of nodes in the FE grid. It will be shown that applying such constraints completely specifies the distant source. Analytic synthetic seismograms were also generated at the same locations. The two step seismograms, which have been propagated through a FE grid for thirty to thirty five kilometers between 1500 km and the receiver should be identical to the analytic synthetics at the same receivers if the FE calculation is stable. Results from this test are shown in Figure 4. The pairs of two step seismograms illustrated show how the introduction of the hourglass corrections effects the waveform and amplitude of the results. The upper trace in each pair includes the hourglass restoring force the lower trace does not. At the scale of the figure the corresponding analytic synthetics are indistinguishable from the two step results with hourglass restoring terms. The uppermost number to the right of each trace is the ratio of the peak to peak amplitude of the illustrated trace to that of a synthetic calculated for the same location. The lower number is the same type of ratio using an RMS amplitude measure discussed in detail later. These three pairs of seismograms were recorded at the free surface at distances of 30, 32.5, and 35 km from the left hand grid edge. These distances illustrate the behavior of the amplitudes at adjacent nodes within the grid. Some intermediate nodes have been omitted, but the alternation of higher and lower amplitudes for the uncorrected synthetics is seen as long as an even number of nodes are skipped between illustrated nodes. Examining the illustrated results shows that adding the hourglass restoring force term makes a small but perceptible change to the waveform. This change produces a slight improvement to the already excellent correspondence between the FE and analytic waveforms. However, the important improvement made when hourglass restoring force terms are included is in the amplitude correspondence between the FE and synthetic results. When no hourglass corrections are made the amplitudes of FE

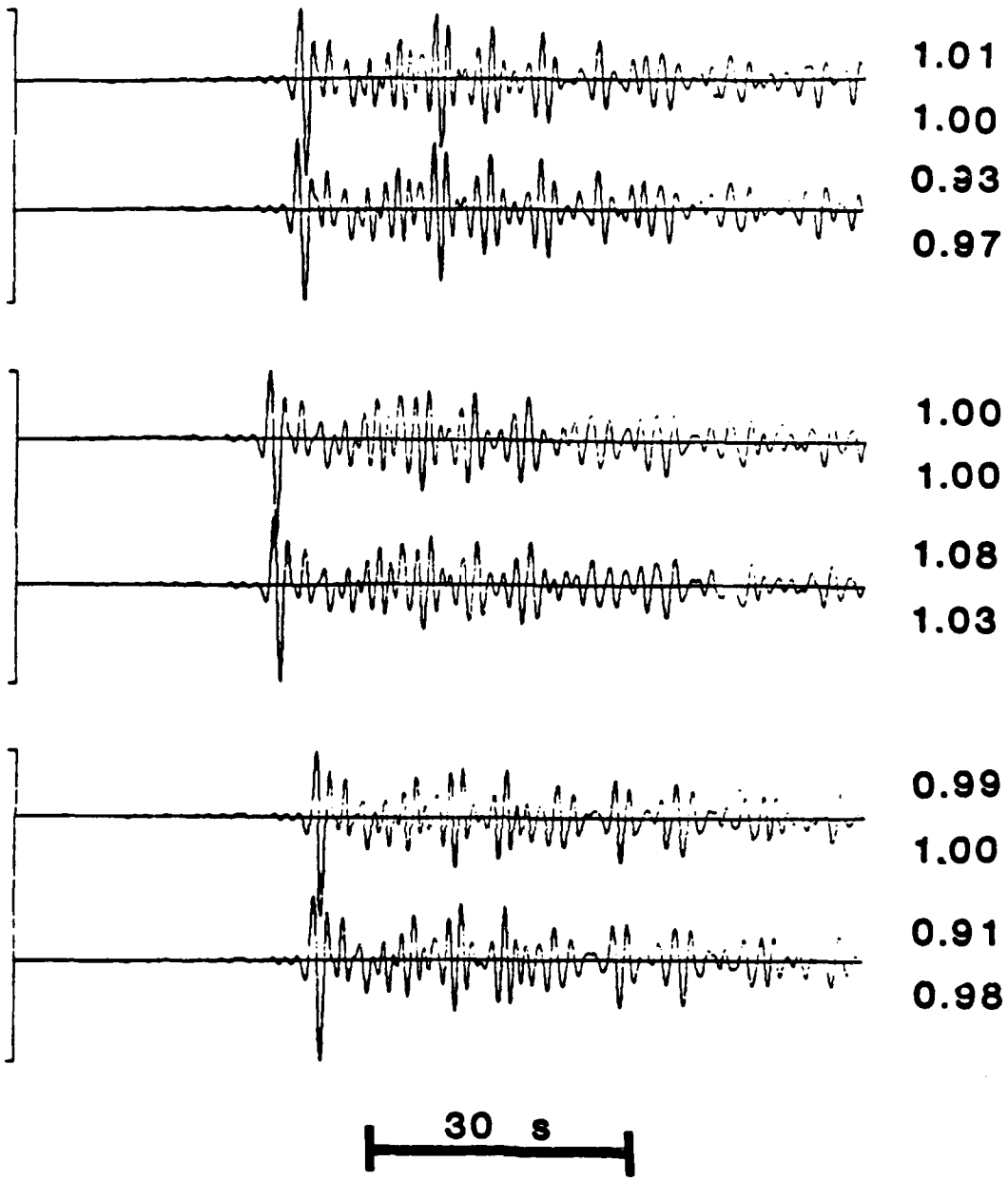

Figure 4: Waveforms for hybrid seismograms calculated in a FE grid removed from the source by a distance of 1500 km. Seismograms are calculated for a line source in a layer over a half-space. Each pair of seismograms is recorded at a given node. The upper trace in each pair includes the hourglass restoring force terms. The lower trace in each pair does not. The number to the right of each trace are amplitude ratios. The amplitude of the illustrated seismogram is compared to that of a synthetic calculated for the same location. The upper number is a ratio for peak to peak amplitudes, the lower for RMS amplitudes. Seismograms are of duration 102 seconds.

seismograms at successive nodes along any row or down any column alternate between being larger and smaller than those of the corresponding synthetics. Introduction of the hourglass restoring force terms removes this oscillation in the amplitude. Clearly the presence of the oscillatory term caused by the hourglass instabilities superimposed on the correct solution is not desirable. Thus, it is necessary to apply the hourglass restoring force correction to obtain the correct solution.

With these additions the SWIS FE code produces accurate solutions. However, the calculations are extremely time consuming. An effort was made to increase the speed of the calculations for the Cartesian SH option used for the calculations in this study. First, the options for general curvilinear and cylindrical coordinates were removed. Some small subroutines were incorporated into higher level routines to reduce the number of subroutine calls. The system was defined to have two dimensions and one degree of freedom thus removing a number of decision statements and blocks of code necessary to the implementation of other options. These changes also allowed the removal of a number of do loops and their replacement with single statements. Other modifications were made where incorporation of analytic simplifications of the expression being evaluated by the code substantially reduced the number of necessary calculations. The overall effect of these modifications was an increase of between a factor of four and and factor of five in the speed of execution of the modified and accelerated SWIS code over the original SWIS code for case of the propagation of SH waves in Cartesian coordinates.

The FE and propagator matrix methods used in the studies have now been explained, and the components of each which must be understood to explain the Representation Theorem coupling methods have been described. The modifications made to the SWIS FE code have increased the speed of the code by more than a factor of five. They have also allowed the application of time dependent displacement

constraints to selected nodes in the grid, and the recording of time slices, or snapshots of the motion of each node in the grid at a given time. These additional capabilities are utilized to implement the propagator to FE coupling, to allow the use of larger FE grids, and to better understand the propagation of disturbances through complex structures. Next it is necessary to understand the Representation Theorem (RT) and how it can be applied to coupling these two methods to produce a hybrid method utilizing the strengths of each.

The Representation Theorem and Green's Functions

The basis of the method used to couple the propagator matrix calculation to the FE calculation, or to couple the FE calculation into the Propagator matrix calculation is the application of the Representation Theorem on the boundary between the regions in which each method is used. The Representation Theorem (RT) relates the displacement at a point in a volume V to the body forces f_i in the volume V and to the displacements u and the tractions T_i on the surface S of volume V. There are many equivalent ways of expressing the RT, for example (Aki and Richards; eq 2.41)

$$u_p(\vec{x},t) = \int_{-\infty}^{+\infty} d\tau \iiint_V f_i(\vec{\xi}\,,\tau)\, G_{ip}(\vec{x},t-\tau\,;\,\vec{\xi},0)\, dV(\vec{\xi}) \qquad (26)$$

$$+ \int_{-\infty}^{+\infty} d\tau \iint_S \left\{ G_{ip}(\vec{x},t-\tau\,;\,\vec{\xi},0)\, T_i\left[\,\vec{u}(\vec{\xi},\tau),\, n_j\right] - c_{ijkl}\frac{\partial}{\partial x_l} G_{kp}(\vec{x},t-\tau\,;\,\vec{\xi},0)\, u_i(\vec{\xi}\,,\tau)\, n_j \right\} dS(\vec{\xi})$$

where $\vec{\xi}$ the location of a point of the surface S of volume V, $\vec{x}$ the location of a receiver in volume V, $u_p(\vec{x},t)$ is the p component of the displacement at time t at the receiver location, $\vec{x}$, t is the time at which the observation is made, τ is the source time, $T_i(\vec{\xi}\,,\tau)$ is the boundary condition specifying stress as a function of source time τ for all points on surface S, n_j is the j^{th} component of the outward unit normal to the surface S, $u_i(\vec{\xi}\,,\tau)$ is the boundary condition specifying displacement as a function of source time τ for all points $\vec{\xi}$ on the surface S, and G_{ip} is the Green's function which

represents the displacement in the i^{th} direction at $\vec{x}$ at time t due to a unit impulse applied in the p^{th} direction at position $\vec{\xi}$ at time τ. The desired Green's functions are obtained by solving the wave equation below in volume V, subject to the initial conditions that G_{ip} and $\frac{\partial}{\partial x} G_{ip}$ are zero for $t \leq \tau$.

$$\delta_{ip}\,\delta(\vec{x}-\vec{\xi})\,\delta(t-\tau) = \rho\frac{\partial^2}{\partial t^2}G_{ip}(\vec{x}\,,\,t\,;\,\vec{\xi}\,,\,\tau) - \frac{\partial}{\partial x_j}\left\{c_{ijkl}\frac{\partial}{\partial x_l}G_{kp}(\vec{x}\,,\,t\,;\,\vec{\xi}\,,\,\tau)\right\} \quad (27)$$

The form of the RT given as equation (26) is not optimal to demonstrate how the coupling of the two methods is accomplished. To transform it to a more manageable form several conditions are applied. First, it is assumed that no body forces are present within volume V. Thus, the first term on the right hand side of equation (26) vanishes. Next, the medium is assumed to be isotropic. This reduces the number of independent c_{ijkl} terms to nine from eighty one. It allows them to be written as

$$c_{ijkl} = \lambda\,\delta_{ij}\,\delta_{k_L} + \mu\,(\delta_{ik}\,\delta_{jl} - \delta_{il}\,\delta_{jk}) \quad (28)$$

Using these values of c_{ijkl} the tractions T_i can be expressed as

$$T_j = \tau_{ij}\,n_i = c_{ijpq}\frac{\partial}{\partial \xi_q}u_p(\vec{\xi}\,,\,\tau)\,n_j = \left\{\lambda\,\delta_{ij}\,u_{l,l} + \mu\,(u_{i,j} + u_{j,i})\right\}\,n_j \quad (29)$$

Substituting (28), and (29) into (26) a more useful form of the RT is found.

$$u_p(x,t) = \int_{-\infty}^{+\infty} d\tau \iint_S \left\{G_{pi}\tau_{ij} + \lambda G_{pl,l}\,u_j + (G_{pi,j} + G_{pj,i})\,u_i\right\}\,n_j\,dS(\vec{\xi}) \quad (30)$$

Where all derivatives are with respect to $\vec{\xi}$. For the case of SH waves only, (30) can be further simplified by applying the conditions governing SH motion and by assuming all quantities are constant with respect to x_2, that is

$$\Gamma_{22} = \frac{1}{2\pi\rho\beta^2} K_0(sr/\beta) = \frac{1}{2\pi\mu} \int_{r/\beta}^{\infty} \frac{1}{\left[t^2 - r^2/\beta^2\right]^{1/2}} e^{-st}\, dt \qquad (34)$$

$$= \frac{1}{4\pi\mu} \int_{-\infty}^{\infty} \exp \frac{\left[-(s/\beta)(\xi^2 + r^{2)^{1/2}}\right]}{(\xi^2 + r^{2)^{1/2}}} d\xi$$

where $r^2 = (x_1 - \xi_1)^2 + (x_3 - \xi_3)^2$. This form is valid for a whole space, and must be modified to satisfy the half-space problem. The whole space problem is a solution to equation (27) subject to the radiation condition that $\Gamma_{22} \to 0$ and $\frac{\partial \Gamma_{22}}{\partial r} \to 0$ as $r \to \infty$. For the half-space problem Γ_{22} must satisfy an additional BC as well as satisfying equation (27) and the radiation condition. The BC Γ_{22} must satisfy is that there be no stress, σ_{xy}, on the free surface. That is, the relation $\frac{\partial \Gamma_{22}}{\partial z} = 0$, must be satisfied on the free surface, at z=0. This is equivalent to specifying that volume V is a half-space rather than a whole space. Physically, the introduction of the free surface boundary at z=0 implies that energy that would otherwise continue to radiate towards infinity will instead be reflected back toward the depth of the receiver. This implies that the addition of a term of the same form as the whole space solution, so that it will satisfy the original equation, but with the propagation distance r equal to the propagation path length of a surface reflection rather than a direct arrival, will satisfy the zero stress BC at the surface. The half-space Green's function for a SH line source given below is based on this reasoning and can be shown to satisfy the BC, the radiation condition, and the initial equation.

$$\Gamma_{22}(\vec{x}; \vec{\xi}) = \frac{1}{2\pi\mu} \left[K_0(sr^-/\beta) + K_0(sr^+/\beta)\right] \qquad (35)$$

AD-A193 563 BODY AND SURFACE WAVE MODELING OF OBSERVED SEISMIC EVENTS PART 1(U) CALIFORNIA INST OF TECH PASADENA SEISMOLOGICAL LAB R W CLAYTON ET AL. 11 MAY 87 2/2

UNCLASSIFIED AFGL-TR-87-0157 F19628-85-K-0017 F/G 8/11 NL

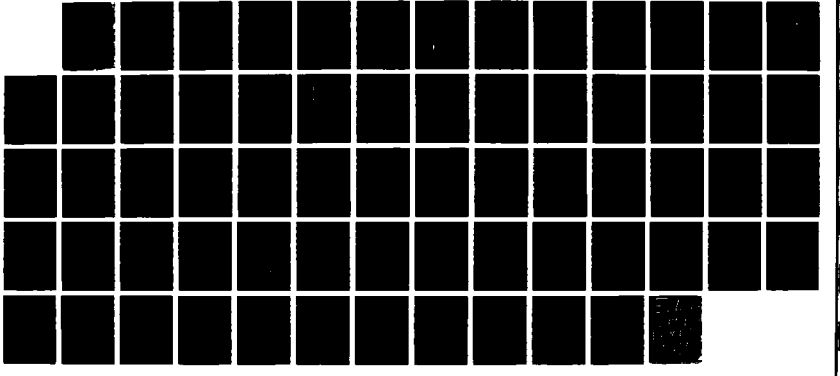

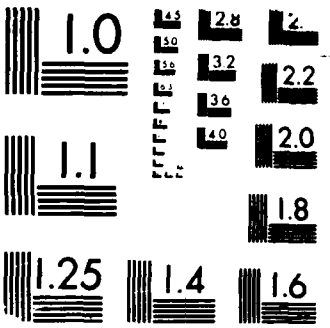

$$u_1 = u_3 = 0 \tag{31}$$

$$\tau_{11} = \tau_{33} = \tau_{13} = \tau_{31} = 0$$

$$G_{j1} = G_{j3} = G_{3j} = G_{1j} = 0$$

$$-\frac{\partial}{\partial x_2} = \frac{\partial}{\partial \xi_2} = 0$$

Also, it is usual to assume that the motion and stress are everywhere zero for times less than τ=0. Applying this condition and the conditions given in (31) to (30) and integrating from $-\infty$ to ∞ over x_2 gives the form of RT appropriate for a 2-D SH line source.

$$u_2(\bar{x},t) = \int_0^\infty d\tau \int_C \mu \left\{ \Gamma_{22} u_{2,k} + \Gamma_{22,k} u_2 \right\} n_k dC(\xi_1,\xi_3,\tau) \tag{32}$$

where C is the curve defined by the intersection of the surface S with the x_1–x_3 plane, and following the notation of de Hoop (de Hoop 1958)

$$\Gamma_{ij} = \int_{-\infty}^{+\infty} G_{ij}(x_1,x_3,t)dx_2 \tag{33}$$

Omitting the integration over x_2 gives a SH RT appropriate for a 3-D analogue of the procedure described below. Further discussions in this chapter relate to the 2-D problem.

The form of the line source Green's function given by de Hoop (de Hoop 1958) is

where $r^{\pm} = \sqrt{(x_1-\xi_1)^2 + (z\pm\xi_3)^2}$. To compare this form for the Green's functions to the forms of the displacements used in the rest of this discussion it is first necessary to transform the equation from the Laplace transform domain to the Fourier transform domain, and to express the modified Bessel function, K_0, in terms of Hankel functions or of exponentials. Examining the second expression in the first line of equation (34) indicates that it is the Laplace transform of a quantity, f(r,z), where f(r,z) is the first term in the integrand. Applying the change of variables, $\xi^2 = (vt)^2-r^2$, changes the lower limit of integration to zero and the integration variable to ξ. Then, noticing the symmetry of the resulting integrand allows the lower limit of the integral to be changed to $-\infty$ if a factor of one half is introduced. This gives the form of the equation in the second line of equation (34). Finally, introducing an additional change of variables, $s = i\omega$, changes the Laplace transform to a Fourier transform. The resulting expression for the Green's function is

$$\Gamma_{22} = \frac{1}{2\pi\mu}\left[K_0(ik_\beta r^+) + K_0(ik_\beta r^-)\right] \qquad k_\beta = \frac{\omega}{\beta} \tag{36}$$

Next, it is useful to transform the modified Bessel functions, K_0, into Hankel functions to make direct comparison with the displacement solution for the line source in a layered half-space possible. The modified Bessel function can be expressed in terms of Hankel functions (Abramowitz and Stegun, eq 9.6.4)

$$K_\nu(z) = \frac{-i\pi}{2} e^{\frac{i\pi}{2}\nu} H_\nu^{(2)}\left(ze^{-i\pi/2}\right) \qquad -\frac{\pi}{2} < \arg(z) \leq \pi \tag{37}$$

The argument of the modified Bessel function, $ik_\beta r$, is of the form ix where x is a positive real number. Thus, $\arg(z)=\frac{\pi}{2}$, and the expression (37), is applicable. Substituting equation (37), with $\nu=0$, into equation (36) gives the first expression in the next group of equalities. It is in the form that it can be directly compared to a line source displacement expression for a homogeneous half-space that is used in the propagator

technique to develop the expression for the layered half-space. This expression is

$$\overline{v}(r,\phi,z) = \frac{i\pi}{2}\left[H_0^{(2)}(k_\beta r^+) + H_0^{(2)}(k_\beta r^-)\right] \tag{38}$$

Alternately, the equation (36) can be written in terms of integrals of exponentials and then be compared directly to the solution for a line source in a homogeneous half-space. The exponential form of the equation is the result of substituting the appropriately transformed version of the integral expression in equation (34) for each modified Bessel function in equation (36). This representation of the Green's function is given as the second equality in the next group of equations.

$$\Gamma_{22} = \frac{-i}{4\mu}\left[H_0^2(k_\beta r^+) + H_0^2(k_\beta r^-)\right] \tag{39}$$

$$= \frac{1}{2\pi\mu}\left[\int_{r_1/\beta}^{\infty} \frac{1}{\left[t^2 - r_1^2/\beta^2\right]^{1/2}} e^{-i\omega t} dt + \int_{r_2/\beta}^{\infty} \frac{1}{\left[t^2 - r_2^2/\beta^2\right]^{1/2}} e^{-i\omega t} dt\right]$$

Comparing the second equality in equation (39) to equation (25) for the line source in a homogeneous half space, and comparing the first equality in (38) to the alternate expression for the line source in the homogeneous half-space, equation (38), shows that

$$\overline{u_y}(x,z) = \frac{1}{2\pi\mu}\Gamma_{22}(\overline{x};\overline{\xi}) \tag{40}$$

Thus, the displacement Green's function can be calculated in a manner identical to the displacement solution, in either a layered half-space or a homogeneous half space. However, one must be careful to include the multiplicative factor of $\frac{1}{2\pi\mu}$ when determining the Green's functions for use in the Representation Theorem expressions.

The form of the Representation Theorem (RT) given in equation (32) has been used to determine approximate analytic solutions to the problems of propagation across a surface step (Knopoff and Hudson 1964), and of propagation in a layered elastic wedge (Hudson and Knopoff 1964). This is also the form used in this study to develop procedures for the coupling of FE and Propagator Matrix solutions.

Figures 5 and 6 show geometries useful for developing and explaining the methods to be used for coupling FE and propagator matrix methods. The purpose of developing these methods is to allow the propagation of wavefields from a source to a receiver through a series of plane layered media separated by complex regions that cannot be modeled using a plane layered structure, or by changes in the layered structure. For example, the complex regions that will be considered in chapter 2 are continent to ocean and ocean to continent boundaries. A simple geometry, consisting of a layer over a half-space, is used as a test case to show how the methods work, and how they can be applied in both this simple case and in more complicated cases. Figure 5 can be used to illustrate the geometry used to couple energy traveling through a layered medium, into a FE grid which may contain structures of arbitrary complexity. Figure 6 can be used to illustrate the coupling from such a FE grid into a layered structure where propagator matrix methods are used to transmit the energy further. Each of these figures will be discussed in detail later.

Propagator to Finite Element Coupling

In a layered medium the wavefield can be mathematically constructed at any point receiver within the layered half-space using the propagator matrix technique and an appropriate form of a source representation. The resulting seismogram at any point in the layered half-space will include not only a direct arrival and a surface reflection but also the superposition of many multiple reflections which produce the surface waves in the wavetrain. Although the seismograms are produced as modal

sums, in the limit of using all possible modes, they are equivalent to summing over all possible multiple reflections in terms of rays. Thus, they can be conceptualized in terms of rays. To simplify the graphical representation used in Figures 5 and 6 the seismogram at a source point in the layered half-space is represented by a single direct line from the source to the receiver. This line also implicitly represents all the reflected and multiply reflected rays in that seismogram which would hopelessly clutter the diagrams if they were included.

Figure 5 shows a graphical representation of a layer over a half-space. The source is represented by a large asterisk, and each receiver by a large point. The origin of the coordinate axes is also shown as a large point. The coordinate axes $x_1 = x$, and $x_2 = z$, are labeled at the origin of the Cartesian coordinate system used in this discussion. The arrows show the directions in which the values of each coordinate increase. The distance x increases to the right, the depth z increases downwards, and the coordinate $y = x_2$ increases out of the page. All motion occurs in the y direction since this is an SH wave problem. The free surface of the half-space is located at z=0, and the source is located at x=0 at depth h. The second long horizontal line is located at z=D, where D is the thickness of the layer above the half-space. The points denoting the receivers, also illustrate the locations of the nodes in two columns of a FE grid. The intervening columns of nodes are not illustrated to avoid cluttering the diagram. The short horizontal line that connects the lowermost nodes is at $z = D_{FE}$, and denotes the bottom of the FE grid. The FE grid is assumed to extend off the page toward the right. The vertical line connecting the leftmost column of receivers shows the lefthand edge of the FE grid. For the sake of simplicity and clarity the structure illustrated within the FE grid is the same layer over the same half-space as that used in the region traversed using the propagator matrix calculation.

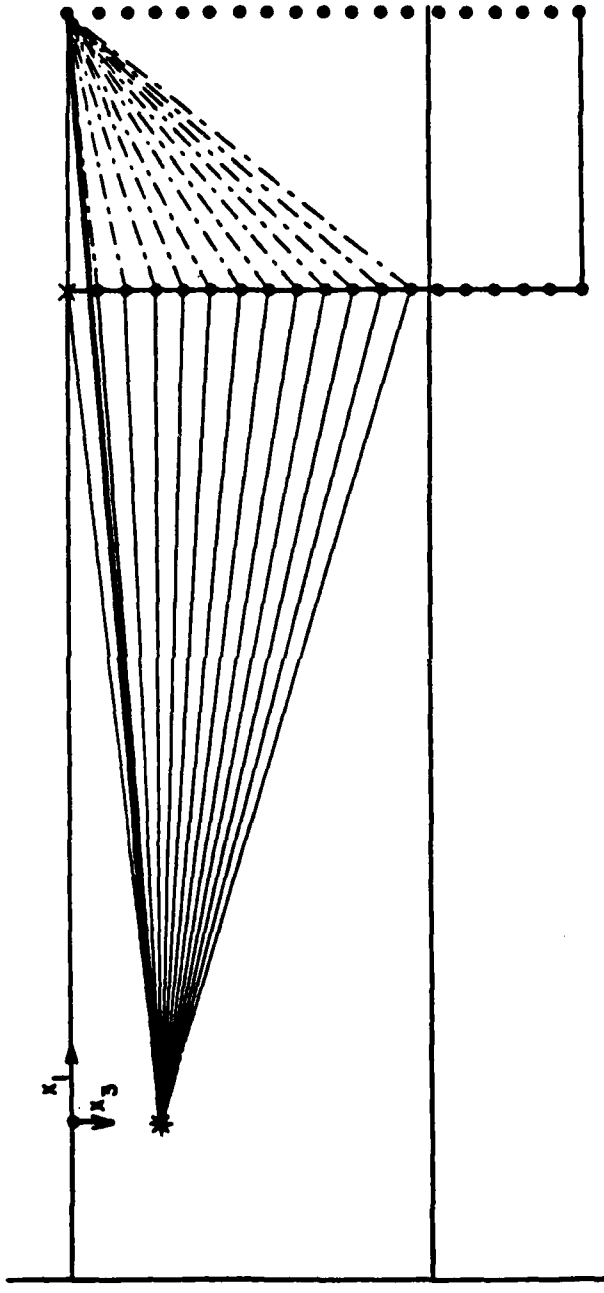

Figure 5: Geometry used to explain the coupling of propagator matrix seismograms from a source outside a FE grid into a FE grid. The two long horizontal lines show the free surface and the boundary between the layer and the half-space. The source is shown as an asterisk. Two columns of FE nodes are shown as dots. The vertical line connecting the dots and the short horizontal line perpendicular to it are the grid edges. The heavy solid line from the source to the surface reciever in the grid denotes the direct analytic seismogram, the solid lines between the source and the grid edge nodes denote the direct forcing functions, and the dotted lines indicate the source to reciever paths, for the sources created by the application of the forcing functions at the grid edge, that integrate to give the hybrid seismogram.

The coupling of a wavefield defined by the discrete sampling of seismograms along the leftmost edge of a FE grid, into that FE grid is straightforward. The seismograms, for a specified source function, are generated at a group of receivers equally spaced in z located a horizontal distance X from the source. The depth spacing Δz between the receivers is the node spacing in the FE grid into which the wavefield is to be coupled. The distance X is the minimum separation between the source and the lefthand edge of the grid. The solid lines connecting the source to the receivers along the left edge of the grid illustrates these seismograms. They are calculated by transmitting the appropriate source functions through the layer over a half-space structure from the source to the leftmost edge of the FE grid by using the propagator matrix method. The seismograms are then applied as displacement time history constraints on the leftmost column of nodes in the FE grid. The application of this type of constraints to a column of nodes in the FE grid completely specifies the subsequent motion at all points in that FE grid. Thus, a hybrid seismogram can be recorded at any node in the FE grid provided a FE calculation of suitable duration is completed. Consider, as an example, that the receiver at which the hybrid and analytic seismograms are to be compared is the surface receiver at a distance X2 from the source. The minimum distance from the source to the second column of nodes illustrated in Figure 5 is X2. The heavy solid line in Figure 5 represents the analytic seismogram, calculated using only the propagator matrix method and the appropriate source functions. The hybrid seismogram is represented by the integration over all the dashed paths connecting the edge nodes and the receiver. Each dashed path represents a seismogram for which the appropriate forcing function is a time dependent source.

Figure 5 shows the layer over a half-space structure extending into the FE grid. A series of calculations completed using such a homogeneous structure provides a

useful test of the procedures used. It allows the comparison of the hybrid solutions, those solutions propagated from the source to the receiver using a combination of methods, to analytic synthetics, those calculated entirely with the source functions and the propagator matrix technique, for receivers in locations identical with respect to the source. Hybrid and analytic synthetics calculated by using the layer over a half-space structure in both portions of the path will be shown later. These seismograms will be used to demonstrate the validity of the coupling method by comparing the hybrid results to the analytic results. Although, in this example, the FE grid contains the same layer over a half-space structure as that used for the propagator matrix calculations, any other arbitrary structure can be put into the FE grid without altering the coupling method. However, the calculation of analytic synthetics to which the resulting hybrid synthetics can be compared may be difficult or impossible. Thus, although we wish to address the effects of complex structures within the FE portion of the path the simple case where the FE grid contains the same layered structure as used for the propagator matrix calculation will be discussed here as it is the best test of the method.

In the examples discussed in later sections the seismograms used as forcing functions are generated using more than one type of source. The first types of sources used are line sources, for a single point force in a homogeneous half-space or a layered half-space. For these cases the applied forcing functions are $u_y(x,y,z)$. However, the balance of the sources used are double couple point sources. The propagator matrix solutions for these sources are of the form $\bar{v}(r,\phi,z)$. The displacements are expressed in cylindrical coordinates rather than in the Cartesian coordinates appropriate to the RT integral or the Cartesian FE representation. Thus it must be demonstrated that these cylindrical displacements can be used in place of the Cartesian ones expected without adversely affecting the results. This will be demonstrated in the following paragraphs.

The expressions for $\bar{v}(r,\phi,z)$ for the dip slip and strike slip faults, equations (6), are in cylindrical coordinates (r,ϕ,z), where $r = \sqrt{(x^2+y^2)}$. Displacement time histories of a series of locations corresponding to the first column of nodes in a FE grid a distance r_1 from the source were evaluated using these expressions. When these displacement seismograms are used as input forcing functions then they are used as if $\bar{v}(r,\phi,z)$ was an expression for $\bar{u}_y(x,y,z)$ rather than for $\bar{u}_\phi(r,\phi,z)$. No transformation from cylindrical to Cartesian coordinates is performed. The displacement field defined by the imposition of displacement time history constraints down the FE grid edge is then propagated an additional distance, Δr, through the FE grid to give the hybrid seismograms that approximate $\bar{u}_\phi$ at the receiver. The validity of using $\bar{v}(r,\phi,z)$ rather than $\bar{u}_y(x,y,z)$ will now be demonstrated. It will be shown that for $r_1 >> \Delta r$ substituting u_ϕ for u_y gives a good approximation of u_ϕ at the receiver despite the fact that the FE method produces 2-D rather than 3-D propagation effects.

Consider a FE grid with its leftmost edge a distance r_1 from a source, and a receiver, where hybrid and analytic synthetic results are recorded, a distance r_2 from the source. Define the distance propagated within the FE grid as $\Delta r = r_2 - r_1$. Consider, also, the expressions (6) for the displacements from a point dip slip or strike slip source. Only variations in the r coordinate need to be discussed to establish the validity of this procedure so, for clarity, (6a) or (6b) will be reduced to,

$$\left\{\bar{v}(r,\phi,z)\right\} = \bar{v}_\omega(\phi,z)\,\frac{\partial H_\nu^{(2)}(k_L r)}{\partial r} \tag{41}$$

where $\nu = 2$ for a strike slip source and $\nu = 1$ for a dip slip source. The derivative of the Hankel function can be expanded in terms of undifferentiated Hankel functions using (Abramowitz and Stegun, eq 9.1.29)

$$\frac{1}{k_L}\,H_\nu^{(2)}(k_L r) = -\,H_{\nu+1}^{(2)}(k_L r) + \frac{\nu}{k_L r} H_\nu^{(2)}(k_L r) \tag{42}$$

Each resulting Hankel function can be expanded in terms of the asymptotic expansion of H_ν for large r (Abramowitz, Stegun, eq 9.2.4)

$$H_\nu^{(2)}(k_L r) = \sqrt{\frac{2}{\pi k_L r}}\, e^{-i(k_L r - \frac{1}{2}\nu\pi - \frac{1}{4}\pi)} \qquad -2\pi < \arg(k_L r) < \pi \tag{43}$$

Replacing the derivative of the Hankel function in equation (41) with the product of k_L and the right side of expression (42), gives an expression for $\left\{\overline{v}(r,\phi,z)\right\}$ including only undifferentiated Hankel functions. Substituting the asymptotic expansion, equation (43), for each of these Hankel functions gives an alternate expression for $\left\{\overline{v}(r,\phi,z)\right\}$. It is

$$\left\{\overline{v}(r,\phi,z)\right\} = \overline{v}_\nu(\phi,z)\sqrt{\frac{2}{\pi k_L r}}\left[k_L - \frac{\nu}{r}\right] e^{i\pi\frac{(2\nu-1)}{4}}\, e^{-ik_L r} \tag{44}$$

Since we are considering the case of r large, $k_L >> \frac{\nu}{r}$, and the second term in the square brackets can be ignored, $\left\{\overline{v}(r_2,\phi,z)\right\}$ can be expressed in terms of ϕ, z, r_1, and Δr as

$$\left\{\overline{v}(r_2,\phi,z)\right\} = \overline{v}_\nu(\phi,z)\sqrt{\frac{2k_L}{\pi(r_1+\Delta r)}}\, e^{i\pi\frac{(2\nu-1)}{4}}\, e^{-ik_L r_1}\, e^{-ik_L \Delta r} \tag{45}$$

$$= \left\{\overline{v}(r_1,\phi,z)\right\}\sqrt{\frac{r_1+\Delta r}{r_1}}\, e^{-ik_L\Delta r}$$

$$\approx \left\{\overline{v}(r_1,\phi,z)\right\}\, e^{-ik_L\Delta r} \qquad \Delta r << r_1 \qquad k_L r_1 >> 1$$

Now, for a line source in a half space, equation (25), or for a line source in a vertically inhomogeneous half-space, the modal relation analogous to equation (45) is,

$$u_\phi(x2,z) = u_\phi(x1,z)\, e^{-ik_L x2-x1} = u_\phi(x1,z)\, e^{-ik_L \Delta x} \tag{46}$$

Comparing (46) and (45) shows that both expressions have the same form. In each case the displacement at r_2 can be expressed as the displacement at r_1 multiplied by a propagation factor. A FE or RT calculation will give the same propagation factor for each mode as the analytic expression, (46), above. If the displacements at r_1, $\overline{v}(r_1,\phi,z)$ or $u_y(x,z)$, and the propagation factors, $e^{-ik_L \Delta r}$ or $e^{-ik_L \Delta x}$, are correlated by considering $x1=r_1$ and $\Delta x=\Delta r$, then $\overline{v}(r_1,\phi,z)$, the 3-D solution, will be given by $u_y(x,z)$, the result of the 2-D FE or RT calculation, so long as the source is many wavelengths, $k_L r$, from the boundary and r is normal to the FE grid edge or the RT integration surface.

Finite Element to Propagator Coupling

The coupling of FE seismograms into a layered media through which they are transmitted by the propagator matrix technique and the application of the RT, is accomplished by direct evaluation of the RT integral as given in equation (32) using propagator matrix generated line source Green's functions. The geometry of the problem is illustrated in Figure 6. The geometry will be explained, then the coupling procedure will be discussed.

Figure 6 shows the geometry used to evaluate the RT integral, equation (32). Again, the layer above a half-space model is illustrated in both the FE and propagator matrix regions for clarity. In practice any structure can be used in the FE grid. The two long horizontal lines show the free surface and the boundary between the layer and the half-space. The solid vertical line which does not have dots superimposed upon it is the righthand edge of the FE grid. The FE grid is assumed to continue off the figure to the left. The source can be assumed to be either in the FE grid itself or on the far side of the FE grid. The short horizontal line shows the bottom of the FE grid. The x's shown within the grid and on its bottom boundary represent nodes in

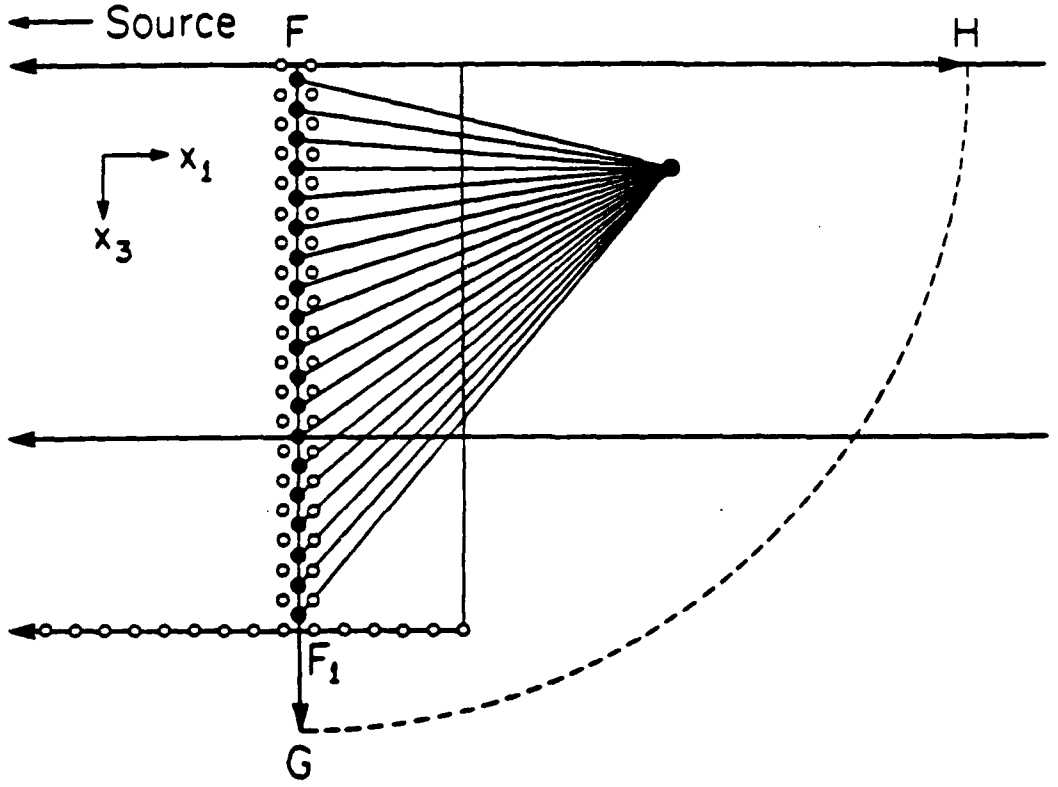

Figure 6: Geometry used to explain the coupling of FE stress and displacement time histories into propagator matrix calculations. The RT integration path, C, is shown as the closed curve FGHF. Finite element nodes are shown as open circles. The short vertical and horizontal lines are the boundaries of the FE grid. The two long horizontal lines show the free surface and the boundary between the layer and the half-space. The filled circles superimposed on the FG section of the integration path are element centers within the FE grid where stress and displacement time histories are recorded. The dot within the integration path denotes the receiver. The lines connecting the element centers and the receiver represent the line source Green's functions.

the FE grid. The two illustrated columns of nodes define the corners of a column of elements. The center of each of these elements is shown as a dot. The integration path, C, for the RT integral is illustrated as the closed curve FGHF. The arrows at G and H indicate that the integral is evaluated on the contour, C, where the x coordinate at G, and the z coordinate at H both tend to infinity. An example of a possible receiver inside the contour C is illustrated as a large dot outside the FE grid. The lines connecting the dots showing the column of element centers within the FE grid to the receiver represent the line source Green's functions for propagation from a source at the location of the element center to the receiver.

The evaluation of the RT integral on the contour, C, will be discussed in three parts. First the quantities used in the evaluation of the RT integral on the segment FG of the contour, C, will be discussed. Then, the procedure used to estimate the value of this integral will be explained. Finally, it will be shown that the contributions to the RT integral from integration along segments GH and HF of the contour, C, do not contribute to the solution.

Before the particulars of the integration procedure can be discussed, each of the quantities in equation (32) must be defined. The integration surface for the segment GH is a line with the x coordinate held constant, only the terms generated by setting k=1 in equation (32) need to be considered. Thus, the quantities of interest are, μ, u_y, σ_{xy}, Γ_{22}, and $\Gamma_{22,2}$. The displacement and stress time histories at the element centers, illustrated as dots in Figure 6, are recorded during the FE calculation. The element center displacement u_y, and the element center stress, σ_{xy}, are used as the u_2 and $\mu u_{2,1}$ terms respectively, in the RT integral (32). Line source Green's functions are calculated for the transmission of a unit line displacement, applied at each of the nodes illustrated as dots in Figure 6 at time t, to the receiver point. These Green's functions are calculated using the propagator matrix method. These displacement

Green's functions are the Γ_{22} terms in equation (32). The evaluation of the $\Gamma_{22,2}$ terms is analogous to the calculation of the displacement Green's functions. The details of this calculation will be discussed later when the evaluation of stress seismograms is discussed. Now, all the necessary time dependent quantities in the RT integral have been defined. It remains to note that the rigidity, μ, in equation (32) is the rigidity at the depth of the source.

The next step is to explain how the RT integral is numerically integrated. Consider the displacement and stress seismograms, and the displacement and stress Green's functions as time series. Each time series gives the amplitude of a displacement or a stress as a function of time. The time spacing between successive points in each time series is the time step duration, Δt, used in the FE calculation. It should be remembered that the terms $\Gamma_{22}u_{2,k}$ and $\Gamma_{22,k}u_2$, in the RT integral, equation (32), are convolutions. Thus, the evaluation of the integrand at each integration point is a four step process. First, each of the displacement and stress seismograms is Fourier transformed into the frequency domain. Then, the products of the Green's functions and FE results, $\bar{\Gamma}_{22}\bar{u}_{2,k}$ and $\bar{\Gamma}_{22,k}\bar{u}_2$, are calculated. In these expressions a bar denotes a Fourier transform. Next, the resulting products are inverse Fourier transformed back into the time domain. Finally, the sum of the two convolutions is determined and multiplied by the rigidity. Now, the value of the integrand at each element center on the integration surface is known. Integration along the segment FG or the contour, C, is approximated by taking the sum over the values of the integrand at each element center along the subsegment FF_1 of the segment FG times the segment length, and applying the assumption that the contributions to the integral from the remainder of segment FG are negligible. The assumption that no significant contribution is made by integration along segment F_1G can be justified for the case where F_1 is chosen so that the earliest possible arrival of energy from a source at depth F_1 is later

than the last arrival in the seismogram being considered. For the remainder of this discussion we will assume that the depth F_1 illustrated in Figure 6 satisfies this criterion. Thus, the integration of the RT integral on the segment FG of the contour, C, is expressed as a sum over the value of the integrand at each of the element centers along subsegment FF_1 times the segment length. This is equivalent to applying a trapezoidal rule numerical integration to the equation (32) along segment FF_1.

Next, the integration over the remaining two segments of the contour, C, will be shown to give no contribution to the RT integral. The segment of the contour FH, along the free surface will be considered first. The integration surface for the segment FH of the contour, C, is a line with the z coordinate held constant. Thus, only terms generated by setting k=3 in equation (32) need to be considered. The free surface boundary condition applied on this surface states that the is zero stress on this surface. Thus, at z=0 the stress, $\mu u_{2,3}$, is zero. Since the Green's function, Γ_{22}, used in all the calculations also satisfies the free surface BC, the Green's function stress, $\mu\Gamma_{22,3}$, is also zero at z=0. Therefore, one term in each product in the integrand of equation (32) is zero, causing the value of the integral along this portion of the contour, C, to be zero. Next, the segment GH of the contour, C, will be considered. As $r\rightarrow\infty$ the displacements Γ_{22} and u_2 must approach zero. The radiation BC used in deriving the expressions for these values imposes such a condition. Substituting the asymptotic expansion for H_ν into equation (38) and (39) and taking the limit as $r\rightarrow\infty$ also verifies this statement. Again, one component of each product in the integrand of equation (32) is zero. Clearly, this makes the integrand zero and verifies that the section GH of contour, C, makes no contribution to the RT integral.

In summary, the mechanics of the methods used to couple propagator matrix solutions into FE calculations and to couple FE results into the RT integral using line source Green's functions generated with the propagator matrix method are described

briefly. To couple propagator matrix solutions into a FE calculation three basic steps are necessary.

(1) Generate seismograms at an appropriate set of receivers using the desired source functions and the propagator matrix technique. An appropriate set of receivers consists of receivers at a fixed horizontal distance from the source, at depths corresponding to the nodes in the first column of the FE grid to be used in the FE calculation.

(2) Use this set of seismograms as displacement time history constraints on the left-most column of nodes in that FE grid.

(3) Record hybrid seismograms at the desired locations within the FE grid as the constrained FE calculation proceeds.

To couple results from a FE calculation back into a simple layered structure across which they can be transmitted using propagator matrix Green's functions and the RT integral five steps are needed.

(1) Record element center displacement and stress time histories from the FE calculation.

(2) Calculate line source displacement and stress Green's functions that will transmit a disturbance from each element center to the desired receiver.

(3) Fourier transform the displacement and stress time histories and the displacement and stress line source Green's functions into the frequency domain. Perform the multiplication of the displacement time history with the stress Green's function and the stress time histories with the displacement Green's functions. Inverse Fourier transform the products back into the time domain.

(4) Add the appropriate pairs of products and multiply by the rigidity to give the values of the integrand at each of the element centers.

(5) Sum the values of the integrands multiplied by their respective interval lengths along the integration surface to give the hybrid seismogram.

Tests of Accuracy: SH Pulse Input

The first, and the most basic, test of the validity of the RT formulation is the coupling of two successive FE calculations. This type coupling can in itself be used to advantage under some conditions, and will be referred to as grid extension in later discussions. For example, propagation through successive FE grids can be useful in some cases to deal with unwanted boundary reflections. As will be demonstrated later the transmitting BC used is angularly dependent, and removes little of the reflection at grazing or near grazing incidence. For FE calculations with large aspect ratios, that is $nx >> nz$, wide angle reflections from the grid bottom can contaminate the results. When seismograms of short duration are required these wide angle reflections can be avoided by using a series of small aspect ratio grids. For example, if a series of two small aspect ratio FE calculations are used to model a long aspect ratio problem then it should be possible to shift at least half the width of the grid without worrying about wide angle reflections. In that case two small grid runs of the FE would be faster than one run with an expanded grid. Thus, the grid extension would be worthwhile.

In Figure 7 a pair of fifty by fifty node grids are illustrated. A line force source, which is a point force when it is projected onto the x-z plane defined by the FE grid, is applied to the first node in the n^{th} row of nodes in the first, or upper grid. It is shown in the figure as an crossed circle on the left edge of the upper grid. The wide vertical line within this grid represent the sixteenth column of elements, where intermediate seismograms are recorded for later use as forcing functions input to the second step of the procedure. The narrow vertical line in the upper grid represents the thirty first column of nodes where direct seismograms representing results for a

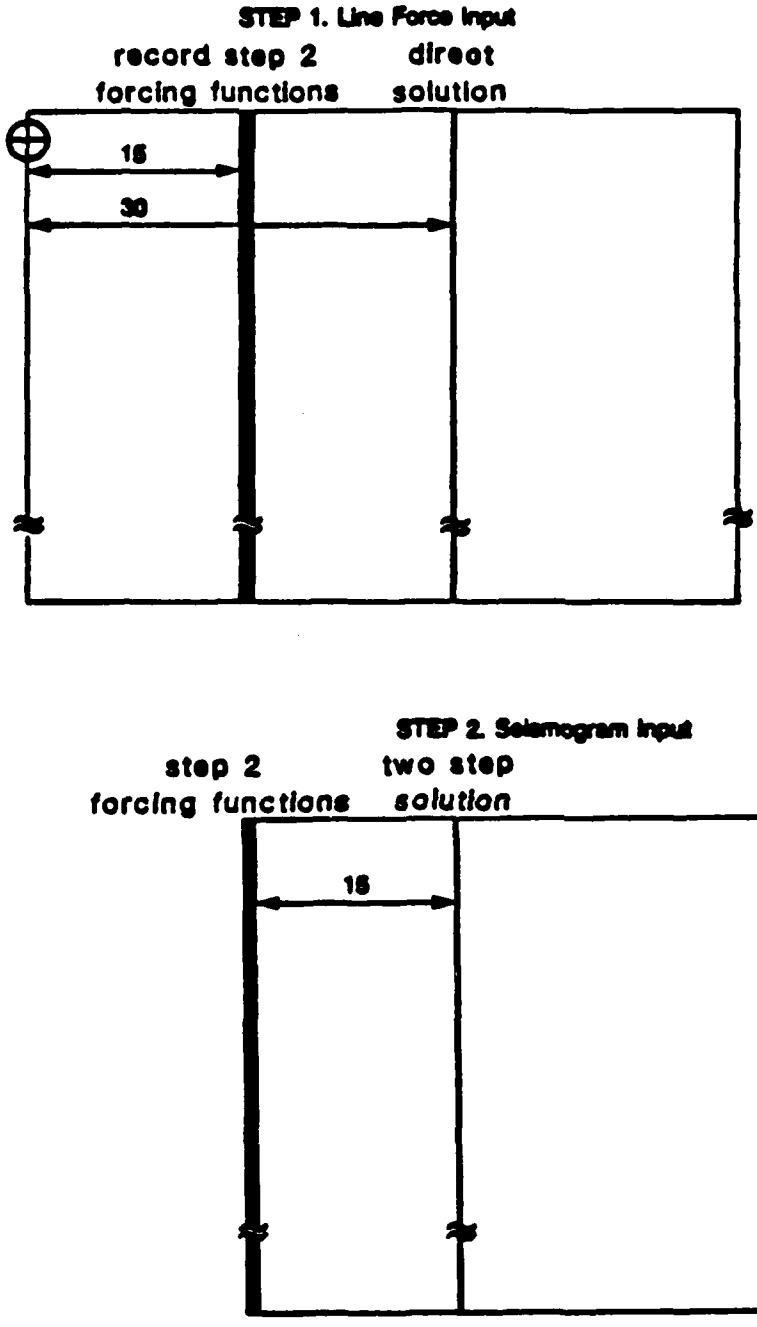

Figure 7: Grids used to test coupling of two successive FE calculations. Both grids are illustrated to scale. The horizontal lines ending in arrows are labeled with the number of element widths they span. The vertical lines within the grids show the locations of the depth sections where results were recorded. The crossed circle on the left side of the first grid represents the line source. Both grids have dimensions 50x50. The horizontal shift of the second grid with respect to the first grid is 15 element widths.

single FE calculation in a fifty by fifty grid are recorded. Figure 7 also shows the spatial relationship of the grid used for the second step of the procedure to the grid used to calculate the direct results and the forcing functions. The first column of nodes in the second grid is shifted to the right to coincide with the location of the sixteenth column of nodes in the first grid. The vertical position of the free surface in each grid is identical. For the second step the intermediate seismograms recorded in step one are used as forcing functions on the first column of nodes in the second grid. The single vertical line within the second grid represents column sixteen, where 'two step' seismograms are recorded. The total propagation distance for the 'two step' procedure, summed over both steps, is equal to the distance propagated in the direct calculation. The application of the displacement time histories used as forcing functions to the left hand edge, or the first column of nodes, of the second grid demonstrates that specifying the the displacements as a function of time due to a given source, for each of the nodes in the leftmost column of a FE grid constrains the motions of all points in the grid to be consistent with that source. When any column other than that closest to the source, in this case the leftmost column, is used as the input column, all nodes more distant from the source than the input column are consistent with the source. The nodes sourceward of the input column form a mirror image of the distant nodes with the symmetry line being the input column. Any energy incident upon the boundary formed by the input column is reflected as it would be from a rigid boundary.

Figure 8 shows a comparison of the seismograms generated by a direct calculation and by the 'two step' procedure. The top seismogram in each column is recorded at the surface. The vertical spacing between the nodes at which the remaining seismograms are recorded is 0.4 km or two element widths, depth increases as one moves down each column. The first column shows the direct results recorded at column

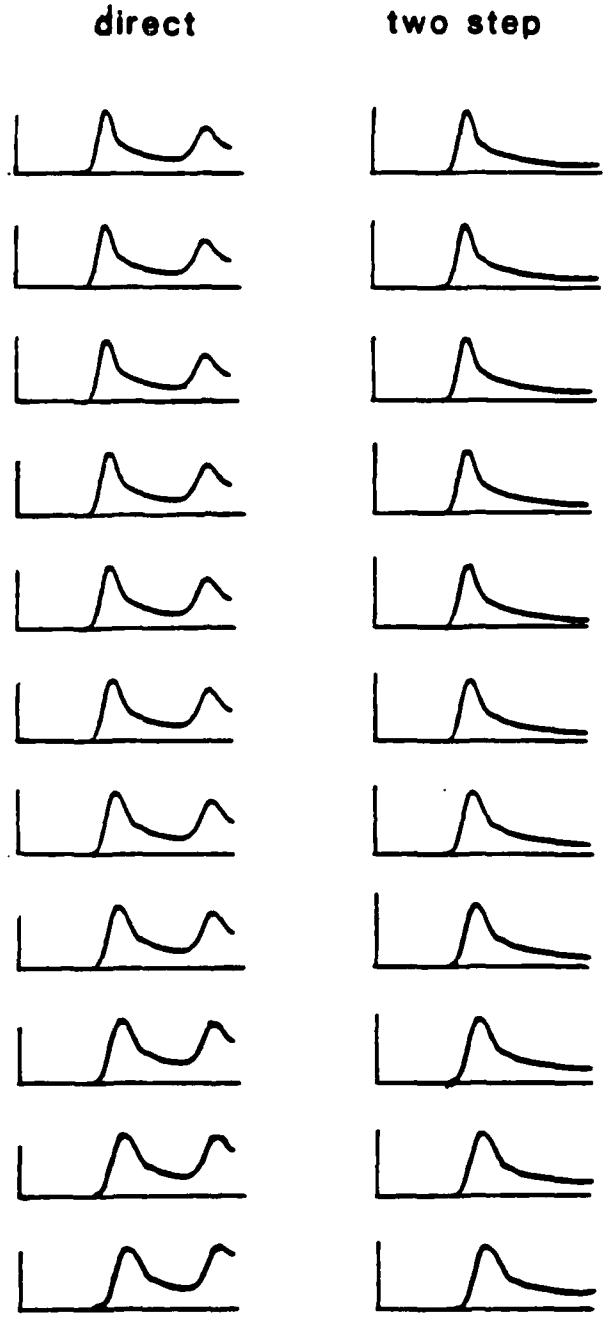

Figure 8: Sample waveforms recorded along the depth section thirty element widths from the source that is illustrated in figure 1.2d. The first column shows the direct seismograms, those recorded in the grid containing the source. The second column shows the two step results recorded at the same distance from the source but in the grid shifted away from the source. The vertical spacing between nodes where seismograms are illustrated is 2 element widths. The uppermost pair of seismograms are recorded at the surface. Depth increases as one moves down each column.

thirty two in the first grid. The second column shows the corresponding 'two step' results recorded at column sixteen of the second grid. The initial waveforms in each column are almost identical, the only discernible difference being a second pulse resulting from reflection from the right hand end of the grid which is seen for the direct calculation only. The reflection is not seen for the 'two step' procedure because the right hand end of the grid is fifteen element widths farther to the right, moving the reflection to a time later than the end of the seismogram. The amplitudes, measured as the height of the first peak, are equivalent. The amplitude variations between methods are less the 0.1%. These results demonstrate the validity of coupling two successive FE calculations by applying forcing functions as BC's on the edge of the second FE grid.

Figure 9 shows the grid geometry used to illustrate how forcing functions can be used to couple energy from a distant source into a FE grid. Seismograms for a line source 2.5 km below the free surface in a half-space, at a horizontal distance of fifteen kilometers from the edge of the grid, were determined using a numerical evaluation of the analytic solution for the direct ray and the ray reflected from the free surface (eq 25). The seismograms form a complete set of forcing functions including a seismogram for each node in the first column of the grid. Analytic seismograms determined by evaluation of the expressions for a line source in a half-space (eq 25) were calculated at horizontal distances from the source corresponding to rows sixteen and thirty-one of the grid. Rows sixteen, thirty one, and forty six are shown in Figure 9 as the three vertical lines within the grid. Using the forcing functions as input to a FE calculation hybrid solutions were calculated for all nodes in columns sixteen and thirty-one. Thus, the analytic solutions can be used as a reference against which the hybrid solutions can be compared.

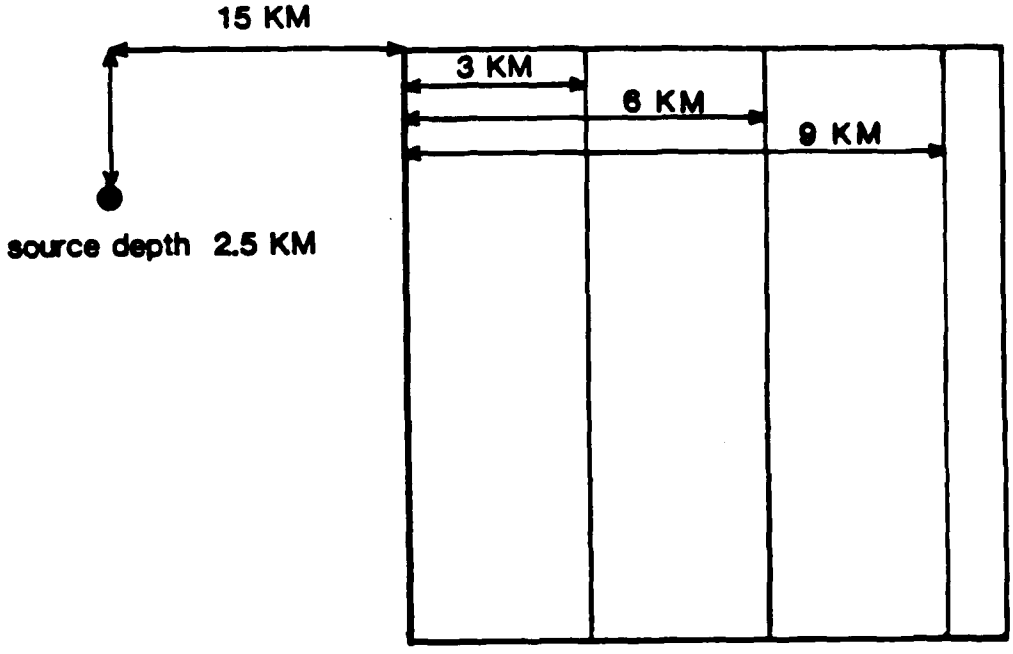

Figure 9: Geometry used to show the validity of coupling energy from a distant source into a FE calculation. The grid illustrated is 50x50 nodes, and is shown to scale. The source is illustrated as the filled circle outside the grid. The source to grid distance is not to scale. The vertical lines in the grid show the depth sections where seismograms were recorded. These seismograms are illustrated in Figure 10 The horizontal lines ending in arrows are labeled with their lengths.

Figure 10 shows the results of the test of the validity of the RT coupling of energy from a distant source into a FE calculation. The first two columns show the results for column sixteen of the grid, which is three kilometers into the grid. The second two columns show analogous results at column thirty two, six kilometers into the grid. The first column in each group shows analytic seismograms for reference. The second column in each group shows the hybrid seismograms at the corresponding locations. The first seismogram in each column is recorded at the free surface. Successive seismograms moving down each column are recorded with one kilometer depth spacing. The waveforms of the analytic and the hybrid results agree extremely well. However, the 'hybrid' results for column thirty two include a reflection from the end boundary of the grid, not present in the analytic calculations. The illustrated seismograms are scaled so that the maximum peak has unit height. Thus, the apparent amplitude differences in the initial peaks at six kilometers is an artifact of the scaling. The correspondence in amplitude between the two methods is excellent. At three kilometers the agreement deteriorates below the fortieth of fifty grid points from better than 0.5% to as much as 10-20%. At six kilometers the departure from the correct amplitudes begins at a shallower depth, after about thirty five grid points. The variations of the quality of fit with distance from the grid edge and with depth from the free surface, can easily be explained. The truncation of the RT integration at the bottom of the grid causes artifacts which are largest as the depth of truncation is approached or surpassed. To be more specific, it is useful to extend the test discussed above to more clearly delineate the nature of these variations, and the restrictions they place on the use of this method of coupling a distant source into a FE calculation. A more extensive test will be discussed below.

To minimize the calculation needed to obtain the forcing functions, it is useful to investigate the effect of reducing the number of forcing functions used, that is limiting

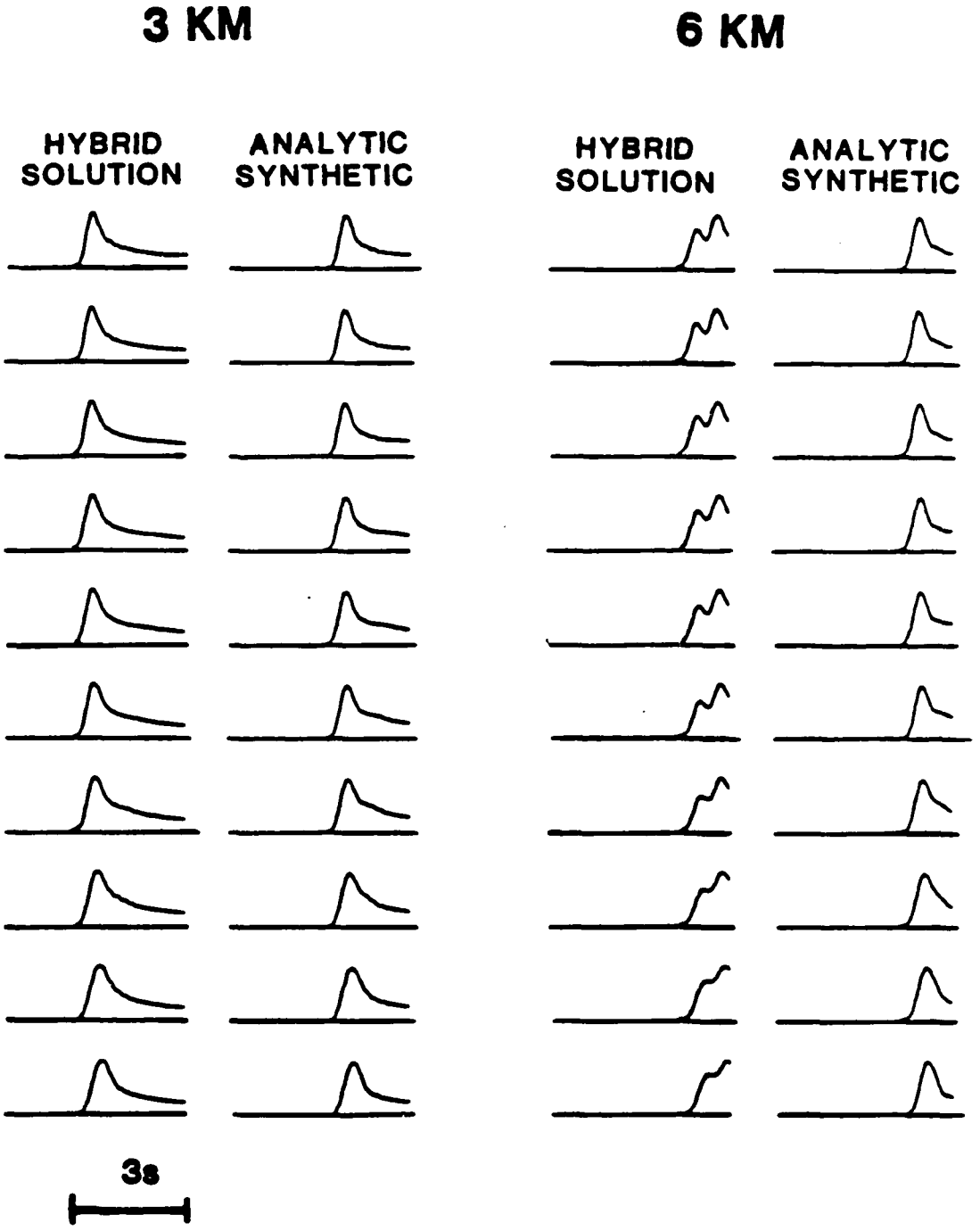

Figure 10: Demonstration of the coupling of a distance source into a FE calculation. Two pairs of columns showing seismograms recorded at the depth sections three and six kilometers from the grid edge. The first column in each pair shows the results of the FE step of the hybrid calculation, the second column shows the half-space synthetics at the same locations. The first row of seismograms are recorded at the surface, successive rows are separated by one kilometer in depth. Peak amplitudes are normalized to one.

the depth extent over which forcing functions are applied to the left hand grid edge. The exact solution of the RT coupling problem requires integration to infinite depth. However, energy arriving after the time of the last sample in the modeled seismogram can be ignored. Thus, the maximum depth which needs to be considered is twice the depth of the deepest receiver plus the distance over which the travel time is equal to the seismogram duration. It is clear that prohibitively large FE grids would be required to produce records of reasonable length or at large distances. However, solution of acceptable accuracy can be produced by integrating over a comparatively small number of forcing functions. The previous example, of coupling energy from a distance source into a FE grid illustrates that this is the case. For a fifty by fifty grid, discrepancies of less than 0.3% for the uppermost forty grid points are observed. A complete solution at the depth of the fortieth row of receivers would require nz to be larger than one hundred fifty, three times the size used in the example. This observation implies that fewer forcing functions are needed if some differences at depth, near the bottom of the grid, are permissible. An experiment to investigate the effects of applying forcing functions to only the top n nodes in the input column has been performed. A geometry and procedure analogous to that used to demonstrate the validity of the RT coupling of a distant source into a FE calculation was used.

The geometry of the grids used to investigate the effects of changing the number of the applied forcing functions and thus, the depth where the deepest forcing function is applied, on the accuracy of the resulting seismograms is shown in Figure 11. A line source embedded in a half-space at a depth of 2.5 km was used and is shown as a large solid dot on the vertical dotted line denoting the x coordinate origin. The horizontal distance from the source to the left hand edge of the grid is fifty kilometers. The first column of nodes in the grids used are shown as a pair of vertical solid lines. The two single solid vertical lines within the grids are the locations where the analytic

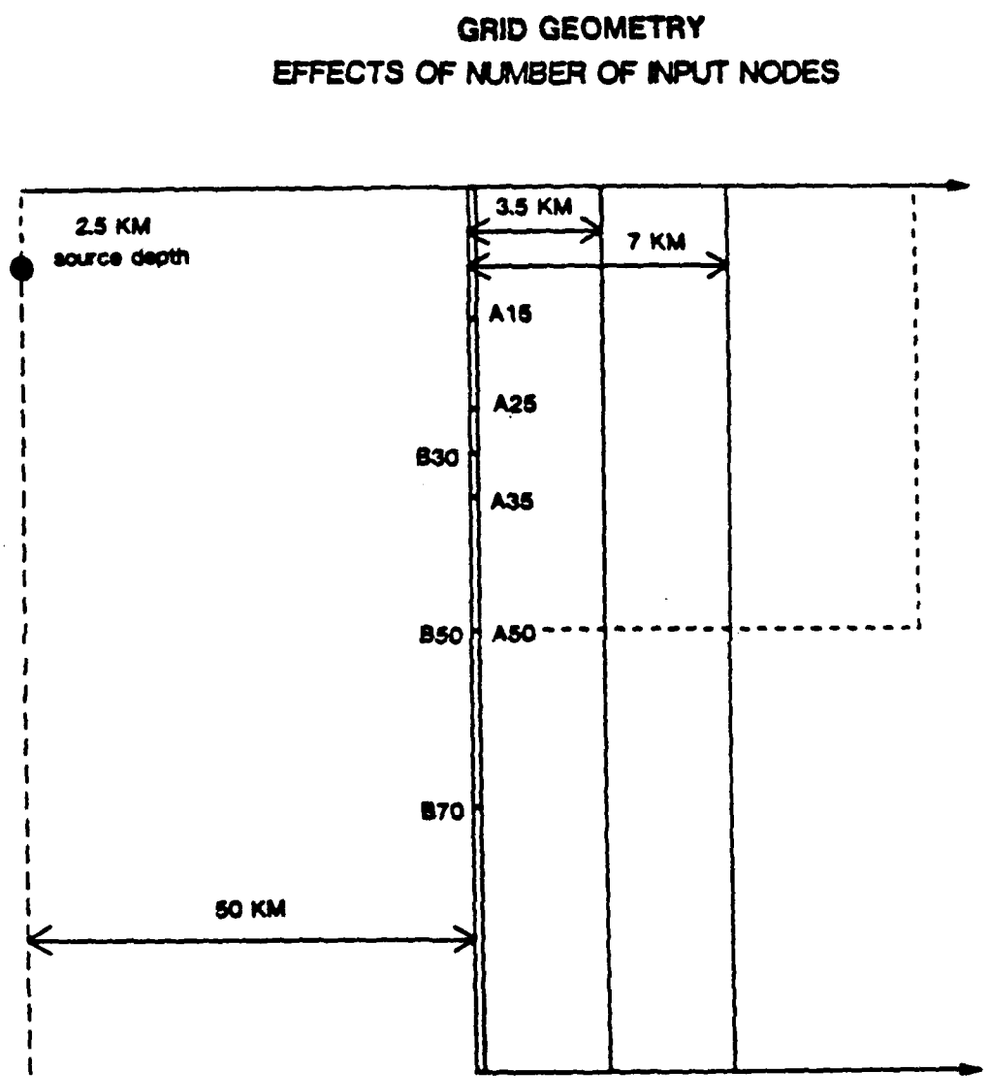

Figure 11: Grids used to test the effect of varying the number of forcing functions. Double vertical lines show the left edge of the grids. Horizontal lines crossing these vertical lines show the bottommost forcing function for each test. Tests A15, A25, A35, and A50 are completed in the 50x50 grid whose extent is marked by the dotted boundaries. Tests B30, B50, B70, and B100 are done in the large grid whose bottom is shown as a horizontal line ending in a solid arrow. The solid vertical lines within the grid show the depth sections where results are recorded. Solid horizontal lines ending in arrows are labeled with their lengths.

synthetic seismograms are compared with the hybrid seismograms from the FE calculations. They are at distances of 53.5 km and 57.0 km from the source, corresponding to columns sixteen and thirty one in the FE grids. Two grids are used for these tests. The dotted lines within the large 100x100 grid are the bottom and right hand edges of the smaller fifty by fifty grid used for the first four tests. The solid horizontal lines ending in solid arrows show the free surface and the bottom edge of the large FE grid used for the remaining tests. For both FE grids hybrid seismograms were calculated for four cases. Each of these cases used a different number of forcing functions. For the small FE grid fifteen, twenty five, thirty five, or fifty forcing functions were used. For the large FE grid thirty, fifty, seventy, or one hundred forcing functions were used. The vertical extents of the input forcing functions are illustrated to scale in Figure 11. The locations of the bottommost input forcing function for the small grid tests are shown by the horizontal lines labeled A15, A25, A35, and A50 which cross the first column of elements in the illustrated grid. For the large grid the bottommost forcing functions are shown as the lines labeled B30, B50, B70, and the bottom of the large grid, B100. Results from each of these eight tests were examined to determine the effects of grid size and vertical extent of the input forcing functions.

Figure 12 shows examples of the seismograms observed at column sixteen in the four small grid tests. The surface seismograms are illustrated in the first row of the figure. Each row is recorded at nodes about 0.9 km deeper, that is four element widths deeper than the previous row. The column of numbers in the middle of the figure give the node row at which that row of seismograms was recorded. The first column shows results from test A50. These waveforms are very similar to the analytic seismograms recorded for the same locations. The agreement is best at the surface, at depths below the thirty fifth node the decay of the pulse becomes less rapid than that seen on the analytic synthetic and the maximum amplitude of the pulse increases with

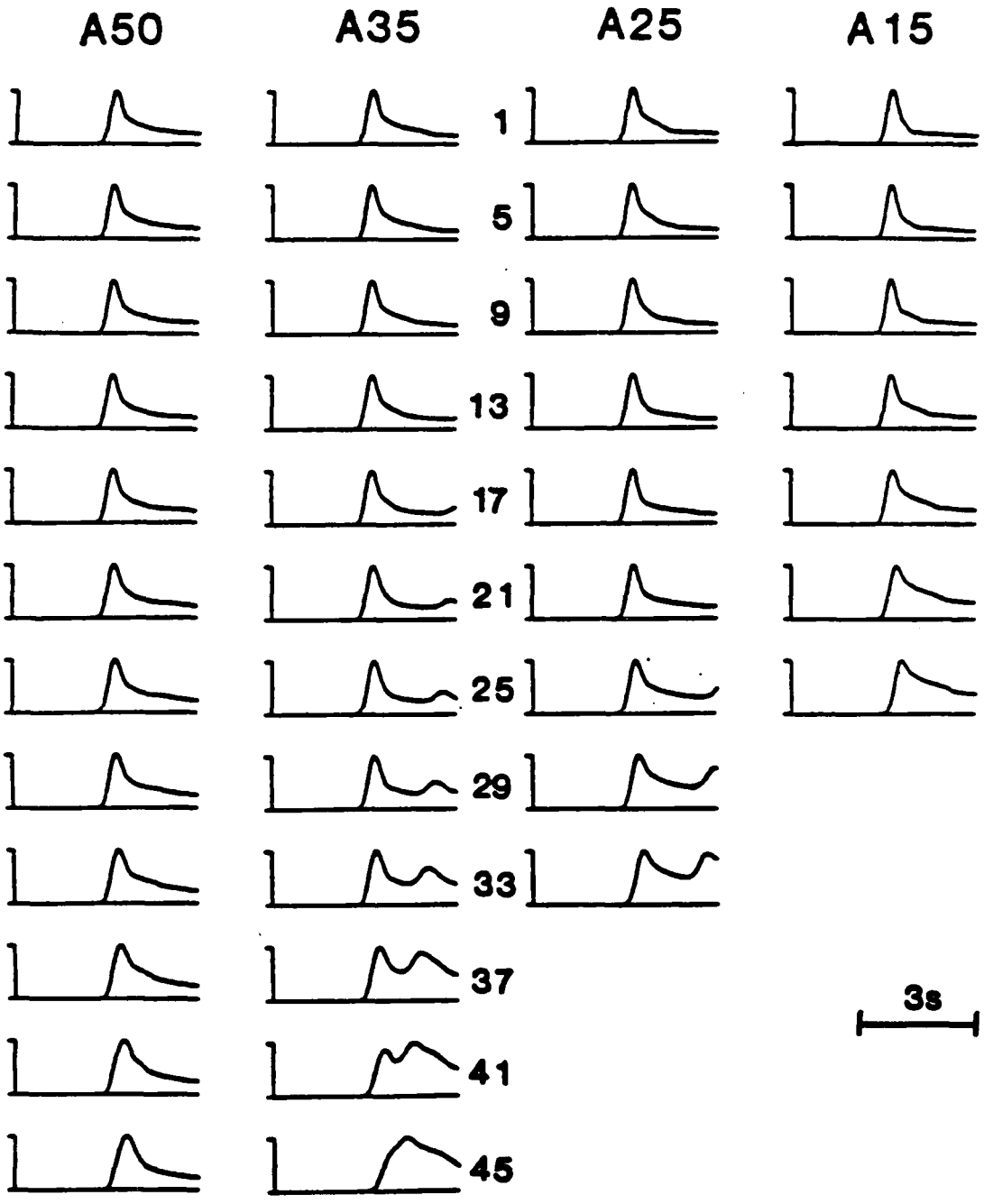

Figure 12: Seismograms for four cases using different numbers of forcing functions. Each column shows seismograms on a depth section at 53.5 km from the source. The first row is recorded at the surface. Vertical spacing between rows is about 0.9 km. The first column uses 50 forcing functions, the second 35, the third 25, and the fourth 15. The column of numbers in the center of the figure gives the node row number for each row of seismograms.

respect to the analytic synthetic. For this test the difference in waveform shape is small. The second column shows results from test A35. A second pulse not visible for the A50 test is present. This pulse is a reflection from the grid bottom of energy not canceled by the disturbances input in the bottommost fifteen forcing functions in test A50. The pulse is most prominent for traces recorded at depths below the bottommost forcing function applied in this test. This is predictable since it could not be expected that results for receivers below the input nodes would be reliable. If the reflection can be removed, as with an absorbing BC then the correspondence of A35 results to direct synthetics is good down to node row thirty or thirty five. The third column shows results of test A25. Again a reflected pulse contaminates the deeper receivers. Results compare well with the analytic synthetics down to about node row twenty. The fourth column shows results of test A15. Here, the same trend already observed continues. The correspondence between A15 results and analytic synthetics is good down to about node row ten. It appears that acceptable waveforms can be calculated for depths such that at least five to ten input forcing functions are applied at rows below the receiver. Similar results are observed for these tests at seven kilometers from the grid edge, and for the large grid tests at both distances. Some indication that calculation of accurate seismograms at longer distances may require a larger vertical extent of input forcing functions has been observed.

Figure 13 gives a more complete analysis of the amplitudes of the seismograms recorded in these eight tests in relation to the amplitudes of analytic synthetics. At both distances the maximum amplitudes of the seismograms from each test were tabulated. These amplitudes were used to calculate amplitude ratios. The amplitude ratio, A, is defined as

$$A(\text{node i}) = \frac{\text{AMPLITUDE OF DEPTH EXTENT TEST (node i)}}{\text{AMPLITUDE OF DIRECT CALCULATION (node i)}} \qquad (47)$$

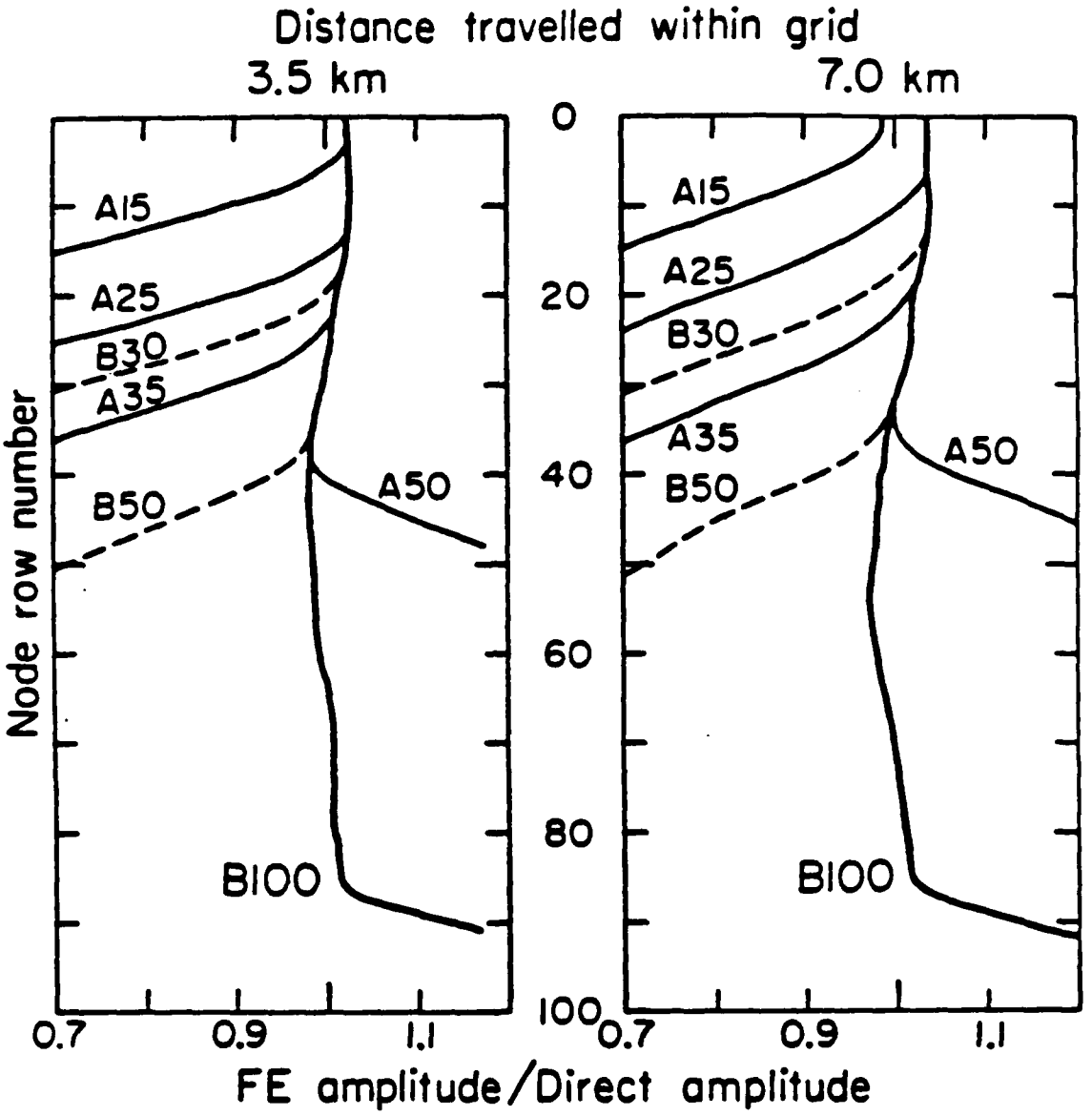

Figure 13: Relative amplitudes of synthetic and two step seismograms at the same locations, as a function of the number of input forcing functions. The left hand graph shows results recorded at a depth section 3.5 km from the grid edge, the right hand graph results recorded at 7 km. Heavy lines show tests for which all node rows in the grid have forcing functions applied. Lighter solid lines show results of tests in the 50x50 grid. Dotted line show result of tests in the 100x100 grid. The number in the label above each line indicated the number of forcing functions used in that test.

These amplitude ratios were then plotted as a function of depth, measured as a number of node rows. The resulting plots are shown in Figure 13. The left hand plot is for a distance of 3.5 km, and the right hand plot for a distance of seven kilometers. The heavy lines in each plot indicate the amplitude ratios for the two tests in which all nodes in column one of the grid have forcing functions applied to them, A50 and B100. These tests are used as a reference against which the other tests can be compared. The dotted lines labeled A15, A25, and A35 show where the amplitude ratios for the three tests in the small grid, using partial sets of forcing function input, depart from those of test A50. The amplitude ratios agree well with those of the A50 test for the near surface nodes in each test. The depth at which they depart from the A50 results increases as the number of input forcing functions increases. As expected the amplitude correspondence is better when more complete input is used. Examining these results at a distance of 3.5 km shows that if results for n rows are desired, input forcing functions should be applied to n+5 nodes. At seven kilometers similar results are observed but the departure from acceptable amplitude ratios occurs four or five nodes shallower. Thus, as distance increases a larger depth extent of input forcing functions is needed to produce amplitude correspondence within acceptable bounds. The results for the tests using the larger grid are show in Figure 13 as the light lines labeled B30 and B50. The results show the same trends as the results for the small grid indicating that the artifacts in the tests using truncated input sets are due to interaction with the grid bottom of incompletely integrated signals in the seismograms.

If one wishes the analytic solutions to correspond well to the FE solutions the frequency content of the forcing functions used to drive the FE calculation becomes important. To investigate the effects of the frequency content of the input, sets of forcing functions for a source distant from the FE grid were calculated for two cases.

Each of these sets consists of seismograms calculated along a depth section fifty kilometers from the source, with a vertical node spacing of 0.2 km. Both sets of seismograms were determined for a line source, with a triangular time function, in a half-space (eq 25). The first case used a time function with a duration of .15 seconds, the second used a time function with a duration of .45 seconds.

The results of these tests are illustrated in Figures 14 15, and 16. The first two of these figures show the seismograms recorded on a depth section 53.5 km from the source. The vertical spacing between successive rows of seismograms is about one kilometer. The amplitudes in all traces in these figures have been normalized such that the peak amplitudes of each trace appear the same size. The first column in each figure shows the analytic solutions. The second column shows the same seismograms band pass filtered between one and one hundred seconds. The third column shows the bandpass filtered hybrid solutions. Figure 14 shows the results using the 0.15s time function, and Figure 15 shows the results for the 0.45s time function. Figure 16 addresses the amplitude correspondence for both cases. In Figure 14 it is possible to see both the direct arrival and the arrival reflected from the free surface in the direct seismograms recorded at depth. These arrivals are clearly higher frequency than the minimum period of one second transmittable by the FE grid. The hybrid solutions for this case contain unwanted oscillations. However, when the hybrid solutions, and the direct solutions are both band pass filtered their waveforms are in excellent agreement. Alternatively, band pass filtering the forcing functions before they are input to the FE calculation will produce unfiltered hybrid solutions almost indistinguishable from the filtered hybrid solutions calculated using the unfiltered forcing functions. Aliasing of energy traveling in waves of frequency higher than can be propagated by the grid into lower frequency bands does not seem to be a problem for these tests. Figure 15 shows that waveforms of the direct and hybrid solutions correspond well when the input has

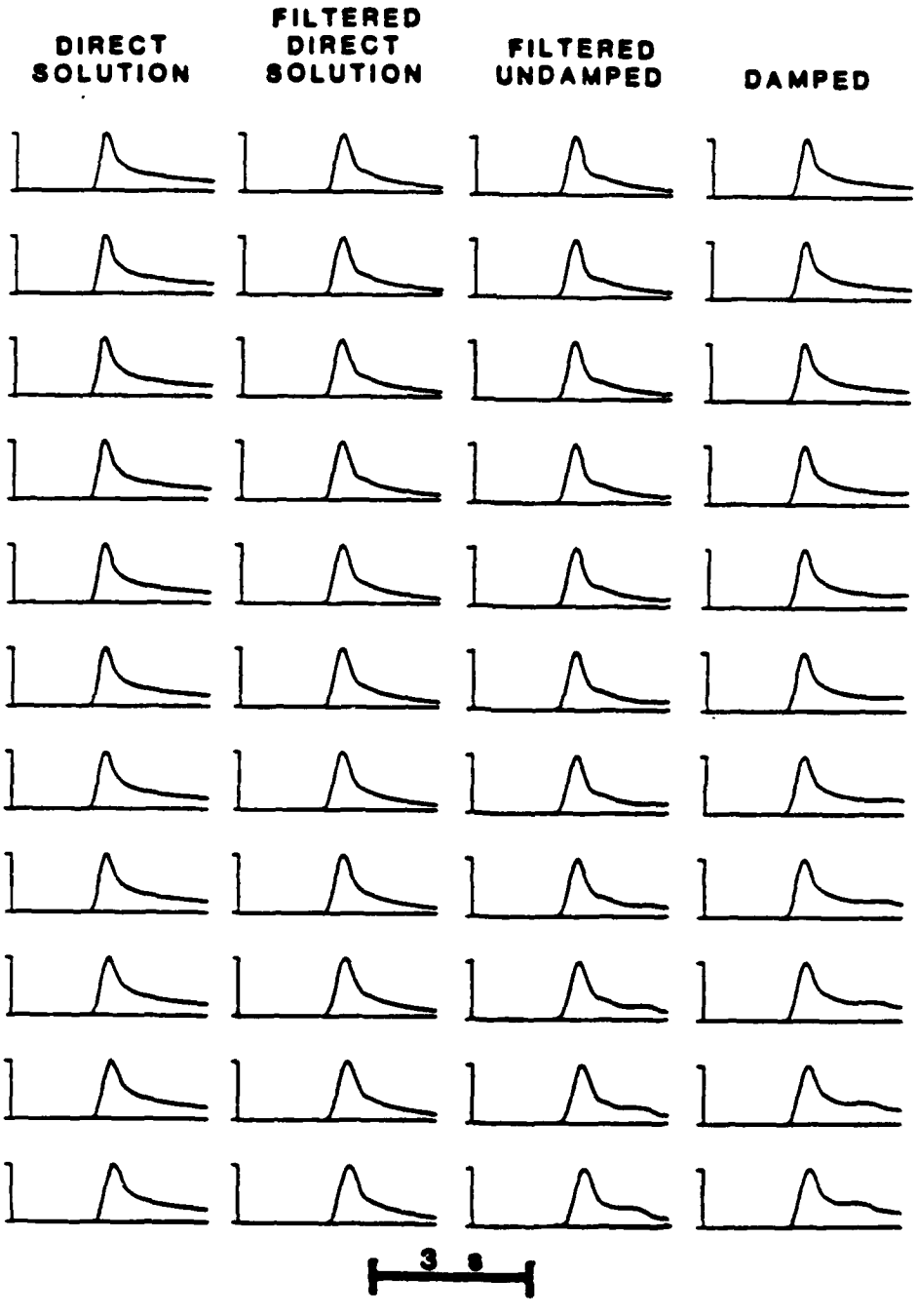

Figure 14: Effects of filtering and internal damping on FE solutions. Column one shows a depth section of line source half-space synthetics with a triangular time function of .15s duration. Column two shows the same seismograms band pass filtered between 1s and 100s period. Column three shows the hybrid solutions without internal damping and with the same bandpass filter applied. The fourth column shows the hybrid solution with internal damping. No filter is applied. Amplitudes of each trace are normalized to give unit peak amplitude.

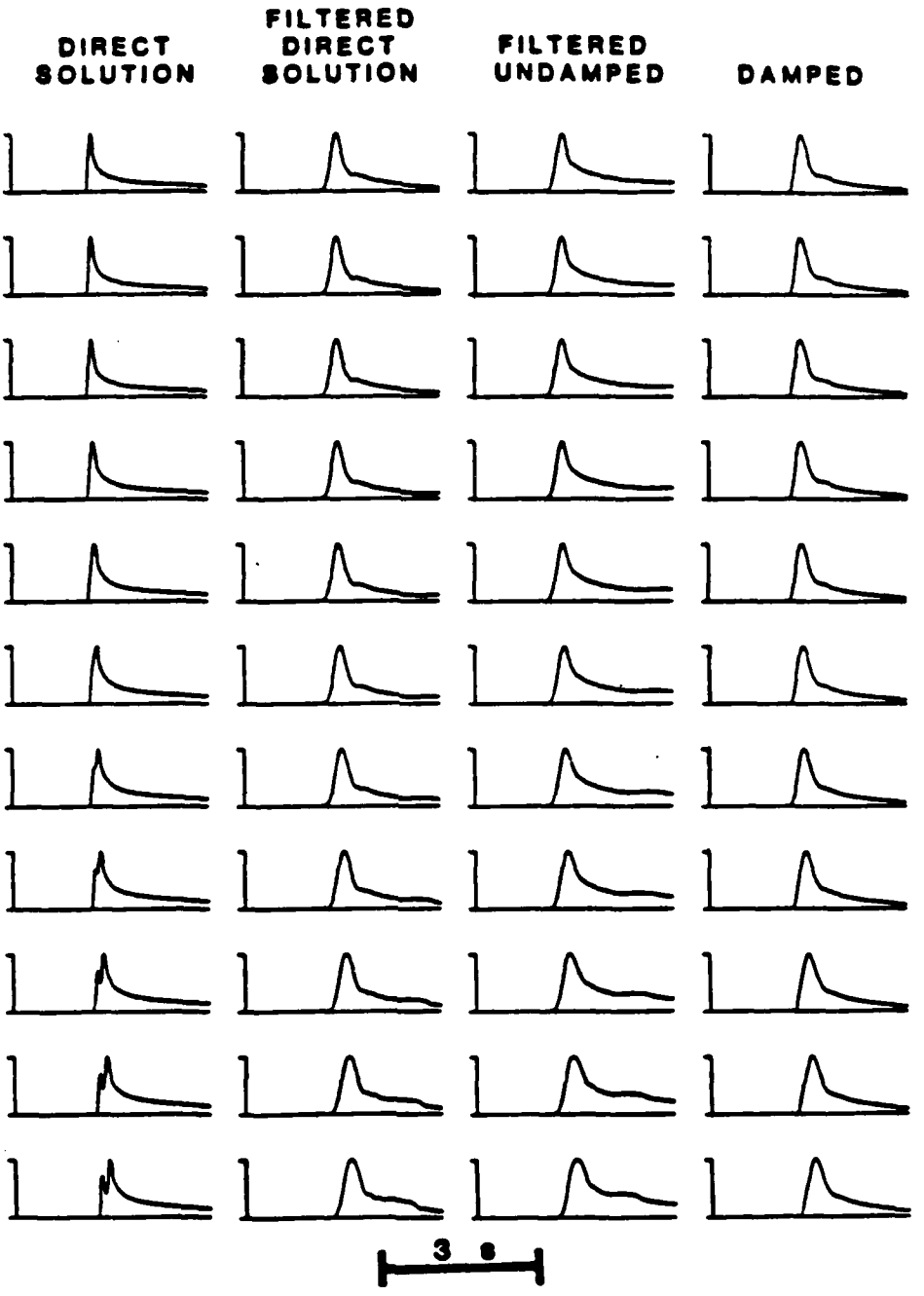

Figure 15: Effects of filtering and internal damping on FE solutions. As for figure 14 but using a triangular time function of .45s duration.

no significant high frequency component. In this case the bandpass filtering makes little or no additional improvement to the correspondence of the two sets of results.

The spurious oscillations seen in the unfiltered hybrid solutions can be removed by filtering as discussed above, or by the introduction of a damping coefficient within the FE calculations. For each of the sets of forcing functions used in the tests discussed in the previous paragraph FE solutions were determined both with and without damping. The damping coefficient used in the FE code is dependent on distance. Therefore, a single damping coefficient cannot produce correct amplitudes at a variety of distances. At the distance for which the coefficient is calculated, and within a few grid spacings of that distance, the coefficient produces FE results that correspond very well with the direct solution. If the direct solution contains high frequencies the results correspond to the filtered direct results. This can be seen by examining Figures 14 and 15. In each of these figures column two shows the filtered direct solutions, and column four shows the hybrid solution using internal damping with the FE calculation. The damping coefficient is chosen to be optimal at the illustrated distance. The correspondence in waveform between these two columns is very good.

Figure 16 shows the amplitude ratios for the tests of filtering and damping efficiency. It illustrates the relative accuracy of using the damped FE and the filtered undamped FE approaches. The damped FE calculation shows more variation with depth of the amplitude ratios. The ratios are calculated at the distance for which the damping coefficient was optimal. However, for the calculation which includes damping, as distance from this point increases the amplitude ratios rapidly depart from one and show even larger variations with depth. On the other hand the ratios for the filtered undamped FE calculation remain quite stable.

The results of these tests can be summarized by noting the following important observations. If the input seismograms contain frequencies higher than those that can

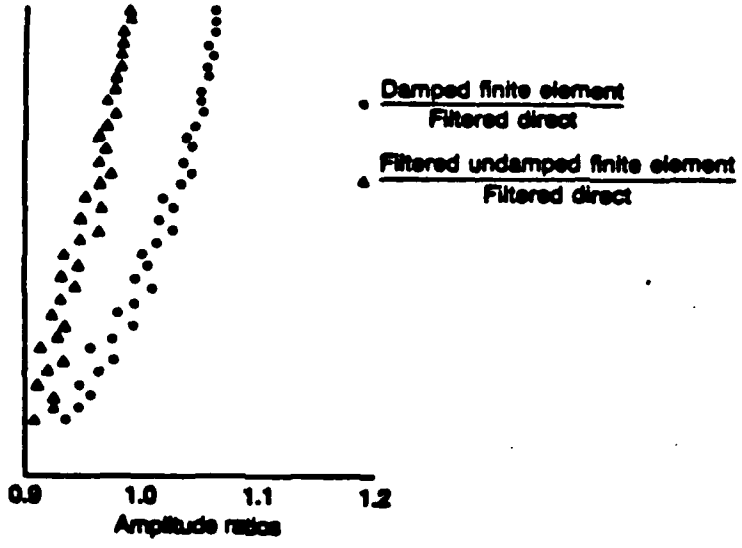

Figure 16: Amplitude ratios as a function of depth for seismograms recorded on a depth section 57 km from the source.

be propagated through the FE grid, as in the case of the rapid rise observed for the forcing functions and analytic seismograms with the 0.15s time function, then the grid acts as a filter. The amplitude of the FE solutions are significantly reduced with respect to the analytic solutions and spurious oscillations are introduced near the end of the waveform. The correspondence of amplitudes and waveforms between the analytic solution and the hybrid solution for this situation is poor because the analytic solution contains higher frequencies than the hybrid solution, and the hybrid solution contains numerical artifacts. Low pass filtering the analytic solution and the hybrid solution will improve the waveform fit enormously, and bring the amplitude ratios much closer to one. The cutoff frequency of the low pass filter should be at most the highest frequency that the grid can propagate. It is not important whether the input forcing functions or the output hybrid solutions are filtered. Both approaches produce equivalent results. When input forcing functions contain no frequencies too high for propagation, filtering of hybrid solutions or analytic synthetics is not necessary as it does not change the goodness of fit. The use of internal damping in the FE calculation is distance dependent and introduces addition variation in the goodness of fit of amplitude and waveform as a function of depth. Considering all these observations the best combination of filtering and damping when a range of distances is to be used is to filter an undamped FE solution. If theoretical results are available the filtered undamped solutions should be compared directly to them. If the theoretical results contain high frequencies they should be low pass filtered before being compared to the filtered undamped solutions. This approach should give the best correspondence to the theoretical results.

Tests of Accuracy: SH Lg Mode Sum Input

The accuracy of coupling a 2-D SH pulse from a source outside a FE grid into that grid have now been thoroughly discussed. The limitations of such an approach

have also been defined. However, generalizing these results, which have been demonstrated only for a line source in a half-space, to a line source or a point source in a layered media or even in a layer over a half-space can be misleading. Some of the tests discussed below illustrate cases for which results do not generalize. The physical model used in all of these tests is a layer over a half-space. The addition of the layer above the half-space allows for the existence of Love waves. This changes the behavior of the accuracy of coupling a distant source to a FE calculation. In these tests the layer has a thickness of thirty two kilometers, an S wave velocity of 3.5 km/s, and a density of 2.7 g/cc. The underlying half-space has an S wave velocity of 4.5 km/s, and a density of 3.5 g/cc. The initial calculation demonstrating the validity of coupling a distant source into a FE grid for the case of a layer over a half-space used a grid spacing of 0.53 km in both x and z. All subsequent tests used a grid spacing of 0.5 km in both x and z. All tests use a time step of 0.05 s. Each test uses the same set of ninety forcing functions, or a subset of that same set, applied to the leftmost column of nodes. Forcing functions are calculated for a strike slip point double couple source at a depth of eight kilometers. The source to grid edge horizontal distance is 1500 km.

The seismograms used as forcing functions in the tests discussed below are calculated as mode sums over modes with periods between 0.5 s and 100 s. The fundamental mode and the first five higher modes are included in each calculation. This is not a complete representation, but produces a seismogram that shows the overall character of the arrivals seen in data in the L_g group velocity range of between 2.8 and 3.5 km/s. A complete representation would require as much as five times the amount of calculation to produce the forcing functions or the synthetics used for comparison to the hybrid results. To assure the inclusion of all energy down to a period of 0.5 s twenty two higher modes would be necessary, for all energy down to a period of one

second eleven higher modes need to be included. The cutoff frequency of the sixth higher mode is 1.9 s. The forcing functions used are complete to that period and contain a significant portion of the energy at the shorter periods considered. For waveform modeling of data the use of a more complete mode set would be advisable, but for the tests discussed here it is an unnecessary expenditure of effort. An example of a forcing function or direct seismogram, recorded at the surface at a distance of 1500 km from the source is shown in Figure 17. The group velocities of the arrivals are shown along the horizontal axis. The heavy rectangle enclosing the largest portion of the seismogram delimits the portion of the trace used as a displacement time history to drive the surface node on the depth section at 1500 km from the source. The seismogram shown in this figure is not the actual trace used as a forcing function. It has been band pass filtered between 0.01 and 1.0 Hz and has had the WWSSN short period receiver function applied to it. The traces used as forcing functions have been band pass filtered but do not have the instrument applied. Examples of such traces at different source receiver separations are shown in Figure 18. In this figure these traces are labeled synthetic.

At this point it is useful to digress and to more precisely define the RMS amplitude measure used in subsequent discussions and the method used to calculate it. The form of the relation used to determine the RMS amplitude is

$$RMS = \frac{\sqrt{\sum_{n=1}^{m} \left[amp(n)^2 \right]}}{\sqrt{m}} \qquad m = \frac{T_{RMS}}{\Delta t} \tag{48}$$

where m is the number of points in a sampling window or duration T_{RMS} seconds. The location of the sampling window with respect to the arrivals of maximum amplitude and the duration of the trace contained within the sampling window have a significant effect on the value of the RMS amplitude. Care must be taken to choose

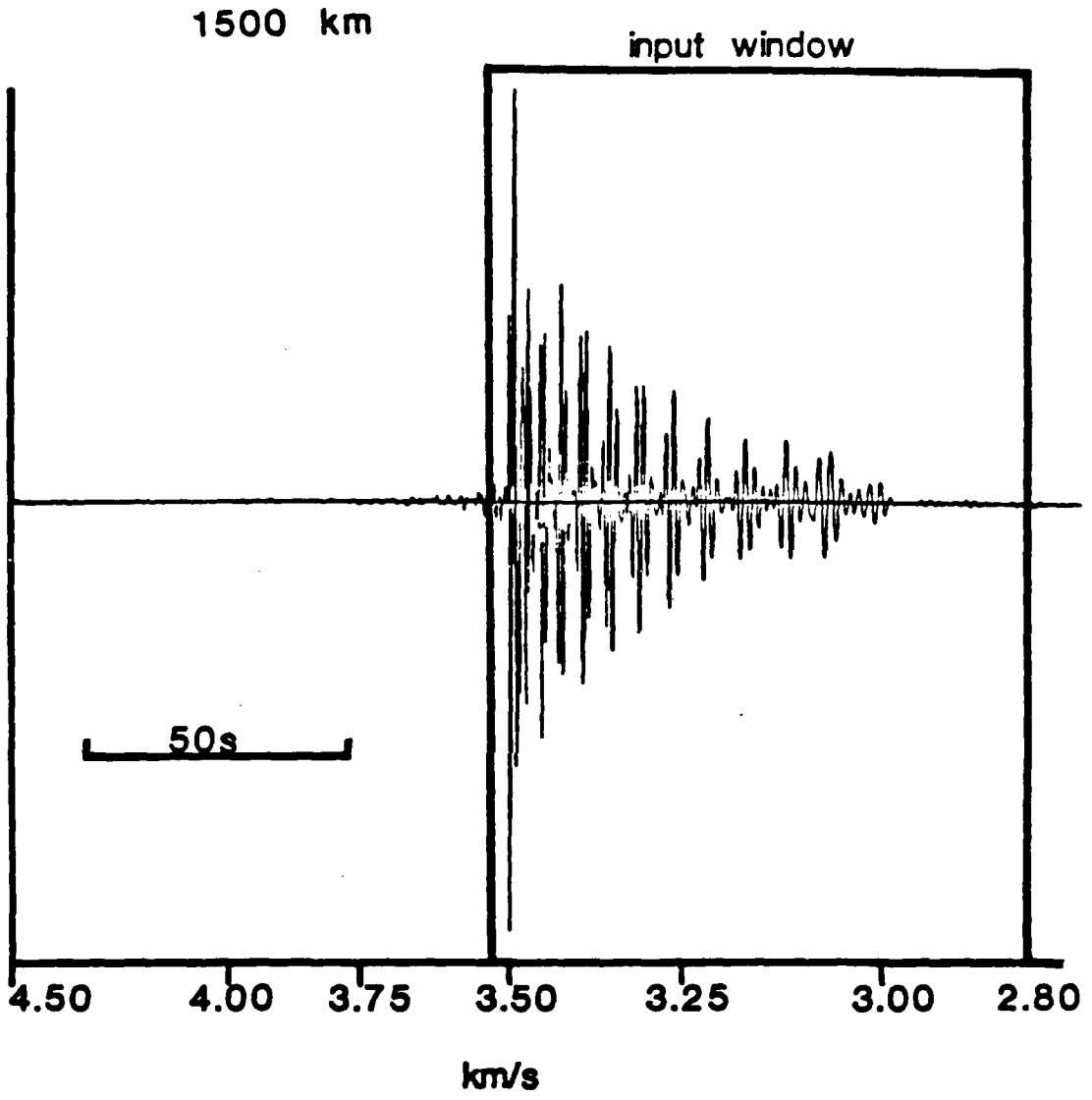

Figure 17: Sample forcing function for SH L_g wave FE calculation. The seismogram includes modes with periods between 0.5s and 1000s. Only the fundamental and the first five higher modes are used. The mode sum synthetic has been transmitted 1500 km from the source using the propagator matrix technique. The resulting seismogram has been band pass filtered between 0.01 and 1 hz, and has the WWSSN short period instrument has been convolved with it. The portion of the seismogram within the box labeled input window is used as a forcing function. The numbers along the axis indicate the group velocities of the arrivals.

windows for two sets of results that are compatible with each other and produce meaningful comparisons. For example, choosing the beginning of the seismogram being considered as the first point in the sampling window can cause difficulties when comparing different calculations or when comparing successive seismograms along a depth or distance section. When different calculations are being compared extreme care must be taken to insure that both seismograms begin at the same absolute time. When successive seismograms in a depth or distance section are being compared, the duration of the portion of the trace with negligible amplitude that occurs before the first arrival increases with distance from the source. This creates an artifact that makes RMS amplitudes appear to decrease with distance. To avoid these and other problems some other method of determining the beginning of the sampling window must be devised. It would be possible to correct for the distance term by ignoring enough points at the beginning of the seismogram to compensate for the difference in arrival time. However, when models became more complicated the choice of the first arrival, and the determination of its travel time from the source becomes more complicated due to the possible presence of strong refracted or diffracted phases. Thus, a more general approach which does not require the use of theoretical travel times has been chosen. Two different methods of selecting the first point in the sampling window have been used. The selection of one of these two methods was based on the characteristics of the waveform as discussed below.

The first method, which was used in the majority of cases, selects the first point to be included in the sampling window and the last point to be included in the seismogram by bracketing the portion of the seismogram whose RMS amplitude is to be measured. This piece of the seismogram is bracketed with sections of seismogram with sustained low amplitude persisting for at least a defined minimum duration. This method is used when the oscillations in the waveform are very small until the first

large and impulsive arrival occurs, when no periods of sustained low amplitude occur during the duration of the trace, and when the amplitude of the seismogram decays to a sustained low amplitude at its end. Given that all three of these conditions are satisfied the following algorithm produces stable and accurate RMS amplitude measures. The algorithm consists of five steps:

(1) Determine the size of the maximum absolute value of amplitude in the seismogram

(2) Set a cutoff value for the amplitude at some fraction of the maximum (usually .01 or .05)

(3) Beginning at the location of the maximum absolute value scan toward the beginning of the seismogram until a series of samples two seconds in duration all have amplitudes smaller than the cutoff amplitude. The first point in this series is defined to be the first point in the sampling window used to determine the RMS amplitude.

(4) Beginning at the location of the maximum absolute value scan toward the end of the seismogram until a series of samples two seconds in duration all have amplitudes less than the cutoff amplitude. The first sample in that series of samples defines the last point in the seismogram.

(5) Calculate the RMS amplitude for sampling windows with durations 15, 20, 25, .., 85s. If the duration of the sampling window exceeds the duration of the seismogram then the longest sampling window used is the duration of the seismogram, and that duration is recorded.

The second method is used when small arrivals precede the main arrival on only a subset of the traces being considered, when the small arrivals preceding the main arrival contain sustained periods of low amplitude on some subset of the traces, and when sustained periods of low amplitude occur elsewhere within any of the

seismograms. This method is not used when the arrival with maximum absolute amplitude is preceded by a lower amplitude arrival of long (>10s) duration, or when the maximum amplitude occurs within the first 10s of the seismogram. This method is also useful when slight wraparound occurs as a result of convolving the instrument with the seismogram producing small spurious arrivals before the main peak. If significant wraparound occurs, the convolution length is extended to remove it. The determination of RMS amplitude is not expected to correct it. The basics for the algorithm used for the second method are identical to those used in the first method. The only differences lie in the method used to select the first point in the sampling window, and in the duration (5s) of sustained low amplitude that defines the end of the seismogram. When using the second method the first point in the sampling window is defined to be the point in the time series for a time ten seconds before the time of the peak of maximum absolute amplitude. Clearly, if the maximum amplitude occurs late in the seismogram this method is not useful. However, when periods of sustained low amplitude occur early in the seismogram, or when small amplitude early arrivals are detected on only a subset of the seismograms then this method gives stable RMS amplitudes whereas the amplitudes using the first method will not be stable.

These algorithms yield a series of RMS amplitude values that can be used to compare results derived using different methods. If RMS amplitudes agree within all period ranges, and waveforms are similar the fit is considered to be excellent. If discrepancies occur or increase with the length of the sample window, then there is probably a problem modeling the later arrivals, that is, the representation of later arrivals is probably incomplete. If the shortest time windows show discrepancies that decrease rapidly as the window length increases then the amplitudes of the initial arrivals are unstable or incorrect. Examining the behavior of the RMS amplitude as a function of sample window length can give insight into the nature of and the

underlying reasons for misfit between methods. In most of the discussions that follow, the method used to obtain RMS amplitudes will not be specified. Both methods described above give consistent interpretations if they are applied to all seismograms in a given example. While the actual amplitude measures may vary between the two methods the changes seen in amplitude within a given example are the same regardless of the method used so long as the same method is consistently applied. The variation of RMS amplitude with the length of the sample window will be discussed only when such variation have direct impact upon the results of the comparisons.

Now I will return to the discussion of the RT coupling of a distant line source in a model consisting of a layer over a half-space into a FE calculation. First, it is useful to establish that the coupling of energy from a distant source into a FE grid is valid for a layered structure more complicated than a half-space. The seismograms illustrated in Figures 18 and 19 verify that the method of coupling does generalize as the theory implies it should. The seismograms in Figure 18 are recorded at two distances from the grid edge, and at five depths for each of these distances. A pair of seismograms is shown for each of these ten locations. The upper seismogram in each pair is the direct synthetic determined as a mode sum and transmitted to the receiver using the propagator technique. The lower seismogram in each pair is the hybrid synthetic for which the first portion of the path is traversed using the propagator matrix technique and the remainder of the path is traversed in a FE grid. For this test a 100x100 node grid was used and sixty forcing functions were applied to the FE grid edge. All seismograms in Figure 18 have a duration of fifty five seconds and have been band pass filtered between .01 and 1 Hz. The amplitudes of all traces are normalized so the maximum peak to peak amplitude of each trace appears to have the same value. Within each pair the variation in peak to peak amplitude is less than five percent. The peak to peak amplitude ratios of the hybrid synthetic to the analytic synthetic

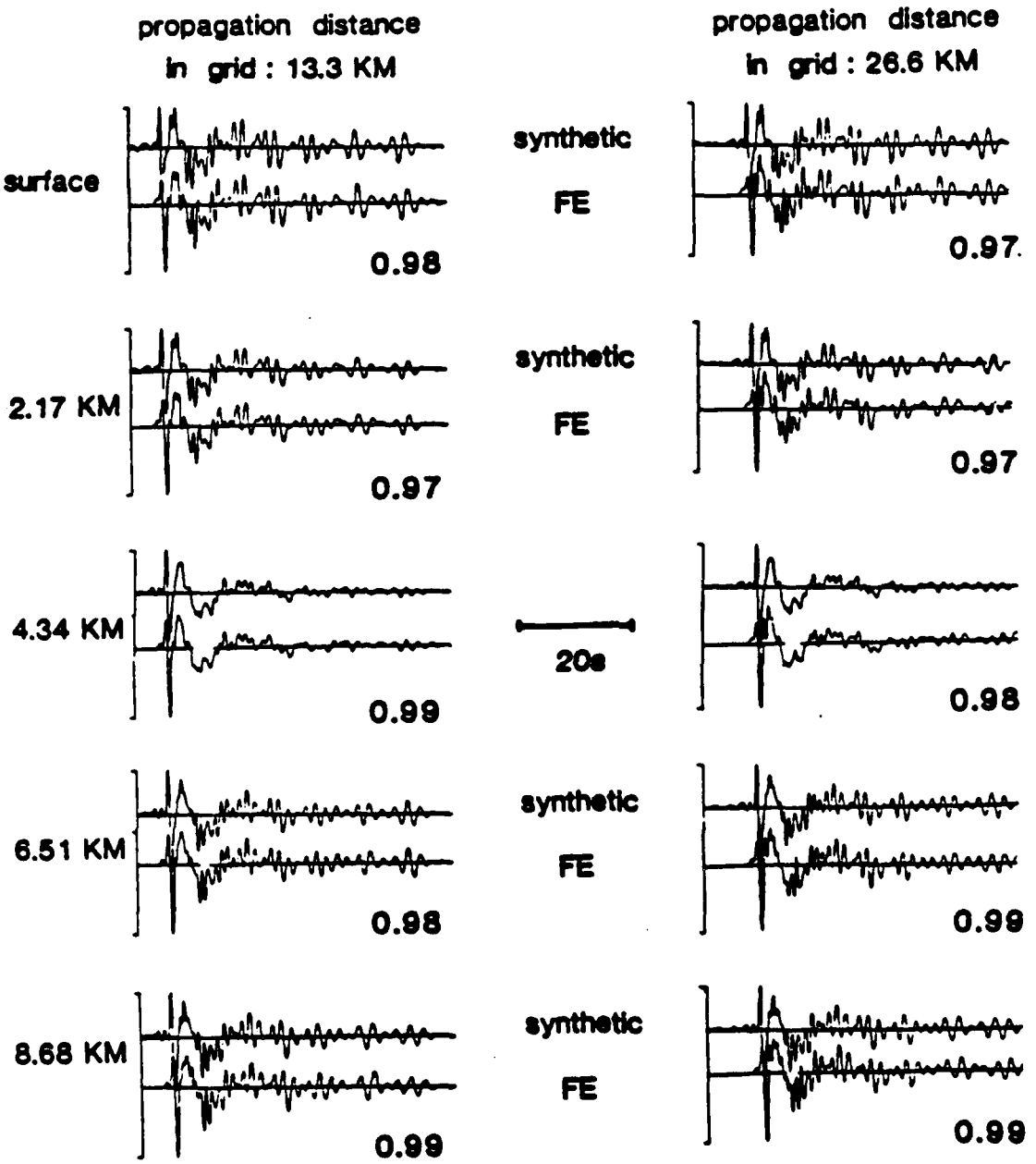

Figure 18: Comparison of hybrid solution to mode sum synthetics. The upper trace in each pair is a mode sum synthetic transmitted using only propagator matrices. The lower seismogram in each pair is the hybrid solution. The depths for each row and the horizontal propagation distances in the FE grid for each column are shown. The ratio of the FE to synthetic peak to peak amplitudes is given as the number below each pair of traces. Each trace has been band pass filtered between .01 and 1.0 Hz, and its maximum peak to peak excursion has been normalized to one.

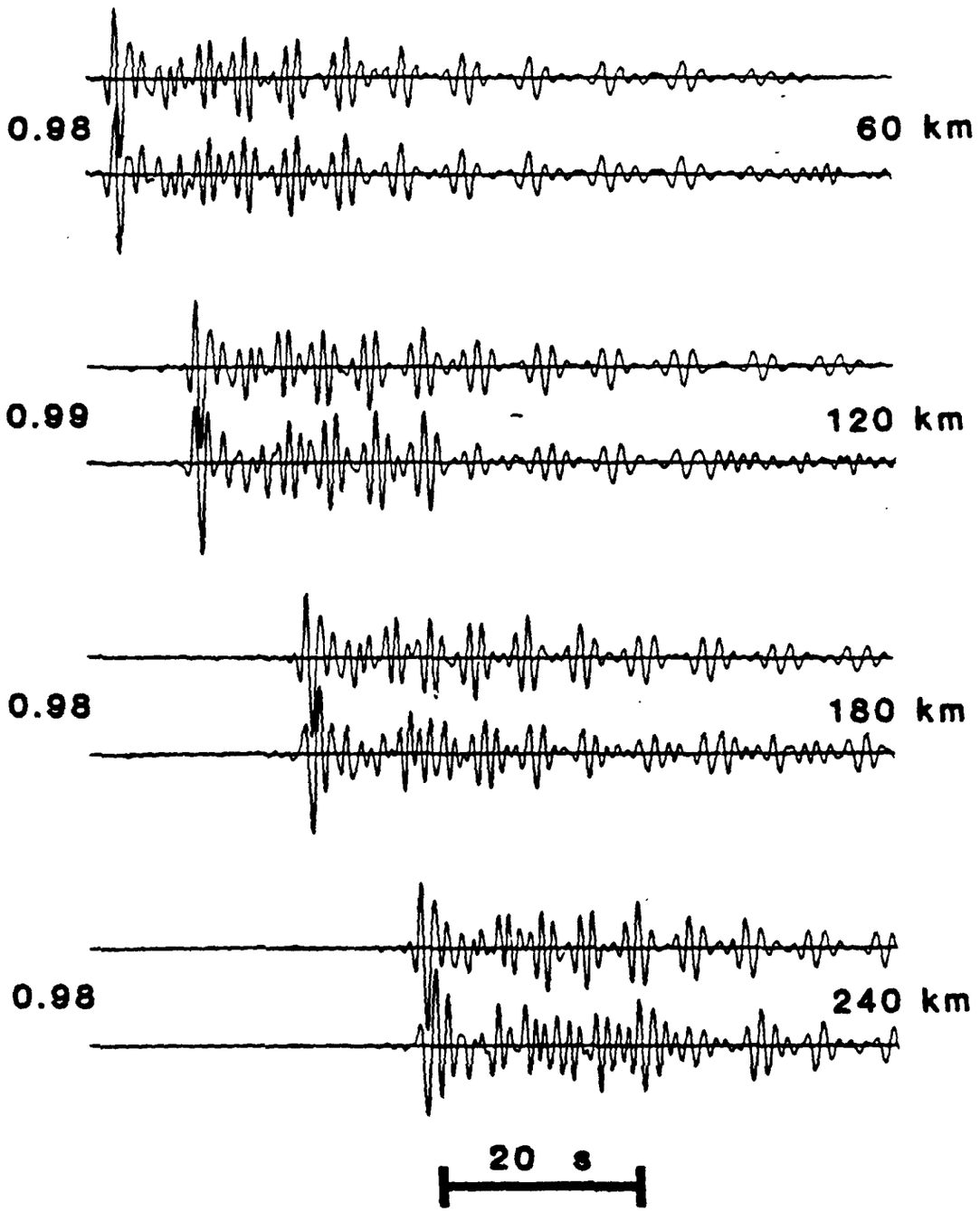

Figure 19: Comparison of hybrid solutions and 3-D mode sum synthetics. The forcing functions used are 3-D mode sum synthetics. The upper trace in each pair is the mode sum synthetic, the lower trace is the hybrid solution. Numbers at the left above each pair of seismograms indicates distance from source to receiver at the surface. Numbers at the right give the ratio of RMS amplitude of the hybrid solution to the RMS amplitude of the direct synthetic.

are shown below the right end of each pair of traces. The major differences in the synthetic and hybrid solutions are seen in the amplitude of the first large positive and negative peaks. The amplitude of these peaks is not stable since they are the result of sampling a very high frequency arrival not resolved at the time spacing used. These peaks yield the maximum peak to peak amplitude so the peak to peak amplitude is not stable. This makes the peak to peak amplitude a poor measure of the amplitude fit between models. A far more stable measure of amplitude correspondence between seismograms of this type is the RMS amplitude calculated over some time window appropriate to the seismograms being compared. The RMS amplitudes calculated with window lengths of as much as 45s agree to better than one percent for all pairs of seismograms shown in Figure 18. RMS amplitudes calculated with window lengths greater than 45 seconds show discrepancies in the amplitude correspondence between each pair due to the finite length of the seismogram. Some discrepancies are seen between the detailed waveforms of the direct and hybrid synthetics. These discrepancies are of at least two types. First, and most easily explained, are the small arrivals seen at the beginning of the seismogram in the direct synthetics only. The lack of these arrivals on the hybrid synthetics is due to the exclusion of the very low amplitude initial portion of each seismogram used as forcing function. These portions lie outside the input window as illustrated in Figure 17. Second, are the small discrepancies seen in the higher frequency component of the seismograms, particularly within the first twenty seconds of the trace. To better quantify these shorter period differences, and to enable one to view the record as one would see data from an event, the WWSSN short period instrument response is convolved with seismograms of the type shown in Figure 18 to give seismograms of the type shown in Figure 19.

Figure 19 shows comparisons between direct and hybrid synthetics for a selection of horizontal distances along the free surface. Above each pair of seismograms the

horizontal distance from the source to the receiver is shown. For this test a FE grid of dimensions 150x300 nodes was used. Beside each pair of traces the ratio of hybrid to direct RMS amplitudes is given. In each pair, the upper seismogram is the direct synthetic and the lower trace is the hybrid synthetic. The duration of all seismograms is 102s and the peak to peak amplitude of each trace is scaled to the same value. Each seismogram shown is bandpass filtered between 0.01 and 1.00 Hz and includes the WWSSN instrument. The bandpass filter is applied to the forcing functions and to the resulting FE seismograms. It is applied twice in succession to the direct synthetics. The waveform correspondence between the two types of synthetics is excellent for short horizontal distances, but worsens as horizontal distance increases. The most striking changes occur in the maximum peak to peak amplitudes, and in the amplitudes of successive peaks relative to each other in the first ten to twenty seconds of the record. It appears that the waveform correspondence between the two types of synthetics is excellent if the first ten to twenty seconds of the record is omitted. The discrepancies early in the seismogram could have several sources such as, truncation errors due to the use of too few input forcing functions, the comparison of hybrid seismograms which experience 2-D spreading in the portion of their paths in the FE grid to direct seismograms which experience 3-D propagation along the entire path, reflections from the bottom of the FE grid, and possible intrinsic errors due to the accuracy of the numerical codes or completeness of the chosen representation for the forcing functions and direct seismograms. Some of these possible sources for differences in waveform will be discussed in detail below or in later chapters. It is important to note that despite the small variations in the waveform the RMS amplitude correspondence is excellent and stable as propagation distance increases.

Next the necessary vertical extent of input forcing functions needed to produce an accurate mode sum hybrid seismogram and the truncation error associated with

that vertical extent will be discussed. For the case of the SH pulse from a line source discussed earlier it was found that accurate results required a vertical extent of forcing functions greater than the depth of the receiver by an amount that increased as the horizontal propagation distance increased. This meant that the coupling of an SH pulse from a distant source into a grid with a high aspect ratio necessarily produced results that became very poor at large distances. Fortunately, this behavior does not directly generalize to the case of a layer over a half-space. For a layer over a half-space the results are compatible with and can be explained by considering the Love waves to be modeled in terms of constructive interference of post critical multiple reflections trapped within the crustal layer. This interpretation of Love waves suggests that the most critical nodes at which forcing functions need to be applied are the initial nodes in each row of the grid located in the crustal layer. The results of the calculations illustrated in Figures 20 and 21 show large changes in the waveforms and amplitudes of hybrid synthetics occur as the number of input forcing functions increases, until all nodes in the first column of the grid that lie within the crustal layer have forcing functions applied to them. Further increases in the depth extent of applied forcing functions produce only small changes in waveform in the first thirty seconds of the trace and almost no changes in RMS amplitudes. This remains true of the hybrid synthetics after propagation distances of more than five to ten layer thicknesses of the crustal layer.

All results shown in Figures 20 and 21 were calculated in a FE grid of dimension 150x300 nodes. Five FE calculations were completed, each using a different number of applied forcing functions. These tests use fifteen, thirty, forty five, sixty, and ninety applied forcing functions. In Figures 20 and 21 a number or numbers appear below and at the right end of each seismogram. This number n indicates that n forcing functions are applied to the topmost n nodes in the first column of the FE grid in the

calculation that produced the illustrated seismogram. The pairs of numbers at the left end of each seismogram are peak to peak and fifty five second RMS amplitude ratios. For each seismogram the ratio shown is the ratio of the amplitude of the seismogram being considered to the amplitude of the seismogram at the same location for the example using sixty forcing functions. The uppermost number is the peak to peak ratio, the number below it is the RMS ratio. The layer thickness of thirty two kilometers is equivalent to sixty four rows of nodes. The sixty fifth row of nodes is the first row describing the half-space. The calculation using sixty applied forcing functions is used as a reference since the behavior of the discrepancies due to truncation of the vertical extent of input forcing functions changes when forcing functions are applied outside the layer.

Figure 20 shows three groups of seismograms. Each group is recorded at the surface at a given horizontal distance. That distance is shown on the figure above each group of traces. The first group consists of a single seismogram recorded five kilometers or ten elements from the grid edge. This seismogram represents the identical results observed in the five test cases. The second group of seismograms are recorded twenty five kilometers from the grid edge. The first seismogram in this group represents the almost identical results for the three test cases using the largest numbers of applied forcing functions. Amplitude discrepancies between these cases were less that 0.2%, and no differences in waveform could be seen when the seismograms for each case were overlaid. However, the second two seismograms in the group, representing the tests with thirty and fifteen applied forcing functions respectively show significant differences in waveform and amplitude. The most striking effect of using fewer applied forcing functions is the reduction in the amplitudes of the later arrivals in the seismograms with respect to the early arrivals. The peak to peak amplitudes and the RMS amplitudes with longer window lengths were also reduced as

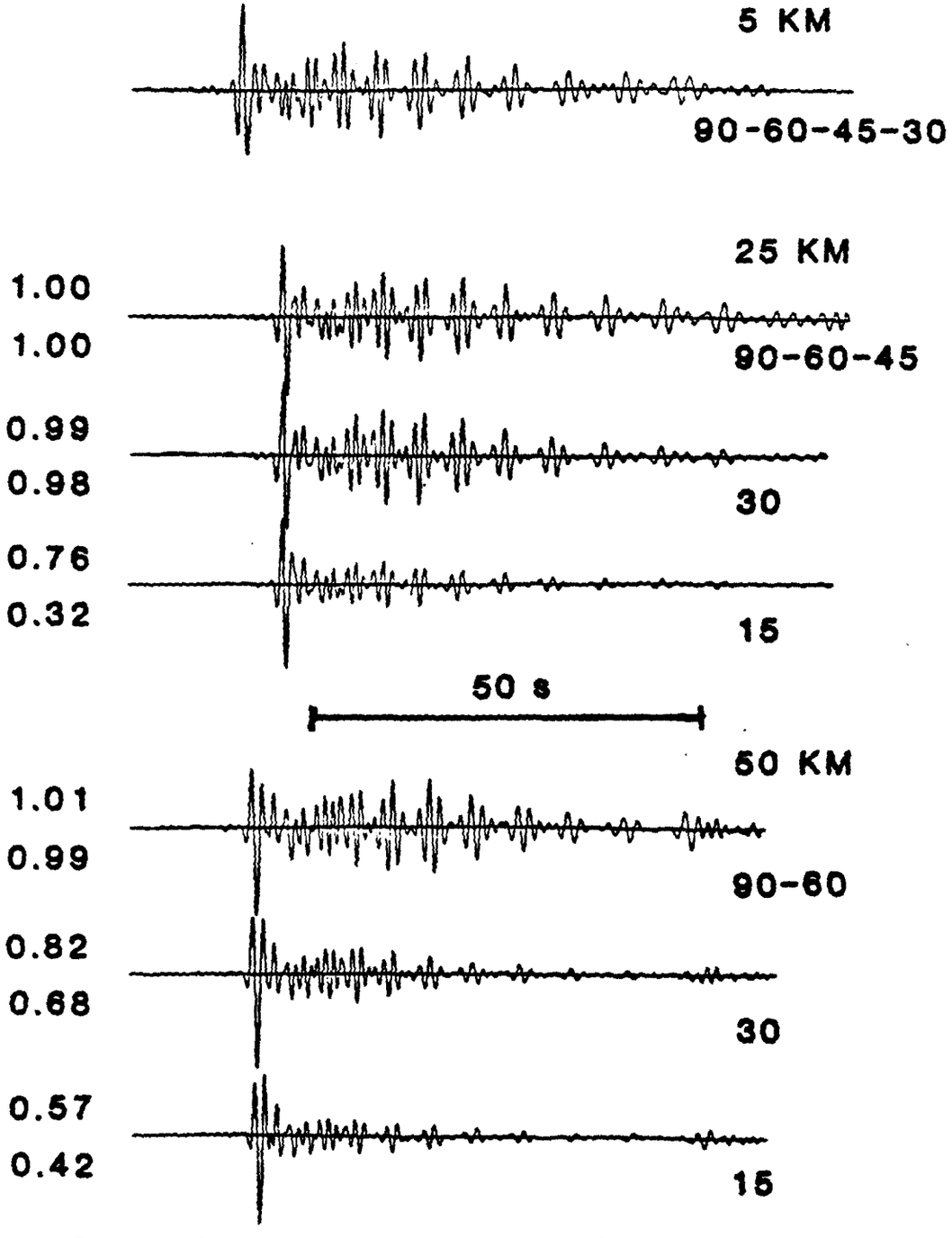

Figure 20: Comparison of hybrid results using different numbers of input forcing functions. Each group of seismograms shows results at a given horizontal distance, as labeled above that group. The number or numbers below and to the right of each seismogram indicate the number of nodes where forcing functions are applied. The pairs of numbers to the left of each seismogram are amplitude ratios. The upper number in each pair is the ratio of the peak to peak amplitudes of that trace to the trace using 60 forcing functions recorded at that distance. The lower number in each pair is the corresponding ratio for RMS amplitudes.

the number of applied forcing functions decreased. In particular, for the seismogram generated using thirty applied forcing functions the RMS amplitude measure corresponds well with the examples using more forcing functions until the window length of the RMS operator exceeds sixty seconds, then the discrepancy increases as the window length increases. For the example using fifteen forcing functions the trend seen in the RMS amplitudes follows the same pattern but the differences in peak to peak amplitude mean that agreement is not good even at a window length of fifteen seconds. If results of the calculation using fifteen forcing functions are examined at locations between the two distances illustrated it is found that the behavior seen in the thirty forcing function example is seen at distances around twelve kilometers in the fifteen forcing function calculation. The third group of seismograms is recorded at a distance of fifty kilometers. The second two seismograms in that group also show the rapid decline in RMS amplitude as the RMS window length increases. However, the example using thirty forcing functions now also shows poor agreement even in the fifteen second window. The example using forty five forcing functions is not illustrated at this distance. The RMS amplitude of the forty five forcing function seismogram corresponds well with the more complete examples for RMS windows as long as sixty five seconds. It was not considered necessary to illustrate this seismogram as it was so similar to the first seismogram in the group. From examining the seismograms at these three distances patterns are beginning to emerge, that will be clarified by the additional distances illustrated in the next figure.

Figure 21 is a continuation of Figure 20 for seismograms recorded at greater distances along the free surface. The amplitude ratios of the two examples using fifteen and thirty forcing functions continue to decrease with distance, although the RMS amplitudes have almost stablized by the time the horizontal distance has reach 150 km. The disturbances visible in the trace have become larger with respect to the

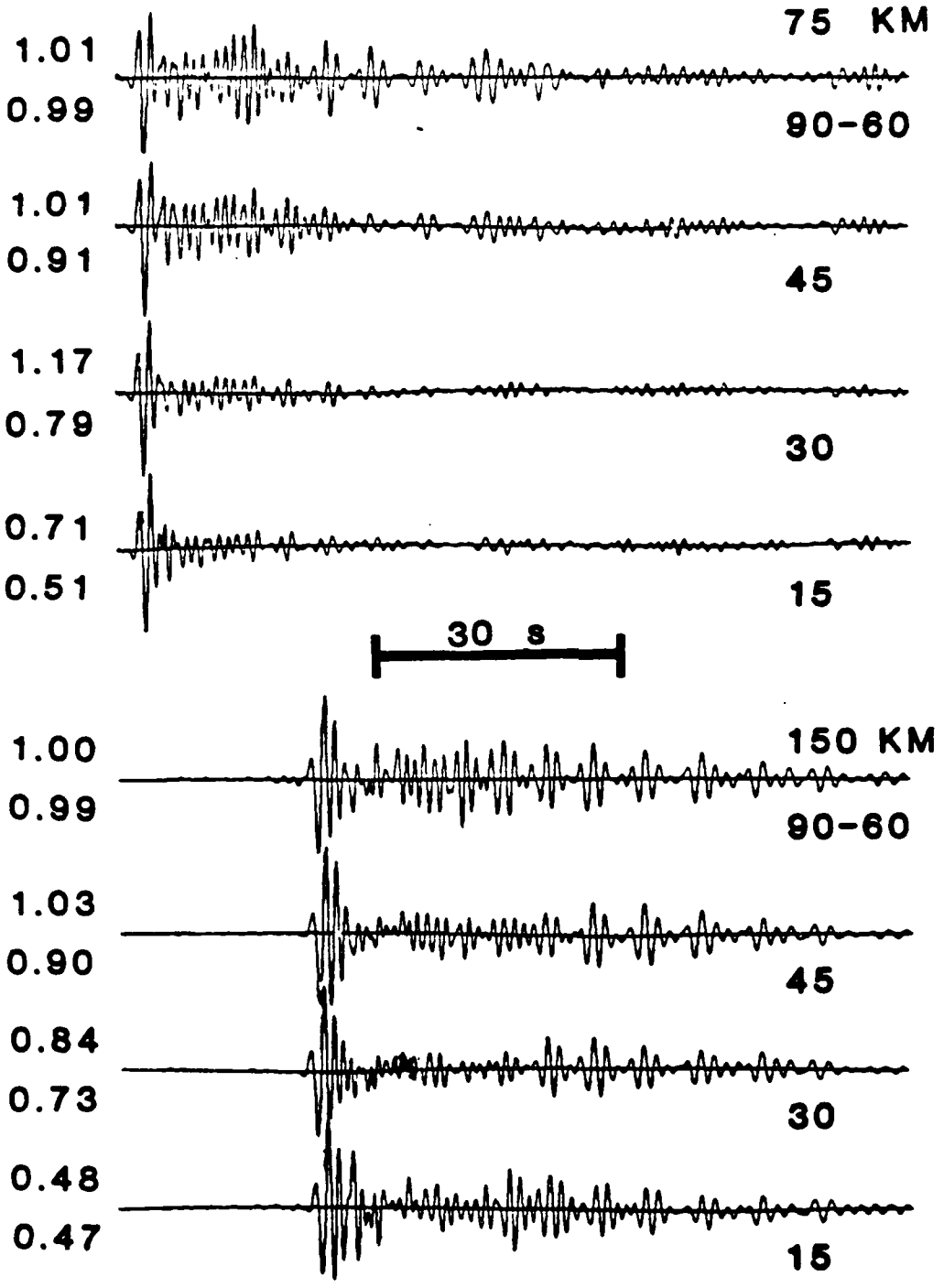

Figure 21: Comparison of hybrid results using different numbers of input forcing functions. Details are the same as figure 20.

shrinking arrival that determines the maximum peak to peak amplitude of the seismogram. For the example using forty five forcing functions the later arrivals continue to shrink with respect to the earlier arrivals as horizontal distance increases, reducing the RMS amplitude in successively shorter time windows. At distances between seventy five and one hundred kilometers the RMS amplitude stabilizes at about 90% of the values seen for the examples using more forcing functions. However, the waveforms correspondence continues to decay. Generalizing the results seen in the examples using a depth extent of forcing functions considerably less than the thickness of the crustal layer leads to several observations. Seismograms along the surface are identical regardless of the number of forcing functions used provided that the propagation distance in the FE grid is less than or equal to the depth extent of the forcing functions. Beyond that distance range the amplitude of the waveform begins to decay. The amplitudes of the latest arrivals are the first to be reduced. As the distance increases progressively earlier arrivals are reduced in amplitude while amplitudes of the later arrivals continue to decay further. As the number of forcing functions increases the rate of amplitude decay decreases and the RMS amplitude value at which the amplitude eventually stabilizes increases. When the depth extent of forcing functions exceeds the crustal layer thickness this behavior changes. At a distance of three hundred kilometers the two examples using sixty and ninety forcing functions continue to agree very well. They show some differences in waveform, barely perceptible when the waveforms are overlaid, in the relative amplitudes of successive peaks during the first twenty to thirty seconds of the seismogram. At larger distances this discrepancy increases slightly, but the amplitude ratios remain very stable and the waveform differences remain small and confined to the first thirty seconds of the seismograms. Thus, truncation error can explain at least a part of the waveform discrepancies seen in the early portions of the seismograms illustrated in the surface section shown in Figure 19.

Figures 22 and 23 illustrate the effects of using different numbers of row of nodes, that is varying the vertical extent of the FE grid, on the resulting SH L_g mode sum seismograms. In each of these figures two groups of three seismograms are shown. Each group is labeled with its propagation distance in the FE grid. The same forcing functions, for a source 1500 km distant at a depth of eight kilometers, are used for each calculation. All seismograms in these figures are plotted at the same scale. The uppermost seismogram in each group was calculated in a FE grid with ninety rows, the center seismogram in a FE grid with one hundred fifty rows and the lower seismogram in a FE grid with three hundred rows. An additional difference between the grids used in these tests is that the grid in which the uppermost seismogram in each group is calculated has a length of five hundred nodes and the other two grids have a length of three hundred nodes. Consequently, differences seen in the last ten to twelve seconds of the upper two records can be attributed to reflections from the righthand edge of the grid. All other differences seen between these seismograms can be attributed to reflections from the bottom edge of the grid. Since the travel time to the bottom of the grid is increased as the number of rows in the grid is increased, any reflections from the bottom of the grid should be seen at different points in the seismogram for each grid. The length of the seismogram is chosen so that reflections from the bottom of the three hundred row grid should arrive after the end of the seismogram. The reflections from the righthand edge of the grid are small but clearly visible, and are, as expected, identical on both of the lower two seismograms in each group. Examining the group of seismograms for a propagation distance of fifty kilometers within the FE grid shows essentially no differences between the seismograms recorded in grids with ninety and three hundred rows. When compared carefully to these seismograms the seismogram calculated in the grid with one hundred fifty rows shows some small differences in the amplitudes of some of the peaks. The RMS amplitudes agree to within less than 0.1%. This implies that reflections from the bottom of the

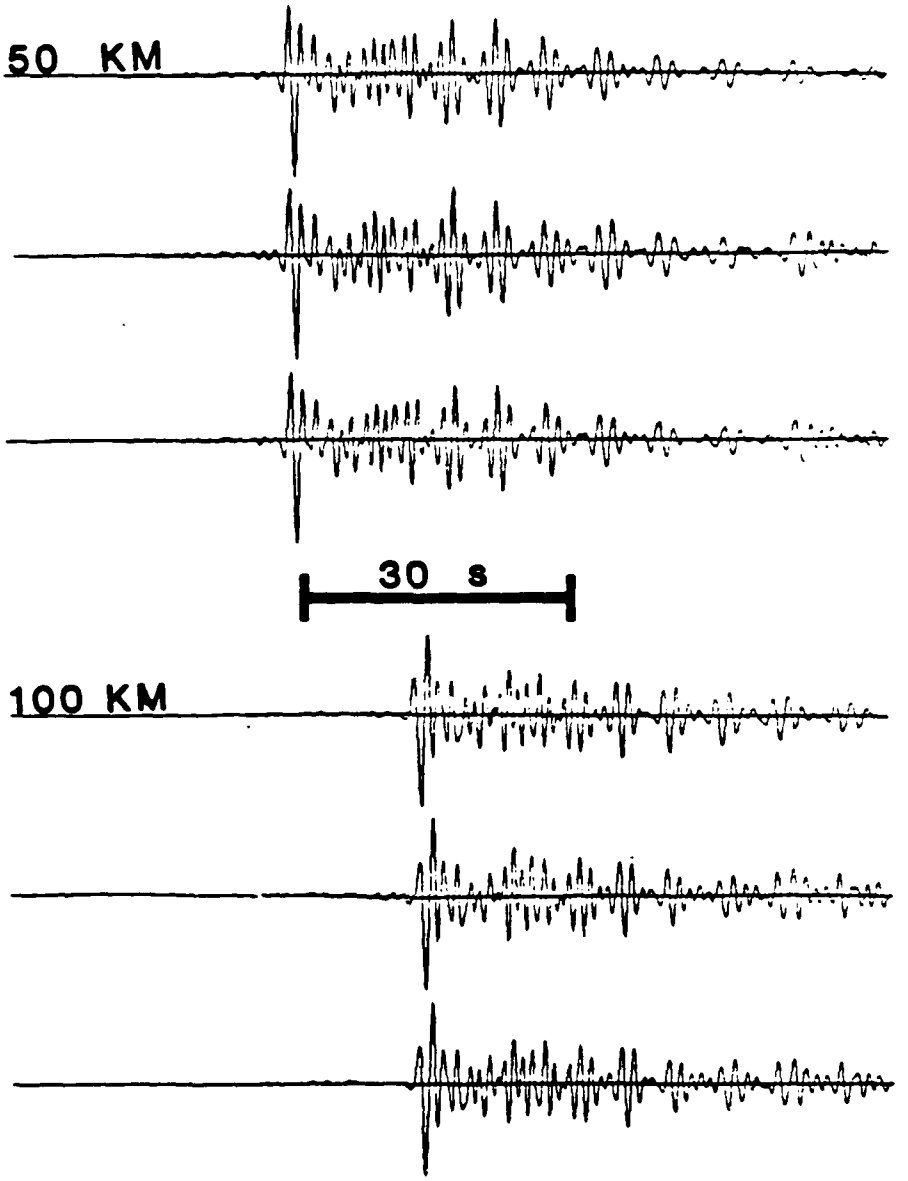

Figure 22: Comparison of hybrid solutions for cases using different numbers of rows of nodes. Results show wide angle reflections are not important. Each group of three seismograms is recorded at the free surface at the indicated distance from the grid edge. The upper trace in each group uses 90 rows of nodes, the center trace 150 rows of nodes and the bottom trace 300 rows. The peak to peak amplitudes of each trace are normalized to one. Differences in peak to peak amplitudes are so small that all peak to peak and RMS amplitude ratios are 1.00. Duration of each seismogram is 102 seconds.

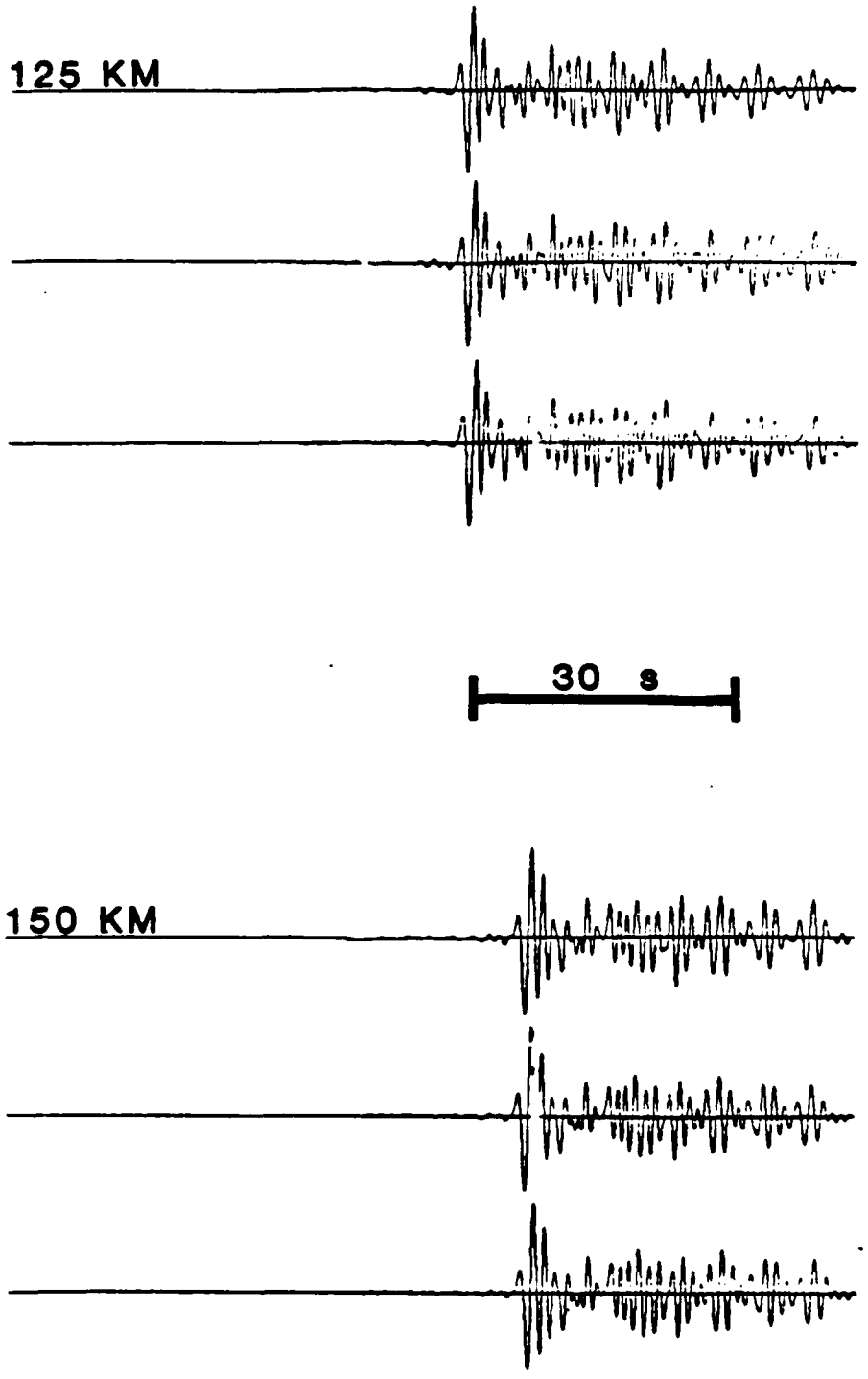

Figure 23 Comparison of hybrid solutions for cases using different numbers of rows of nodes. Details are the same as for figure 22.

grid are insignificant with short path lengths in the grid. For a path length of one hundred kilometers within the FE grid the reflections from the bottom of the grid remain insignificant, as illustrated in the second group of seismograms in figure 22. The two groups of seismograms in Figure 23 show that the reflections from the bottom of the grid remain insignificant to distances of at least one hundred fifty kilometers. Thus, even for aspect ratios as high as three the reflections from the bottom of the grid are not significant when the propagation of SH type L_g mode sum seismograms in a layer over a half-space is being considered. This conclusion will be further supported when the transparent boundary conditions are considered in the following chapter. It will be demonstrated that reflections from the bottom of the grid are significant only when structures are not plane layered.

Summary

In this chapter the basics of the modal propagator matrix method and the FE method were discussed, including the modifications made to the existing implementations of these methods. An approach to apply the Representation Theorem to combine these techniques into a hybrid method was explained. The particulars of the implementiation of the coupling technique differ depending on whether the propagator results are to be passed into the FE calculation or the the FE results are to be transmitted further using the propagator matrix technique. The coupling from modal propagator matrix results to the FE method was demonstrated for the simple example of a layer over a half-space. This simple structure allowed the calculation of analytic synthetics to which the hybrid synthetics could be directly compared to give estimates of the accuracy of the coupling technique.

DARPA SUPPLEMENTAL LIST FOR TECHNICAL REPORTS (Unclassified)
DISTRIBUTION LIST

Dr. Monem Abdel-Gawad
Rockwell International Science Center
1049 Camino Dos Rios
Thousand Oaks, CA 91360

Professor Keiiti Aki
Center for Earth Sciences
University of Southern California
University Park
Los Angeles, CA 90089-0741

Professor Shelton S. Alexander
Geosciences Department
403 Deike Building
The Pennsylvania State University
University Park, PA 16802

Professor Charles B. Archambeau
Cooperative Institute for Research in
Environmental Sciences
University of Colorado
Boulder, CO 80309

Dr. Thomas C. Bache Jr.
Science Applications Int'l Corp.
10210 Campus Point Drive
San Diego, CA 92121

Dr. James Bulau
Rockwell International Science Center
1049 Camino Dos Rios
P.O. Box 1085
Thousand Oaks, CA 91360

Dr. Douglas R. Baumgardt
Signal Analysis and Systems Division
ENSCO, Inc.
5400 Port Royal Road
Springfield, VA 22151-2388

Dr. S. Bratt
Science Applications Int'l Corp.
10210 Campus Point Drive
San Diego, CA 92121

Professor John Ebel
Department of Geology & Geophysics
Boston College
Chestnut Hill, MA 02167

Woodward-Clyde Consultants
Attn: Dr. Lawrence J. Burdick
Dr. Jeff Barker
P.O. Box 93245
Pasadena, CA 91109-3245 (2 copies)

Dr. Roy Burger
1221 Serry Rd.
Schenectady, NY 12309

Professor Robert W. Clayton
Seismological Laboratory
Division of Geological and Planetary
Sciences
California Institute of Technology
Pasadena, CA 91125

Dr. Vernon F. Cormier
Earth Resources Laboratory
Department of Earth, Atmospheric and
Planetary Sciences
Massachusetts Institute of Technology
42 Carleton Street
Cambridge, MA 02142

Professor Anton M. Dainty
Earth Resources Laboratory
Department of Earth, Atmospheric and
Planetary Sciences
Massachusetts Institute of Technology
42 Carleton Street
Cambridge, MA 02142

Dr. Zoltan A. Der
Teledyne Geotech
314 Montgomery Street
Alexandria, VA 22314

Prof. Adam Dziewonski
Hoffman Laboratory
Harvard University
20 Oxford St.
Cambridge, MA 02138

Professor John Ferguson
Center for Lithospheric Studies
The University of Texas at Dallas
P.O. Box 830688
Richardson, TX 75083-0688

Dr. Jeffrey W. Given
Sierra Geophysics
11255 Kirkland Way
Kirkland, WA 98033

Prof. Roy Greenfield
Geosciences Department
403 Deike Building
The Pennsylvania State University
University Park, PA 16802

Professor David G. Harkrider
Seismological Laboratory
Division of Geological and Planetary Sciences
California Institute of Technology
Pasadena, CA 91125

Professor Donald V. Helmberger
Seismological Laboratory
Division of Geological and Planetary Sciences
California Institute of Technology
Pasadena, CA 91125

Professor Eugene Herrin
Institute for the Study of Earth & Man
Geophysical Laboratory
Southern Methodist University
Dallas, TX 75275

Professor Robert B. Herrmann
Department of Earth and Atmospheric Sciences
Saint Louis University
Saint Louis, MO 63156

Professor Lane R. Johnson
Seismographic Station
University of California
Berkeley, CA 94720

Professor Thomas H. Jordan
Department of Earth, Atmospheric and Planetary Sciences
Massachusetts Institute of Technology
Cambridge, MA 02139

Dr. Alan Kafka
Department of Geology & Geophysics
Boston College
Chestnut Hill, MA 02167

Professor Charles A. Langston
Geosciences Department
403 Deike Building
The Pennsylvania State University
University Park, PA 16802

Professor Thorne Lay
Department of Geological Sciences
1006 C.C. Little Building
University of Michigan
Ann Arbor, MI 48109-1063

Dr. George R. Mellman
Sierra Geophysics
11255 Kirkland Way
Kirkland, WA 98033

Professor Brian J. Mitchell
Department of Earth and Atmospheric Sciences
Saint Louis University
Saint Louis, MO 63156

Professor Thomas V. McEvilly
Seismographic Station
University of California
Berkeley, CA 94720

Dr. Keith L. McLaughlin
Teledyne Geotech
314 Montgomery Street
Alexandria, VA 22314

Professor Otto W. Nuttli
Department of Earth and Atmospheric Sciences
Saint Louis University
Saint Louis, MO 63156

Professor Paul G. Richards
Lamont-Doherty Geological Observatory
of Columbia University
Palisades, NY 10964

Dr. Norton Rimer
S-Cubed
A Division of Maxwell Laboratory
P.O. 1620
La Jolla, CA 92038-1620

Professor Larry J. Ruff
Department of Geological Sciences
1006 C.C. Little Building
University of Michigan
Ann Arbor, MI 48109-1063

Professor Charles G. Sammis
Center for Earth Sciences
University of Southern California
University Park
Los Angeles, CA 90089-0741

Dr. David G. Simpson
Lamont-Doherty Geological Observatory
of Columbia University
Palisades, NY 10964

Dr. Jeffrey L. Stevens
S-CUBED,
A Division of Maxwell Laboratory
P.O. Box 1620
La Jolla, CA 92038-1620

Professor Brian Stump
Institute for the Study of Earth
and Man
Geophysical Laboratory
Southern Methodist University
Dallas, TX 75275

Professor Ta-liang Teng
Center for Earth Sciences
University of Southern California
University Park
Los Angeles, CA 90089-0741

Dr. R. B. Tittmann
Rockwell International Science Center
1049 Camino Dos Rios
P.O. Box 1085
Thousand Oaks, CA 91360

Professor M. Nafi Toksoz
Earth Resources Laboratory
Department of Earth, Atmospheric and
Planetary Sciences
Massachusetts Institute of Technology
42 Carleton Street
Cambridge, MA 02142

Professor Terry C. Wallace
Department of Geosciences
Building #11
University of Arizona
Tucson, AZ 85721

Prof. John H. Woodhouse
Hoffman Laboratory
Harvard University
20 Oxford St.
Cambridge, MA 02138

Dr. G. Blake
US Dept of Energy/DP 331
Forrestal Building
1000 Independence Ave.
Washington, D.C. 20585

Dr. Michel Bouchon
Universite Scientifique et
Medicale de Grenoble
Laboratoire de Geophysique
Interne et Tectonophysique
I.R.I.G.M.-B.P. 68
38402 St. Martin D'Heres
Cedex FRANCE

Dr. Hilmar Bungum
NTNF/NORSAR
P.O. Box 51
Norwegian Council of Science,
Industry and Research, NORSAR
N-2007 Kjeller, NORWAY

Dr. Alan Douglas
Ministry of Defense
Blacknest, Brimpton, Reading RG7-4RS
UNITED KINGDOM

Professor Peter Harjes
Institute for Geophysik
Rhur University
Bochum
P.O. Box 102148
4630 Bochum 1
FEDERAL REPUBLIC OF GERMANY

Dr. James Hannon
Lawrence Livermore National Laboratory
P.O. Box 808
Livermore, CA 94550

Dr. E. Husebye
NTNF/NORSAR
P.O. Box 51
N-2007 Kjeller, NORWAY

Dr. Arthur Lerner-Lam
Lamont-Doherty Geological Observatory
of Columbia University
Palisades, NY 10964

Mr. Peter Marshall
Procurement Executive
Ministry of Defense
Blacknest, Brimpton, Reading RG7-4RS
UNITED KINGDOM

Dr. B. Massinon
Societe Radiomana
27, Rue Claude Bernard
75005, Paris, FRANCE

Dr. Pierre Mechler
Societe Radiomana
27, Rue Claude Bernard
75005, Paris, FRANCE

Mr. Jack Murphy
S-CUBED
Reston Geophysics Office
11800 Sunrise Valley Drive
Suite 1212
Reston, VA 22091

Dr. Svein Mykkeltveit
NTNF/NORSAR
P.O. Box 51
N-2007 Kjeller, NORWAY

Dr. Carl Newton
Los Alamos National Laboratory
P.O. Box 1663
Mail Stop C 335, Group ESS3
Los Alamos, NM 87545

Dr. Peter Basham
Earth Physics Branch
Department of Energy and Mines
1 Observatory Crescent
Ottawa, Ontario
CANADA K1A 0Y3

Professor J. A. Orcutt
Geological Sciences Division
Univ. of California at San Diego
La Jolla, CA 92093

Dr. Frank F. Pilotte
Director of Geophysics
Headquarters Air Force Technical
Applications Center
Patrick AFB, Florida 32925-6001

Professor Keith Priestley
University of Nevada
Mackay School of Mines
Reno, Nevada 89557

Mr. Jack Raclin
USGS - Geology, Rm 3C136
Mail Stop 928 National Center
Reston, VA 22092

Dr. Frode Ringdal
NTNF/NORSAR
P.O. Box 51
N-2007 Kjeller, NORWAY

Dr. George H. Rothe
Chief, Research Division
Geophysics Directorate
Headquarters Air Force Technical
Applications Center
Patrick AFB, Florida 32925-6001

Dr. Alan S. Ryall, Jr.
Center for Seismic Studies
1300 North 17th Street
Suite 1450
Arlington, VA 22209-2308

Dr. Lawrence Turnbull
OSWR/NED
Central Intelligence Agency
CIA, Room 5G48
Washington, DC 20505

Professor Steven Grand
Department of Geology
245 Natural History Bldg
1301 West Green Street
Urbana, IL 61801

DARPA/PM
1400 Wilson Boulevard
Arlington, VA 22209

Defense Technical Information Center
Cameron Station
Alexandria, VA 22314 (12 copies)

Defense Intelligence Agency
Directorate for Scientific and
Technical Intelligence
Washington, D.C. 20301

Defense Nuclear Agency
Shock Physics Directorate/SS
Washington, D.C. 20305

Defense Nuclear Agency/SPSS
ATTN: Dr. Michael Shore
6801 Telegraph Road
Alexandria, VA 22310

AFOSR/NPG
ATTN: Director
Bldg 410, Room C222
Bolling AFB, Washington, D.C. 20332

AFTAC/CA (STINFO)
Patrick AFB, FL 32925-6001

AFWL/NTESC
Kirtland AFB, NM 87171

U.S. Arms Control & Disarmament Agency
ATTN: Mrs. M. Hoinkes
Div. of Multilateral Affairs, Rm 5499
Washington, D.C. 20451

U.S. Geological Survey
ATTN: Dr. T. Hanks
National Earthquake Research Center
345 Middlefield Road
Menlo Park, CA 94025

SRI International
333 Ravensworth Avenue
Menlo Park, CA 94025

Center for Seismic Studies
ATTN: Dr. C. Romney
1300 North 17th Street
Suite 1450
Arlington, VA 22209 (3 copies)

Dr. Robert Blandford
DARPA/GSD
1400 Wilson Boulevard
Arlington, VA 22209-2308

Ms. Ann Kerr
DARPA/GSD
1400 Wilson Boulevard
Arlington, VA 22209-2308

Dr. Ralph Alewine III
DARPA/GSD
1400 Wilson Boulevard
Arlington, VA 22209-2308

Mr. Edward Giller
Pacific Sierra Research Corp.
1401 Wilson Boulevard
Arlington, VA 22209

Science Horizons, Inc.
Attn: Dr. Bernard Minster
Dr. Theodore Cherry
710 Encinitas Blvd., Suite 101
Encinitas, CA 92024 (2 copies)

Dr. Jack Evernden
USGS - Earthquake Studies
345 Middlefield Road
Menlo Park, CA 94025

Dr. Lawrence Braile
Department of Geosciences
Purdue University
West Lafayette, IN 47907

Dr. G.A. Bollinger
Department of Geological Sciences
Virginia Polytechnical Institute
21044 Derring Hall
Blacksburg, VA 24061

Dr. L. Sykes
Lamont Doherty Geological Observatory
Columbia University
Palisades, NY 10964

Dr. S.W. Smith
Geophysics Program
University of Washington
Seattle, WA 98195

Dr. L. Timothy Long
School of Geophysical Sciences
Georgia Institute of Technology
Atlanta, GA 30332

Dr. N. Biswas
Geophysical Institute
University of Alaska
Fairbanks, AK 99701

Dr. Freeman Gilbert
Institute of Geophysics &
Planetary Physics
Univ. of California at San Diego
P.O. Box 109
La Jolla, CA 92037

Dr. Pradeep Talwani
Department of Geological Sciences
University of South Carolina
Columbia, SC 29208

University of Hawaii
Institute of Geophysics
Attn: Dr. Daniel Walker
Honolulu, HI 96822

Dr. Donald Forsyth
Department of Geological Sciences
Brown University
Providence, RI 02912

Dr. Jack Oliver
Department of Geology
Cornell University
Ithaca, NY 14850

Dr. Muawia Barazangi
Geological Sciences
Cornell University
Ithaca, NY 14853

Rondout Associates
Attn: Dr. George Sutton
Dr. Jerry Carter
Dr. Paul Pomeroy
P.O. Box 224
Stone Ridge, NY 12484 (3 copies)

Dr. Bob Smith
Department of Geophysics
University of Utah
1400 East 2nd South
Salt Lake City, UT 84112

Dr. Anthony Gangi
Texas A&M University
Department of Geophysics
College Station, TX 77843

Dr. Gregory B. Young
ENSCO, Inc.
5400 Port Royal Road
Springfield, CA 22151

Dr. Ben Menaheim
Weizman Institute of Science
Rehovot, ISRAEL 951729

Weidlinger Associates
Attn: Dr. Gregory Wojcik
620 Hansen Way, Suite 100
Palo Alto, CA 94304

Dr. Leon Knopoff
University of California
Institute of Geophysics & Planetary
Physics
Los Angeles, CA 90024

Dr. Kenneth H. Olsen
Los Alamos Scientific Laboratory
Post Office Box 1663
Los Alamos, NM 87545

Prof. Jon F. Claerbout
Prof. Amos Nur
Dept. of Geophysics
Stanford University
Stanford, CA 94305 (2 copies)

Dr. Robert Burridge
Schlumberger-Doll Research Ctr.
Old Quarry Road
Ridgefield, CT 06877

Dr. Eduard Berg
Institute of Geophysics
University of Hawaii
Honolulu, HI 96822

Dr. Robert Phinney
Dr. F.A. Dahlen
Dept. of Geological & Geophysical Sci.
Princeton University
Princeton, NJ 08540 (2 copies)

Dr. Kin-Yip Chun
Geophysics Division
Physics Department
University of Toronto
Ontario, CANADA M5S 1A7

New England Research, Inc.
Attn: Dr. Randolph Martin III
P.O. Box 857
Norwich, VT 05055

Sandia National Laboratory
Attn: Dr. H.B. Durham
Albuquerque, NM 87185

Dr. Gary McCartor
Mission Research Corp.
735 State Street
P. O. Drawer 719
Santa Barbara, CA 93102

Dr. W. H. K. Lee
USGS
Office of Earthquakes, Volcanoes,
& Engineering
Branch of Seismology
345 Middlefield Rd
Menlo Park, CA 94025

AFGL/XO
Hanscom AFB, MA 01731-5000

AFGL/LW
Hanscom AFB, MA 01731-5000

AFGL/SULL
Research Library
Hanscom AFB, MA 01731-5000 (2 copies)

Secretary of the Air Force (SAFRD)
Washington, DC 20330

Office of the Secretary Defense
DDR & E
Washington, DC 20330

HQ DNA
Attn: Technical Library
Washington, DC 20305

Director, Technical Information
DARPA
1400 Wilson Blvd.
Arlington, VA 22209

Los Alamos Scientific Laboratory
Attn: Report Library
Post Office Box 1663
Los Alamos, NM 87544

Dr. Thomas Weaver
Los Alamos Scientific Laboratory
Los Alamos, NM 87544

Dr. Al Florence
SRI International
333 Ravenswood Avenue
Menlo Park, CA 94025-3493

END

DATE

FILMED

8-88

DTIC